Manipulation of drops with electrowetting:

From morphological transitions to microfluidics

Riëlle de Ruiter

Manipulation of drops with electrowetting:

From morphological transitions to microfluidics

Riëlle de Ruiter

Committee members:

Prof. dr. ir. J.W.M. Hilgenkamp	University of Twente, chairman
Prof. dr. F. Mugele	University of Twente, promotor
Dr. M.H.G. Duits	University of Twente, assistant promotor
Prof. D. Quéré	ESPCI ParisTech
Prof. K.K. Varanasi	Massachusetts Institute of Technology
Prof. W.T.S. Huck	Radboud University Nijmegen
Dr. I.R. Collins	BP
Prof. dr. A. van den Berg	University of Twente
Prof. dr. R.G.H. Lammertink	University of Twente

The research described in this thesis was performed at the Physics of Complex Fluids group within the MESA+ Institute for Nanotechnology and the Department of Science and Technology of the University of Twente. This work is part of the ExploRe research program which is financially supported by BP plc.

Title:	Manipulation of drops with electrowetting: From morphological transitions to microfluidics
Author:	Riëlle de Ruiter
ISBN:	978-90-365-3639-4
DOI:	10.3990/1.9789036536394

Printed by Gildeprint Drukkerijen, Enschede.

MANIPULATION OF DROPS WITH ELECTROWETTING:

FROM MORPHOLOGICAL TRANSITIONS TO MICROFLUIDICS

PROEFSCHRIFT

ter verkrijging van
de graad doctor aan de Universiteit Twente,
op gezag van de rector magnificus,
prof. dr. H. Brinksma,
volgens besluit van het College voor Promoties
in het openbaar te verdedigen op
woensdag 26 maart 2014 om 14:15 uur

door

Riëlle de Ruiter

geboren op 5 april 1985
te Tiel

This dissertation has been approved by:

Promotor:	Prof. dr. Frieder Mugele
Assistant promotor:	Dr. Michèl Duits

Table of contents

Summary

In spite of today's growing efforts to exploit alternative sources of energy, fossil fuels are still expected to serve an important part of the energy demand of society, at least for the next decades. Recovery of the oil is a technologically challenging problem. Crude oil is typically trapped in the narrow regions between the grains of a sedimentary rock at a depth of several kilometers underground. During recovery, the injected water and the released oil need to flow through interconnected pores with sizes that vary from the submicron to submillimeter range. Oil recovery can thus be considered as an applied two-phase flow microfluidics problem. With the current technology only about 50% of the oil present in the pore space can be recovered. The other part remains in the reservoir due to heterogeneity in the wettability and structure of the rock. In this thesis we address various scientific aspects related to the mobilization and subsequent removal of small liquid volumes interacting with heterogeneous solid walls.

In Enhanced Oil Recovery, the low salinity water flooding method is thought to improve oil recovery *via* a wettability alteration of the rock. However, the composition of the injection water also influences the adsorption of amphiphilic species onto the oil-water interface. In **Chapter 3** we study this interfacial adsorption and assembly for a model system of decane containing stearic acid, in contact with an aqueous phase. Deprotonation, adsorption and molecular rearrangement precede the formation of solid metal stearate multilayers. Their formation and final composition strongly depend on the pH and cationic composition of the aqueous phase. Layer formation is facilitated by synergistic effects of simultaneously present mono- and divalent cations. We find that Ca^{2+} is preferentially incorporated in the final layers. The formation of solid layers with a surface viscoelasticity – which is more pronounced in the presence of divalent ions – might influence the release of drops in complex natural systems. Further study of these systems may be justified by more concrete evidence that these layers play an important role under reservoir conditions, *i.e.*, elevated temperatures and the presence of multiple interfacially active species.

Oil drops in the rock pore space are in contact with chemically and topographically heterogeneous surfaces. As a consequence, a drop is situated in an energy landscape with various local minimum energy configurations separated by energy barriers. Variation of the drop volume or surface wettability will change this landscape and may cause displacements and/ or morphology changes of the drop. In low salinity water flooding, desorption of organic compounds is supposed to change the wettability of the rock. In this

thesis however, we use electrowetting as a method to tune the wettability of substrates reversibly and on very short time scales, and investigate the morphological transitions in two different model systems. In **Chapter 5** we first discuss the case of a drop confined between a sphere and a plane as a generic geometry representing a pore throat. The radial position of the drop with respect to the symmetry axis is studied for its dependence on the contact angle, drop volume, and sphere/ plane separation distance. Analysis of numerically calculated energy curves shows a continuous and reversible radially in- and outward movement upon variations in the contact angle. However, due to the small driving forces, for non-ideal surfaces with chemical or topographic heterogeneity, pinning forces can drastically affect the drop behavior. A substantial history-dependence in the shape and position of the drop can then occur, and the outward movement can even become discontinuous.

In contrast, transitions of a drop in contact with a cylindrical substrate, *i.e.*, a fiber, are always discontinuous. Depending on drop volume and wettability, the drop can either attain a barrel morphology engulfing the fiber, or a clamshell morphology sitting on the side of the fiber. In **Chapter 6** we specifically investigate the effect of an external driving force, in this case buoyancy, on the instability lines. The introduction of gravitational forces shrinks the bistable and barrel regimes in favor of the clamshell regime. More importantly, at large drop volumes a new stability limit related to (partial) detachment of the drop from the fiber is found for the clamshell morphology. The typical drop size for detachment increases with the capillary length of the system.

In oil recovery, the gravity forces on a drop are generally too small to be of importance. However, (abrupt) changes in drop shape and position may also affect the drag force exerted by the surrounding fluid. In **Chapter 7** we consider the balance between retaining and driving forces on drops confined between the top and bottom walls of a microfluidic channel. Electrodes are incorporated in the microchannel wall to create a local (electro)wetting defect with tunable strength. A simple model comparing the maximum trapping force and the drag force provides excellent predictions about whether a drop is released from a pinning site.

In addition, the tunable electrical traps can be used as a new tool in continuous-flow microfluidics. Combining the individual drop control achieved using electrical actuation with the high throughput of channel-based microfluidics enables several drop manipulations that are important for many lab-on-a-chip applications, such as on-demand drop trapping and release, guiding, and high-speed sorting.

Samenvatting

Ondanks toenemende inspanningen om alternatieve energiebronnen te benutten, is het de verwachting dat fossiele brandstoffen in ieder geval in de aankomende decennia nog een belangrijk aandeel zullen leveren aan de globale energievoorziening. Oliewinning is technologisch gezien nog altijd een uitdaging. Ruwe olie zit opgesloten in de nauwe poriën van korrelig sedimentair gesteente op een diepte van enkele kilometers onder de grond. Tijdens oliewinning stromen injectiewater en de losgemaakte olie door een netwerk van poriën met groottes die variëren van het submicrometer tot submillimeter gebied. Oliewinning kan dus beschouwd worden als een toegepast twee-fase stromingsprobleem op microfluïdische schaal. Met de huidige winningstechnieken kan maar ongeveer 50% van de totale hoeveelheid olie die aanwezig is in de porieruimte gewonnen worden. Het andere deel blijft achter in het reservoir ten gevolge van heterogeniteit in de bevochtigingseigenschappen en structuur van het gesteente. In dit proefschrift behandelen we een aantal wetenschappelijke aspecten die gerelateerd zijn aan de mobilisatie en verwijdering van kleine vloeistofvolumes die een interactie hebben met een heterogene vaste wand.

Tijdens 'Enhanced Oil Recovery' wordt het injecteren van (zee)water met een verlaagd zoutgehalte verondersteld de oliewinning te verhogen door veranderingen in de bevochtigingseigenschappen van het gesteente. De samenstelling van het injectiewater beïnvloedt echter ook de adsorptie van amfifiele moleculen aan het olie-water grensvlak. In **Hoofdstuk 3** bestuderen we deze adsorptie en de daaropvolgende reorganisatie van moleculen voor een modelsysteem bestaande uit een oplossing van stearinezuur in decaan, in contact met een waterfase. Deprotonatie, adsorptie, en moleculaire herschikkingen gaan vooraf aan de vorming van vaste multilagen van metaalstearaten. De vorming en de uiteindelijke samenstelling hiervan zijn sterk afhankelijk van de zuurgraad en de samenstelling van de kationen in de waterfase. Laagvorming wordt versterk door synergetische effecten van gelijktijdig aanwezige mono- en divalente kationen. We zien dat bij voorkeur Ca^{2+} in de uiteindelijke laag wordt opgenomen. De vorming van vaste lagen met een oppervlakte-visco-elasticiteit – die in aanwezigheid van divalente ionen meer uitgesproken is – kan het loslaten van druppels in complexe natuurlijke systemen beïnvloeden. Een vervolgstudie is gerechtvaardigd indien er meer concreet bewijs is dat deze lagen een belangrijke rol spelen onder de omstandigheden zoals die in oliereservoirs heersen, met name een hogere temperatuur en de aanwezigheid van een verscheidenheid aan oppervlakte-actieve stoffen.

Oliedruppels in de porieruimte van gesteente bevinden zich in contact met chemisch heterogene en onregelmatig gevormde oppervlakken. Al gevolg hiervan bevindt een druppel zich in een energielandschap met verschillende lokale minimum-energie configuraties die gescheiden zijn door activeringsenergieën. Een variatie in het druppelvolume of de bevochtigingseigenschappen van het gesteente zal dit landschap doen veranderen en mogelijk een verplaatsing en/ of verandering in morfologie van de druppel veroorzaken. Tijdens het injecteren van water met een verlaagd zoutgehalte worden veranderingen in de bevochtigingseigenschappen vermoedelijk veroorzaakt door desorptie van organische componenten. In dit proefschrift gebruiken we echter 'electrowetting' om de bevochtigingseigenschappen van substraten omkeerbaar en op zeer korte tijdschalen aan te passen, en onderzoeken we morfologische overgangen in twee verschillende modelsystemen. In **Hoofdstuk 5** behandelen we eerst het geval van een druppel in de ruimte tussen een bol en een vlakke plaat; dit is een simpel model voor een porieruimte tussen twee korrels. We onderzoeken op welke manier de radiale positie van de druppel ten opzichte van de symmetrieas afhangt van de contacthoek, het druppelvolume, en de afstand tussen de bol en de plaat. Een analyse van de numeriek bepaalde energiecurven toont een continue en omkeerbare radiale beweging naar binnen en buiten wanneer veranderingen worden aangebracht in de contacthoek. Doordat de bijbehorende drijvende krachten klein zijn kunnen plakkrachten het druppelgedrag op niet-ideale oppervlakken met chemische heterogeniteit of ruwheid echter drastisch veranderen. Het is dan mogelijk dat de vorm en positie van de druppel sterk afhankelijk worden van de voorgeschiedenis, en de beweging naar buiten kan zelfs een discontinuïteit vertonen.

Transities van een druppel in contact met een cylindrisch substraat, een vezel, zijn echter altijd discontinu. De druppel vormt afhankelijk van het druppelvolume en de bevochtigingseigenschappen ofwel een zogenaamde 'barrel' die de gehele vezel omringt, ofwel een 'clamshell' die aan één kant van de vezel zit. In **Hoofdstuk 6** onderzoeken we specifiek het effect van een externe drijvende kracht, in dit geval de Archimedeskracht op de instabiliteitslijnen. De introductie van gravitatiekrachten verkleint de bistabiliteits- en barrelregimes in het voordeel van het clamshellregime. Van groter belang is de nieuwe stabiliteitslimiet die wordt gevonden voor de clamshell: voor grote druppelvolumes laat (een gedeelte van) de druppel los van de vezel. De kenmerkende druppelgrootte voor loslating neemt toe met de capillaire lengte van het systeem.

In oliewinning zijn de gravitatiekrachten op druppels over het algemeen te klein om van belang te zijn. Veranderingen in de druppelvorm en -positie kunnen echter ook effect

hebben op de weerstandskracht die wordt uitgeoefend door de omringende vloeistof. In **Hoofdstuk 7** beschouwen we de balans tussen de weerhoudende en drijvende krachten op druppels die tussen de boven- en onderwand van een microfluïdisch kanaal ingeklemd zitten. Electroden worden in de wand van het kanaal ingebed om een lokaal (electro)wetting defect met instelbare sterkte te maken. Een eenvoudig model dat de maximale 'plakkracht' en de weerstandskracht vergelijkt, levert voortreffelijke voorspellingen of een druppel wordt losgemaakt van het defect op.

De instelbare elektrostatische energieputten kunnen daarnaast gebruikt worden voor controle over individuele druppels in microfluïdische systemen met een continue stroming. Het combineren van manipulatie van *individuele* druppels op (elektrisch gestuurd) commando, met de grote verwerkingscapaciteit van microfluïdische systemen met een continue stroming maakt verschillende druppelmanoeuvres mogelijk die belangrijk zijn voor vele lab-on-a-chip toepassingen, zoals het gecontroleerd vasthouden en loslaten van druppels, loodsen, en sorteren op hoge snelheid.

Chapter 1

Introduction

The main motivation for this thesis originates from scientific challenges in Enhanced Oil Recovery (EOR). Developing new technologies for increasing the recovery from known reservoirs is becoming more important due to the sustained high demand for oil, combined with the difficulties in finding new reserves through exploration. An example of a novel EOR technique is low salinity water flooding, where wettability alteration is thought to be responsible for the mobilization of oil interacting with clay-covered rock surfaces. While the success of this approach has been demonstrated in many cases, questions remain about the precise mechanism and the scope of the method. Scientific studies are for example necessary to unravel the exact physical-chemical mechanisms of wettability alteration, to investigate the universality with respect to rock and clay types, and to determine the local and/ or global wettability changes associated with a certain increase in recovery. In this thesis we address various aspects related to the mobilization and subsequent release of small liquid volumes interacting with solid walls. This chapter starts with a concise overview of (enhanced) oil recovery, in particular low salinity water flooding, and is concluded by an outline describing the aim of every chapter.

1.1 Motivation: Enhanced Oil Recovery

1.1.1 Structure and properties of oil reservoirs

Oil and gas originate from geological deposits containing large amounts of organic material, the so-called source rocks (Figure 1). The material has been converted to oil in a time span of thousands of years by bacterial action and extreme pressures and temperatures. Afterwards, the oil migrated via the pore space between rock or sand grains and ended up in the reservoir rock. This reservoir is a layer of porous and permeable rock (*e.g.* sandstone or limestone) that contains oil as a single hydraulically connected system. Pore sizes can vary from the submicron to submillimeter scale, and the porosity of the rock, which is the fraction that is not occupied by mineral grains, is approximately 20%. The larger fraction of the pore space is filled with oil, while a minor fraction (one fifth) consists of connate water, which was trapped during rock deposition. Reservoirs are typically a few km long and about 100 m thick, and are located at a depth of a few km. At these depths, elevated pressures (10-100 MPa) and temperatures (40-200 °C) are encountered. The oil is trapped in the reservoir by a seal of impermeable rock. There may be a gas cap above and a water-bearing permeable rock, an aquifer, below the oil.

1.1.2 Recovering oil reserves

Oil reserves are defined as “those quantities of petroleum anticipated to be commercially recoverable by application of development projects to known accumulations from a given date forward under defined conditions” (Petroleum Resources Management System). An important criterion is thus that the oil should be recoverable with existing techniques. The current total reserves are estimated at 200 billion cubic meters, which should be sufficient for 50 years of oil production at the current production rates. Increasing this time span results in more time to fully switch to other energy sources. Besides reducing oil consumption, the location of new oil fields through exploration is an option, however, the opportunities for discovering new oil fields are diminishing. An alternative option is increasing the recovery factor of existing oil fields.

Oil is recovered in various stages. During primary recovery, 5-15% of the oil initially present in the reservoir rock is produced by making use of natural mechanisms. Oil flows to the drilled production wells due to the high pressure in the reservoir, and is replaced by expanding gas or inflowing water. The flow of oil and water through the rock pore space can thus be considered as an applied two-phase flow microfluidics problem, which can be

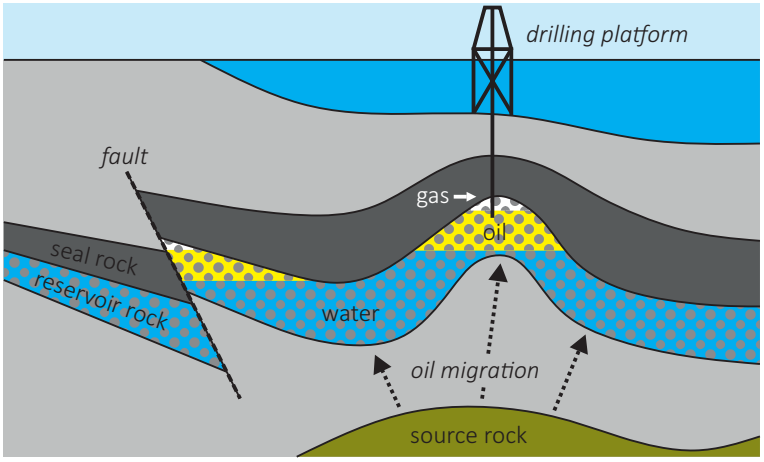

Figure 1 Schematic of an oil reservoir (not to scale).

conveniently modeled by two-phase flows in three-dimensional bead packs or quasi two-dimensional microfluidic devices. During the recovery process the reservoir pressure decreases until it becomes too low for spontaneous oil production. The recovery factor is increased to about 40% by secondary recovery, which involves the pumping of water (or gas) in injection wells to maintain an elevated pressure in the reservoir. However, a large fraction of the oil still remains in the reservoir due to rock heterogeneity, both in wettability and structure. As the less viscous water finds a preferential flow path from the injection well to the production well, significant volumes of oil can be completely bypassed. In addition, oil remains trapped in the pore-space by capillary forces. Oil production *via* secondary recovery becomes uneconomical when large amounts of water are produced. Tertiary recovery or Enhanced Oil Recovery (EOR) is a generic term for techniques that are used to further increase the amount of recovered oil. Some examples include reduction of the oil-water interfacial tension (for example *via* the addition of surfactant to the water [1], the use of microbes to produce biosurfactant *in situ* [2], or gas injection [3]), alteration of the wettability of minerals by injection of low salinity water [4], ultrasonic or seismic stimulation [5, 6], addition of polymers to block preferential flow paths and increase the sweep area [7, 8], pulsed or cyclic water injection [9], and hydraulic fracturing [10]. If new EOR techniques can be used to increase the current recovery factor with 10-20%, this would result in an additional 5-10 years of oil production and an increased production rate.

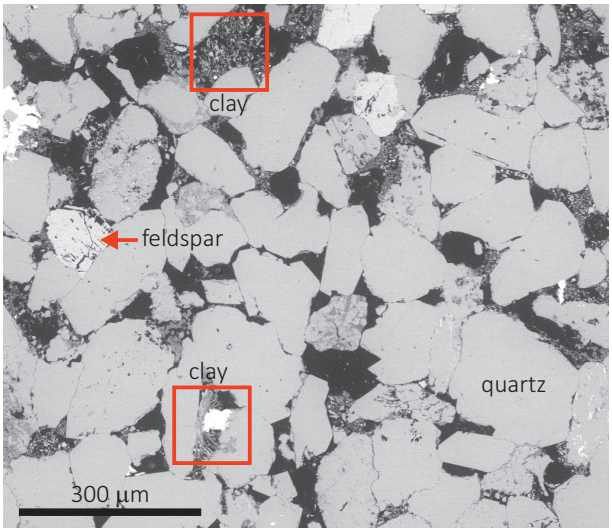

Figure 2 Cross-section of a sandstone sample observed with SEM, showing quartz and feldspar grains and two forms of clay in the pore space. Picture from K. Dalby [11].

1.1.3 Reservoir complexity

As an example of the above-mentioned reservoir rock heterogeneity, we will discuss the complexity of a sandstone sample (Figure 2). Sandstone is composed of submillimeter, rounded quartz and feldspar grains with irregular surfaces. The pore space in between the sand grains contains smaller particles of quartz and feldspar, and often clay minerals such as kaolinite, illite, montmorrillonite, muscovite, and chlorite. The clay is also present as a very thin layer on the surface of the sand grains. Oil and water thus mainly interact with clay minerals, which constitute the major part of the surface area of the pores.

Besides the inhomogeneity of the reservoir rock, also the pore fluids contribute to a large extent to the complexity of the entire system. Petroleum consists of linear alkanes, naphthenes (cycloalkanes), aromatic hydrocarbons, and the more complex asphaltenes. Besides hydrocarbons, various other organic compounds containing nitrogen, oxygen and sulfur are found. Polar compounds are mainly present amongst the larger molecules and may adsorb to the clay minerals, thereby influencing the effective wettability of the pore space. Both connate water and injection water (often seawater) contain various salts, where NaCl, $MgCl_2$, $CaCl_2$, and KCl are the most abundant. Important properties of the aqueous phase are the overall salinity, the valency of the cations and the presence of ions with specific effects.

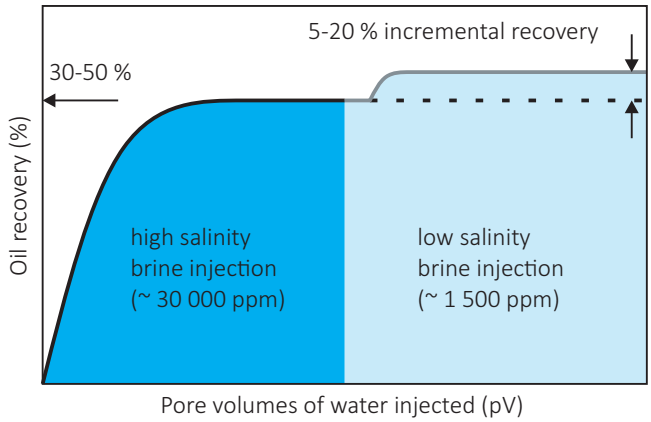

Figure 3 Schematic showing the effect of low salinity water flooding. Switching from a high salinity to a low salinity brine yields a 5-20% increment in oil recovery.

1.1.4 Low salinity water flooding

It can take over 10 years for a new Enhanced Oil Recovery technique to develop from the research stage to deployment in the field. The effect on residual oil saturation is successively determined in core floods (laboratory test on a formation sample), single well chemical tracer tests (field test near a single wellbore), and interwell trials (field test in between two wellbores). Early work on the effect of brine composition during core floods in sandstone cores was performed by Morrow *et al*. [12-15] in the 1990s. The injection of low salinity brine in cores containing clays and crude oil was shown to increases the recovery with up to 15-40% as compared to high salinity brine. Recently, field trials were performed, initially on clay-bearing sandstone formations in near wellbore regions [4, 16, 17]. Single well tests performed on the Prudhoe Bay and Endicott fields on the North slope of Alaska showed an increase in oil recovery of 8-19% when injecting a low salinity (1500 ppm) instead of a high salinity (30000 ppm) brine [4]. Subsequently, interwell tests were executed to unambiguously measure the effect of low salinity water flooding on the field scale, resulting in an incremental recovery of about 10% in the pilot tests (Figure 3) [18].

Various mechanisms have been proposed to explain the effect of low salinity flooding, for example the mobilization of clay fines [15]. Upon contact with low salinity brine, clay particles would detach from the pore surfaces and migrate to the oil-water interface, thus mobilizing previously retained oil drops. However, migration of fines and the resulting permeability reduction due to blocking of pore constrictions was not observed in

numerous core floods showing the low salinity effect [19]. Another possible explanation is a rise in pH due to carbonate dissolution and cation exchange. The pH increase would reduce the oil-water interfacial tension, increase the water wettability of the rock, and lead to *in-situ* generation of surfactants by saponification of acid compounds [4]. However, during many low salinity flooding tests low acid numbers and little pH variation were observed [19].

A more recently proposed mechanism for low salinity flooding is multi-component ion exchange between charged clay particles and the injected brine [19, 20]. In the generally accepted picture the pore space of the reservoir rock was originally filled with water and the pore walls were mostly hydrophilic (*i.e.* water wet). Upon oil migration from a source rock the smallest pores remained water-filled, however, in the largest part of the pore space the water was displaced by oil. The pore walls became more hydrophobic (*i.e.* oil wet) due to adsorption of oil compounds to the rock surface over time. As mentioned before, the pore walls mainly consist of charged clay minerals and silicon. Organic matter and clay minerals can interact *via* different mechanisms, of which some can be strongly affected by cation exchange (Figure 4). Multivalent cations, such as Mg^{2+} and Ca^{2+}, can act as bridges between the negatively charged clay surface and negatively charged compounds in the oil phase, either *via* direct bond formation (ligand bonding) or weak adsorption (cation bridging or water bridging, in the case of solvated cations). Another option is direct adsorption of organic polar compounds onto clay minerals by displacing mobile cations (cation exchange). During low salinity flooding, cations are thought to transfer between the clay minerals and the brine, thereby facilitating removal of organic compounds and organometallic complexes from the rock surface. Expansion of the electric double layer due to the low salt concentration enhances the desorption of polar compounds. The change in wettability to a less oil wet surface would then yield an increased recovery [19, 20].

A pore-scale model of the low salinity water flooding has been proposed to show the consequences of these wettability changes. The calculations predict the magnitude of the effect semi-quantitatively: a modest reduction in the oil contact angle of about 10° in the oil wet pores can easily lead to a significant incremental oil recovery of up to 60% [20]. Experimental verification of the exact physical-chemical mechanisms of wettability alteration is yet to be obtained. As a first step, the stability of Langmuir-Blodgett layers of stearic acid on silica surfaces is shown to be strongly enhanced by the presence of Ca^{2+} ions [21].

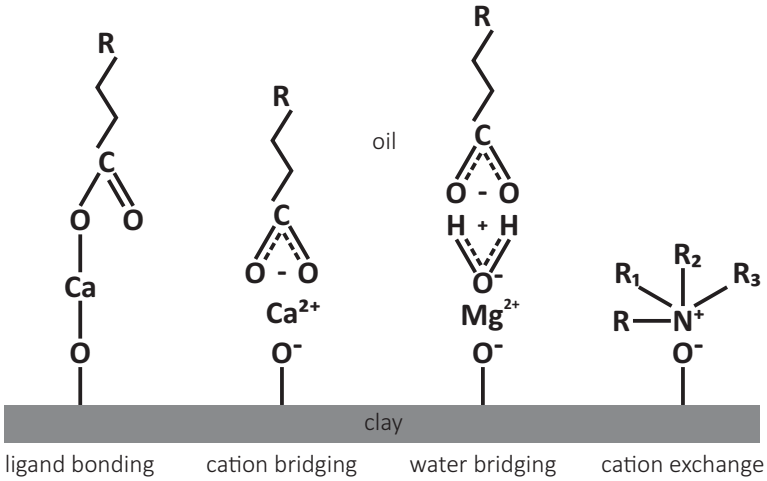

Figure 4 Interaction mechanisms between organic matter and clay minerals that can be affected by cation exchange. Figure adapted from Seccombe *et al.* [17].

1.2 Thesis outline

In this thesis we investigate various aspects related to the mobilization and subsequent removal of liquids interacting with solid walls, on the level of single drops. Oil drops in the rock pore space are in contact with chemically heterogeneous and rough surfaces, resulting in a range of possible local minimum energy configurations separated by energy barriers. Drops can change their shape in a characteristic and typically abrupt manner upon variations in the drop volume or surface wettability to adopt a morphology with lower energy. We review the topic of these so-called morphological transitions in the theoretical background in **Chapter 2**. Although the wettability variations in low salinity water flooding are supposedly caused by the desorption of organic compounds, we rely on electrically induced variations in the contact angle. **Chapter 2** concludes with a discussion on electrowetting as a method to tune the wettability of substrates continuously and reversibly on very short time scales.

Our experimental investigation starts in **Chapter 3** with the effect of adsorption processes. The primary effect triggering enhanced oil recovery in low salinity water flooding is believed to be the alteration of the contact angle, as a consequence of underlying molecular processes such as adsorption, desorption, and assembly of surface active molecules (such as asphaltenes and naphthenates). Besides adsorption onto the rock and clay surfaces, also the adsorption onto the oil-water interface influences the contact

angle. Also, the formation of solid layers with a surface viscoelasticity on these interfaces might influence the release of drops in complex natural systems. We study a simplified model system consisting of a linear alkane as the oil phase, containing the interfacially active compound stearic acid, in contact with an aqueous phase. We identify the effect of the composition of the aqueous (water flooding) phase, *i.e.* the pH, and the type and concentration of the ions, on the formation and composition of three-dimensional structures of metal stearates on the oil-water interface.

Chapter 4 discusses the development of a method to monitor the adsorption of surface active species to an oil-water interface. A drop of aqueous solution containing a simple surfactant is subjected to electrowetting in an open chip geometry. Analyzing the variation of the contact angle during consecutive amplitude modulations of the voltage yields the interfacial tension as function of drop age. We discuss the time resolution of our technique and the advantages compared to conventional techniques in terms of measured output and sample requirements.

In **Chapter 5** and **Chapter 6** we focus our attention to morphological transitions induced by wettability variations. The resulting variations in drop-substrate adhesion and exposure of the drop to external forces facilitate subsequent removal. We study morphological transition in two simplified systems, and use chemically uniform substrates without adsorbed compounds; changes in the effective wettability are obtained *via* electrowetting. In **Chapter 5**, a drop confined in between a sphere and a plate is studied. The morphology and radial position of a drop at equilibrium are dependent on the contact angle, drop volume, and sphere-plate separation. Analysis of the energy landscape shows the occurrence of a symmetry breaking that takes place in the absence of energy barriers and should thus be continuous. To explain the yet observed hysteresis in the shape and position of the drop during the experiments, we numerically study the effect of pinning. We show that small pinning forces can drastically affect the drop behavior, and delay or even preclude the outward movement.

A discontinuous transition (without pinning) is observed for a drop on a fiber: the different morphology classes are the so-called ‘barrel’ engulfing the fiber and the ‘clamshell’ sitting on the side of the fiber. The latter can be more easily detached (and subsequently removed) by external forces. In absence of gravity, the equilibrium shape is determined only by the contact angle and the drop volume, and a large regime can be found in which both shapes are metastable. In **Chapter 6** we specifically investigate the effect of buoyancy on the instability lines, introducing an additional length scale (*i.e.* the capillary

length) into the problem. We also show the existence of an additional stability limit for the clamshell, introducing (partial) detachment of liquid from the fiber. This ‘release’ cannot be observed without external driving force (like buoyancy or flow).

In **Chapter 7** we subsequently consider the balance between retaining and driving forces during drop trapping and release. Drops that are trapped in the rock pore space are modeled by drops confined between the top and bottom walls of a simple microfluidic channel. We again make use of electrowetting, now to create a local ‘wetting defect’ with tunable strength. Drops that are trapped by the defect, can be released again by increasing the hydrodynamic driving force. In such a confined environment, the pressure difference over the drop has a larger contribution than the viscous shear stresses in the surrounding fluid. We set up a simple model that predicts whether drops are released from the pinning site. In addition, our approach of incorporating electrodes in microchannel walls offers interesting opportunities in continuous-flow microfluidics, combining a high throughput with individual drop control.

Finally, we present our overall conclusions and outlook in **Chapter 8**. We discuss the implications for the forces required for drop removal in (enhanced) oil recovery.

References

[1] W. Xu, S.C. Ayrala and D.N. Rao, *Measurement of surfactant-induced interfacial interactions at reservoir conditions*, SPE Reserv. Eval. Eng. 11 (2008), 83-94.

[2] S. Maudgalya, R.M. Knapp and M.J. Mcinerney, *Microbially enhanced oil recovery technologies: a review of the past, present and future*, SPE Production and Operations Symposium, Oklahoma City (2007), SPE 106978.

[3] F.I. Stalkup, *Status of miscible displacement*, J. Pet. Technol. 35 (1983), 815-826.

[4] P.L. Mcguire, J.R. Chatham, F.K. Paskvan, D.M. Sommer and F.H. Carini, *Low salinity oil recovery: An exciting new EOR opportunity for Alaska's North Slope*, SPE Western Regional Meeting, Irvine (2005), SPE 93902.

[5] M. Hilpert, *Capillarity-induced resonance of blobs in porous media: Analytical solutions, Lattice-Boltzmann modeling, and blob mobilization*, J. Colloid Interface Sci. 309 (2007), 493-504.

[6] C. Huh, *Improved oil recovery by seismic vibration: A preliminary assessment of possible mechanisms*, First International Oil Conference and Exhibition in Mexico, Cancun (2006), SPE 103870.

[7] C. Norman, B. Turner, J.L. Romero, G. Centeno and E. Muruaga, *A review of over 100 polymer gel injection well conformance treatments in Argentina and Venezuela: Design, field implementation and evaluation*, First International Oil Conference and Exhibition in Mexico, Cancun (2006), SPE 101781.

[8] H. Frampton, J.C. Morgan, S.K. Cheung, L. Munson, K.T. Chang and D. Williams, *Development of a novel waterflood conformance control system*, SPE/DOE Fourteenth Symposium on Improved Oil Recovery, Tulsa (2004), SPE 89391.

[9] D.A. Ivanov and M. Araujo, *Dynamics of two-phase immiscible pulsed flow*, SPE/DOE Symposium on Improved Oil, Tulsa (2006), SPE 99678.

[10] B.W. Mcdaniel, *Review of current fracture stimulation techniques for best economics in multilayer, lower-permeability reservoirs*, SPE Eastern Regional Meeting, Morgantown (2005), SPE 98025.

[11] K. Dalby, *personal communication* (2014).

[12] P.P. Jadhunandan and N.R. Morrow, *Spontaneous imbibition of water by crude-oil/brine/rock systems*, In Situ 15 (1991), 319-345.

[13] P.P. Jadhunandan and N.R. Morrow, *Effect of wettability on waterflood recovery for crude-oil/brine/rock systems*, SPE Reserv. Eng. 10 (1995), 40-46.

[14] H.O. Yildiz and N.R. Morrow, *Effect of brine composition on recovery of Moutray crude oil by waterflooding*, J. Pet. Sci. Eng. 14 (1996), 159-168.

[15] G.Q. Tang and N.R. Morrow, *Influence of brine composition and fines migration on crude oil/brine/rock interactions and oil recovery*, J. Pet. Sci. Eng. 24 (1999), 99-111.

[16] K.J. Webb, C.J.J. Black and H. Al-Ajeel, *Low salinity oil recovery - log-inject-log*, SPE/DOE Improved Oil Recovery Symposium, Tulsa (2004).

[17] J.C. Seccombe, A. Lager, K.J. Webb, G.R. Jerauld and E. Fueg, *Improving waterflood recovery: LoSal EOR field evaluation*, SPE/DOE Improved Oil Recovery Symposium, Tulsa (2008).

[18] J.C. Seccombe, A. Lager, G.R. Jerauld, B. Jhaveri, T. Buikema, S. Bassler, J. Denis, K.J. Webb, A. Cocking and E. Fueg, *Demonstration of low-salinity EOR at interwell scale, Endicott Field, Alaska*, SPE Improved Oil Recovery Symposium, Tulsa (2010).

[19] A. Lager, K.J. Webb and C.J.J. Black, *Low salinity oil recovery - An experimental investigation*, Society of Core Analysts Meeting, Trondheim (2006).

[20] K.S. Sorbie and I.R. Collins, *A proposed pore-scale mechanism for how low salinity waterflooding works*, SPE Improved Oil Recovery Symposium, Tulsa (2010), SPE 129833.

[21] N. Kumar, L. Wang, I. Siretanu, M. Duits and F. Mugele, *Salt dependent stability of stearic acid Langmuir-Blodgett films exposed to aqueous electrolytes*, Langmuir 29 (2013), 5150-5159.

Chapter 2

Scientific background

Crude oil that is present in a reservoir rock interacts with pore walls with a large degree of complexity; rock grains have variable shapes with irregular surfaces, and the variety in absorbed clay minerals and polar compounds causes microscopic chemical and structural heterogeneity. In this chapter, we discuss the interaction of liquid drops with surfaces that are structured on very different length scales; the structure is either much smaller than or comparable to the drop size. These structured surfaces are particularly interesting because they allow for different drop shapes dependent on the surface wettability or the liquid volume. A decreased drop adhesion and increased exposure to external forces (due to release from confinement) might facilitate subsequent drop removal.

We start with a concise overview of the basic concepts of capillarity and wetting that are encountered throughout this thesis, and the wetting of microscopically textured surfaces. An extensive discussion of these two topics can be found in the book 'Capillarity and Wetting Phenomena' by de Gennes, Brochard-Wyart, and Quéré [1], and recent review papers by Quéré [2, 3] and Bonn *et al*. [4]. Morphological transitions on surfaces structured on the scale of the drop size are subsequently covered; we start with a discussion of general considerations, and continue with some examples of morphological transitions as described in recent literature. In this thesis, we rely on electrically induced variations in the contact angle to study the effect of wettability alterations. Hence, we conclude this chapter with a short overview of electrowetting [5].

2.1 Basic concepts of capillarity and wetting

2.1.1 Surface tension

Small liquid volumes tend to assume a perfectly spherical shape, and surface tension opposes the distortion of the surface by other forces. The physical origin of surface tension is shown in Figure 1A. A molecule that is segregated to the surface loses half its cohesive interactions with the bulk liquid and is thus in an energetically unfavorable state. As creation of new surface is energetically costly fluid systems tend to minimize their surface area. The surface tension is of order $\gamma \cong U/(2a^2)$, with U the cohesion energy per molecule and a^2 the area of the molecule, and is thus dependent on the type of cohesive force. Oils have a relative low surface tension of $\gamma \approx$ 20 mJ/m^2 due to van der Waals interactions, while water has a surface tension of $\gamma \approx$ 72 mJ/m^2 due to hydrogen bonding. An interface between two immiscible liquids is similarly characterized by an interfacial tension, which originates from different attractive intermolecular interactions in the liquids. Surface tension can also be expressed as a force per unit length (mN/m), where the line tension acts in all directions parallel to the surface.

2.1.2 Surfactants

The interfacial tension of a liquid in contact with air, a second liquid or a solid can be reduced by the use of so-called surfactants, *i.e.*, surface active agents. Surfactants are amphiphilic organic molecules, consisting of a hydrophobic and a hydrophilic group. The hydrophobic group of dissolved surfactants distorts hydrogen bonding between water molecules, thereby restricting their mobility; the driving force for adsorption to the interface is thus an increase of entropy of the solvent molecules. After creation of a fresh interface the interfacial tension gradually decreases from the value of the 'bare' interface to the equilibrium interfacial tension. The overall process involves various stages, such as diffusion of the surfactant molecules from the bulk to the interface, and adsorption and re-orientation at the interface. Figure 1B shows the example of stearic acid, which has a hydrophilic acid group that can dissociate depending on the pH of the solution, and a hydrophobic hydrocarbon tail. Stearic acid is used in Chapter 3 as a simple model compound for the variety of surfactants naturally present in oil reservoirs.

2.1.3 Laplace pressure

The interfacial tension causes a pressure difference between the interior and exterior of a curved interface. In Figure 2 we consider a small section of a liquid interface with principal

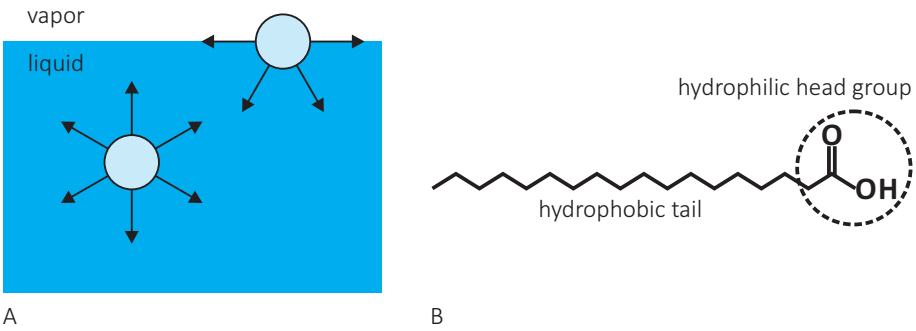

Figure 1 Interfacial tension of a liquid-vapor interface. (A) Liquid molecules and their cohesive interactions in the bulk and at the interface. (B) Stearic acid ($CH_3(CH_2)_{16}CO_2H$) is an example of a surfactant that reduces interfacial tension.

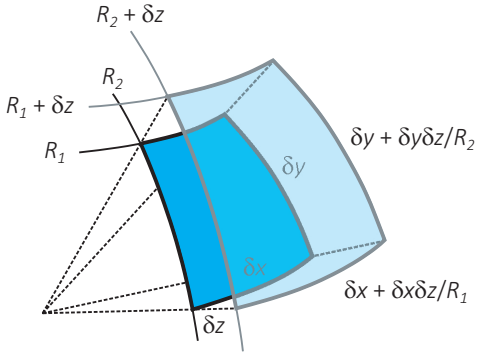

Figure 2 Determination of the Laplace pressure by dilating a liquid interface at constant pressure. Figure adapted from Bruus [6].

radii of curvature R_1 and R_2, which is displaced by an amount δz in the direction normal to the interface, at constant pressure. The work done by the capillary force and pressure is $\delta W = \gamma \delta A - \Delta p_L \delta V$, where the increase in interfacial area is $\delta A \cong \big((1/R_1) + (1/R_2)\big)\delta x \delta y \delta z$, and the increase in volume is $\delta V \cong \delta x \delta y \delta z$. The condition for mechanical equilibrium $\delta W = 0$ yields an expression for the Laplace pressure difference $\Delta p_L = p_A - p_B = \gamma\big((1/R_1) + (1/R_2)\big) = 2\gamma\kappa$, with κ the mean curvature of the interface. For spherical drops of radius R this reduces to $\Delta p_L = 2\gamma/R$. The Laplace pressure hence increases for decreasing drop size, and is typically comparable to atmospheric pressure for micron-sized drops.

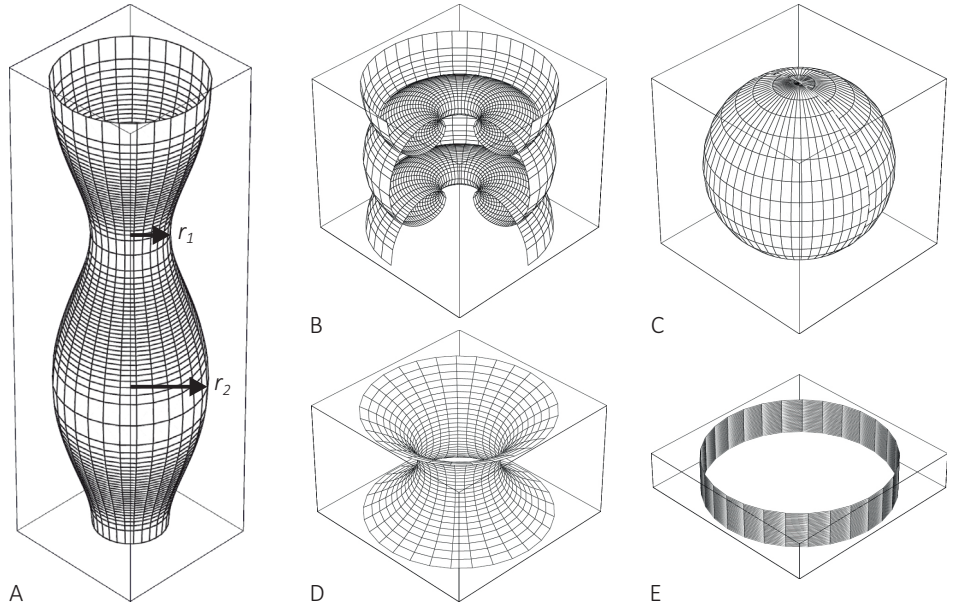

Figure 3 Examples of Delaunay surfaces. (A) Unduloid $\{r_1, r_2\}$, (B) nodoid $\{r_1, r_2\}$, (C) sphere $\{r_1 = 0, r_2\}$, (D) catenoid $\{r_1, r_2 = \infty\}$, and (E) cylinder $\{r_1, r_2 = r_1\}$. Figure adapted from Baret [7].

2.1.4 Constant mean curvature surfaces

In the absence of external forces, the constant pressure throughout the drop implies a constant mean curvature of the interface, which is a spherical shape for a free liquid volume. For the more general case of axisymmetric liquid volumes with boundary conditions, Delaunay [8] proved that constant mean curvature surfaces are obtained by rotating the roulettes of conics (*i.e.*, parabolic, elliptic, and hyperbolic catenaries). The thus obtained surfaces of revolution are catenoids, unduloids, and nodoids, in addition to the elementary cases of spheres and cylinders, and can be parameterized by the minimal radius r_1 and the maximal radius r_2 (Figure 3). Although the Delaunay surfaces are periodic surfaces, only portions of these surfaces are physically stable. Unduloids are unstable due to the Rayleigh-Plateau instability [9], while nodoids are unstable due to the intersecting surface. The necessary boundary conditions are provided by contacting solid substrates, for example in the case of a capillary bridge in between two planes or two spheres. In Chapter 5, we represent small oil volumes in rock pore spaces by the generic geometry of a drop confined between a sphere and a plane. We discuss the symmetry

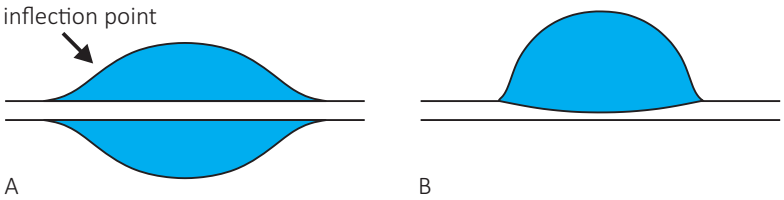

Figure 4 Competing morphologies of drops on fibers. Profile of a (A) barrel shape and (B) clamshell shape.

breaking of these liquid bridges with constant mean curvature above a volume- and separation-dependent critical contact angle.

The boundary conditions can also be provided by a cylindrical surface, a 'fiber'. We first assume that the liquid connects to the fiber surface at zero angle (Figure 4A). At the apex of the drop, both principal radii of curvature are of the order of the drop size R, resulting in a mean curvature $H \approx 1/R$. At the outer edge of the drop however, the radius of curvature perpendicular to the plane of the figure becomes very small, *i.e.*, equal to the radius of the fiber $r \ll R$. This implies that the radius of curvature in the plane of the figure should become negative, and the drop profile contains an inflection point. As can be seen in Figure 4A, the liquid surface again takes the shape of a Delaunay surface (unduloid), as expected for a cylindrically symmetric drop. Upon changing the angle between the liquid interface and the fiber surface, the so-called 'barrel' shape [10, 11] competes with a second constant mean curvature shape, the symmetry-broken 'clamshell' morphology (Figure 4B). Which of these morphologies is attained also depends on the volume of the drop and the history of the system [12].

2.1.5 Capillary length

While the interfacial tension tends to minimize the interfacial area of a drop, deformations in the shape can be induced by external forces. One can define the capillary length $\lambda = \sqrt{\gamma/\Delta\rho g}$, which is a characteristic length comparing the effects of interfacial tension and buoyancy. The capillary length is typically a few millimeters for liquid-vapor interfaces. For drops much smaller than λ, the surface force due to interfacial tension dominates the body force from gravitational acceleration, and a mean curvature shape is attained. In case of liquid/ liquid systems, the capillary length can be drastically increased *via* density matching of both liquid phases. For drops larger than λ, buoyancy effects should be taken into account. In Chapter 6 we investigate the influence of buoyancy

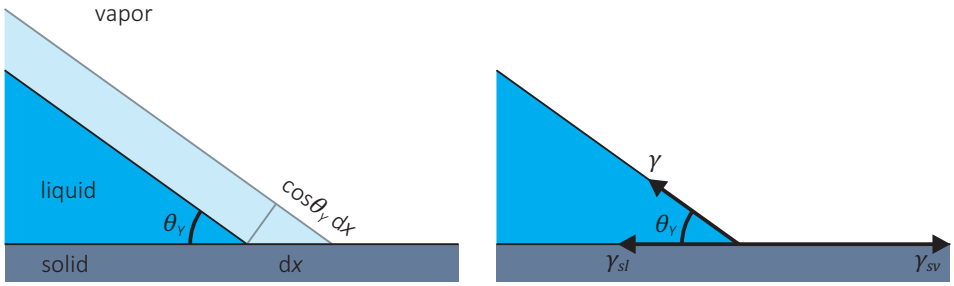

Figure 5 Determination of the Young angle *via* (A) energy or (B) force considerations.

forces on the morphological transitions of drops on fibers (Figure 4). Varying the mass density of the ambient phase allows for tuning of the capillary length in a broad range.

2.1.6 Young angle

When a liquid volume is placed on a chemically and topographically homogeneous planar surface, it either spreads completely or forms a liquid lens. In the latter case, the three phases that need to be considered – *i.e.*, the solid phase (s), the liquid phase (l), and the vapor (or a second, immiscible liquid) phase (v) – coexist at the three phase contact line, where the liquid-vapor interface makes an angle θ_Y with the surface. This Young angle can be derived by calculating the variation of the interfacial energy associated with a small reversible change in contact line position dx (Figure 5A). The variation is given by $dE = (\gamma_{sl} - \gamma_{sv})dx + \gamma \cos\theta\, dx$, with γ_{sv}, γ_{sl}, and γ the solid-vapor, solid-liquid, and liquid-vapor interfacial tension, respectively. In thermodynamic equilibrium the energy change is zero, which results in the Young relation $\cos\theta_Y = (\gamma_{sv} - \gamma_{sl})/\gamma$. The contact angle is thus determined by the chemical nature of the three phases. Alternatively, the Young angle can be derived from a balance between the equilibrium forces, *i.e.*, the interfacial tensions, in the horizontal direction at the three phase contact line (Figure 5B). The vertical components are responsible for deformations of liquid and soft solid substrates.

These global energy arguments yield the macroscopic contact angle. In the immediate vicinity of the three phase contact line, the slope of the liquid-vapor interface can deviate from the one described by the Young relation. At distances up to typically a few nanometers from the solid substrate, the local contact angle is affected by the disjoining pressure. Even closer to the surface, on a molecular scale, the interface position is no

longer uniquely determined due to thermal fluctuations and interface diffusiveness. However, in this thesis, we are only interested in the macroscopic contact angle.

2.1.7 Spreading parameter

Depending on the values of the interfacial tensions two wetting regimes can be distinguished that can be characterized by the spreading parameter $S = \gamma_{sv} - (\gamma_{sl} + \gamma)$, which compares the difference in interfacial energies of the dry and wet substrate. For $S > 0$, the energy of the system is minimized by complete wetting; the solid substrate is covered by a nanoscopic uniform liquid layer, of which the thickness is set by a competition between capillary forces and long range intermolecular forces (van der Waals interactions). Complete wetting is promoted by high-energy surfaces with large chemical binding energies, for low interfacial tension liquids such as light alkanes and silicon oils, and by the use of surfactants. For $S < 0$, the energy of the system is minimized by a drop with a finite contact angle satisfying the Young relation. The partial wetting regime is shown on low-energy surfaces, and can be divided in 'preferentially wetting' for contact angles smaller than $\pi/2$ (also called hydrophilic in case of water drops) and 'preferentially non-wetting' for contact angles larger than $\pi/2$ (hydrophobic). An interesting limit is found for $S < -2\gamma$, for which the drop is in a complete non-wetting situation. Complete non-wetting is highly desired for easy drop removal, and can be achieved in oil-water systems *via* complete wetting of the ambient phase.

2.1.8 Contact angle hysteresis

The derivation of the Young angle in Section 2.1.6 is based on the assumption of an 'ideal' surface, *i.e.*, a planar substrate that is both chemically and topographically homogeneous. However, real surfaces are non-ideal due to small chemical (*i.e.*, wettability) and physical defects. Due to these nanometric to micrometric heterogeneities, the contact angle is not uniquely defined. An example of such a defect is a sharp edge (Figure 6A), where the apparent angle between the liquid-vapor interface and the horizontal increases from θ to $\pi - \psi + \theta$, before the contact line proceeds. The dissipation upon depinning of the contact line is the fundamental mechanism of contact angle hysteresis.

Pinning of the contact line by small heterogeneities introduces an additional horizontal force that opposes the motion of the contact line (Figure 6B). As a result the contact line only advances (recedes) as soon as the advancing (receding) contact angle $\theta_a > \theta_Y$ ($\theta_r < \theta_Y$) is reached. The contact angle hysteresis is defined as the difference between these two angles, and the threshold force required to move a drop on such a surface is

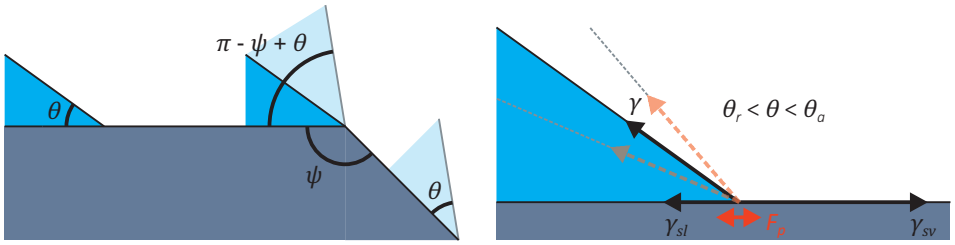

Figure 6 (A) On a sharp edge the apparent contact angle can assume any value between θ and $\pi - \psi + \theta$. (B) Due to contact line pinning, the apparent contact angle can assume any value between the receding and the advancing contact angle.

proportional to $\Delta \cos\theta = \cos\theta_r - \cos\theta_a$. 'Good', *i.e.*, clean and microscopically flat, substrates have a contact angle hysteresis smaller than 5°. The hysteresis of rough or dirty substrates, such as rock surfaces, is typically several tens of degrees, and can even become comparable to the advancing angle.

2.2 Wetting of microscopically textured surfaces

We now first consider the interaction of liquids with surfaces that are textured on scales much smaller than the drop size. The surface properties are dependent on roughness and wettability variations, *i.e.*, on the spatial variations in the geometry and the chemical properties. The presence of these defects not only results in contact angle hysteresis, but also affects the apparent contact angle and can induce different drop regimes.

2.2.1 Wenzel and Cassie-Baxter models

The apparent contact angle θ^* reflects the average properties of the substrate in the proximity of the contact line. For both topographically heterogeneous (structured) and chemically heterogeneous (patterned) surfaces, we are interested in θ^* as a function of the Young angle and the other parameters characterizing the substrate. A small displacement dx of the contact line parallel to the surface yields a change in surface energy. This variation is set to zero to find the equilibrium apparent contact angle.

A structured surface is characterized by its roughness factor $r > 1$, where r is the ratio of the actual surface area over the apparent one (Figure 7A). When the liquid follows all topological variations of the material, we find the Wenzel relation $\cos\theta^* = r\cos\theta_Y$. Surface roughness hence always 'magnifies' the underlying wetting properties. A

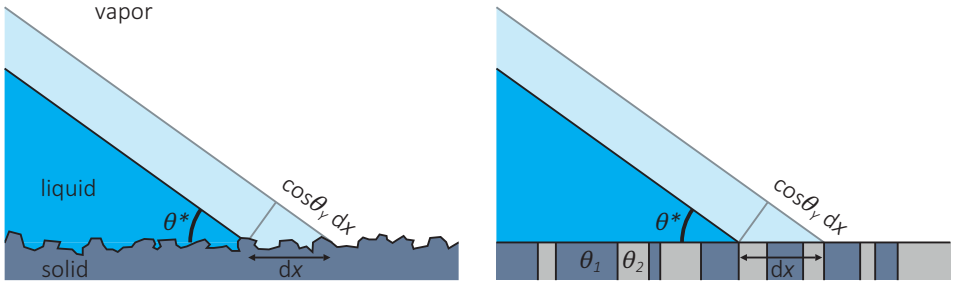

Figure 7 Edge of a drop placed on a (A) rough surface, yielding the Wenzel relation, and on a (B) chemically heterogeneous surface, yielding the Cassie-Baxter relation.

patterned surface consisting of two species with different wettability (Figure 7B) is characterized by the fractional surface areas of both species $f_1 + f_2 = 1$ and their respective contact angles θ_1 and θ_2. The apparent contact angle is then given by the Cassie-Baxter relation $\cos\theta^* = f_1 \cos\theta_1 + f_2 \cos\theta_2$, *i.e.*, it is obtained from a weighted average of the cosines of the angles of both species.

2.2.2 Superhydrophilic and superhydrophobic surfaces

The Wenzel relation predicts a critical roughness factor $r_c = 1/|\cos\theta_Y|$ at which complete wetting or complete drying is attained. However, the Wenzel model is only valid for moderate roughness factors, and hence these regimes cannot be induced by structuring of a surface. In the case of a very rough hydrophilic surface, part of the liquid will fill the microstructure. Drops spreading onto this impregnated state thus encounter a composite substrate with a solid and a liquid fraction (Figure 8A). For very rough hydrophobic surfaces, the liquid does not conform to the asperities of the substrate. Instead, air can remain trapped inside the structure, such that the drop sits on a composite substrate with a solid and a vapor fraction (Figure 8B). Drops deposited on either of these surfaces will thus have an apparent contact angle according to the Cassie-Baxter relation. Although liquid impregnation and air entrapment enhance hydrophilicity and hydrophobicity, respectively, the drop always partially contacts the solid substrate and is hence in the partial wetting regime. On superhydrophobic surfaces, the contact area with air can be increased by using a low solid fraction $f_s \approx 0.1$, resulting in an extremely low hysteresis and thus a large drop mobility.

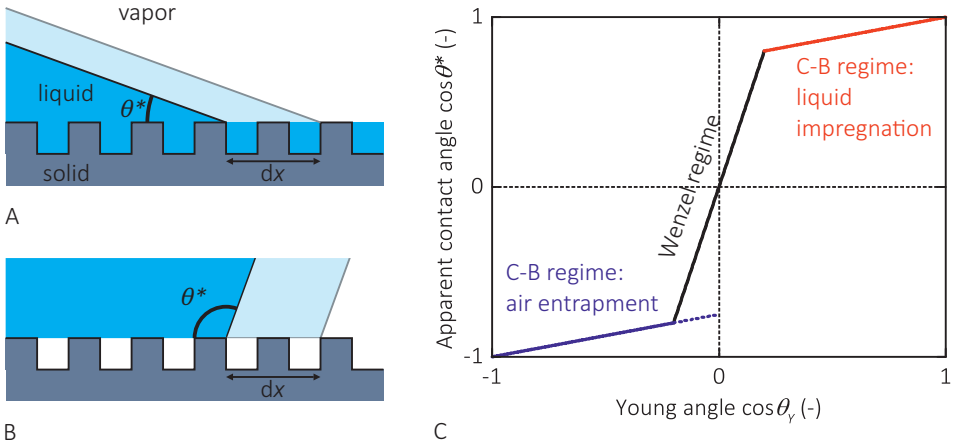

Figure 8 Wenzel and Cassie-Baxter regimes. In case of (A) superhydrophilic and (B) superhydrophobic surfaces, the liquid spreads on a composite surface. (C) Apparent contact angle as function of the Young angle for a pillared substrate with $f_s = 0.25$ and $r = 4$. The solid lines are based on the energy minimum, while the dotted line indicates the metastable Cassie-Baxter regime.

2.2.3 Coexisting states

The energies of drops that are satisfying either the Wenzel or the Cassie-Baxter relation can be compared to find the critical contact angle $\cos\theta_c = \pm(1 - f_s)/(r - f_s)$ separating both regimes. Figure 8C summarizes the results for a simple structured surface with well-defined pillars and without chemical heterogeneity. For hydrophilic surfaces, a large roughness implies a large θ_c and thus promotes liquid impregnation. For hydrophobic surfaces, a large roughness implies a small θ_c and thus promotes air entrapment.

The description of the superhydrophobic state is complemented by the necessary condition to satisfy the Young relation at all contact lines, *i.e.*, at the edge of the drop and for each liquid-vapor interface below the drop. The pinning of the contact line on sharp edges (Figure 6A) introduces an energy barrier $\gg kT$, and a metastable Cassie-Baxter regime for contact angles smaller than θ_c. Under these conditions, careful deposition of liquid results in a Cassie-Baxter drop, while vapor condensation yields a Wenzel drop with significantly smaller contact angle and larger contact angle hysteresis. This metastable Cassie-Baxter state is fragile; a transition to the lower energy Wenzel state can be easily induced by increasing the pressure. Impalement occurs either *via* depinning of the contact lines as soon as the angle of the liquid-vapor interfaces with respect to the vertical wall exceeds the Young angle, or *via* nucleation of solid-liquid contact on the bare substrate.

2.2.4 Defilling of random rough surfaces

Upon decreasing the wettability, a simple pillared substrate allows for transitions from the impregnated state, *via* the Wenzel regime, to the superhydrophobic state. In the latter regime, the substrate is completely dry and previously trapped liquid can be easily removed. Recently, Herminghaus showed that a similar (de)filling transition can be observed for a wide range of naturally occurring random rough surfaces [13, 14]. This defilling transition was proposed as a candidate mechanism for the increased recovery during low salinity water flooding. Initially, the oil is present in the roughness of the rock surfaces. It is suggested that upon increasing the contact angle for the oil during low salinity water flooding, the so-called 'Wenzel prewetting' line is crossed. The average thickness of the adsorbed oil film then jumps discontinuously from a finite value to zero, changing the situation from a thick liquid film filling the troughs of the surface, to a completely 'dry' (*i.e.*, oil depleted) surface. The oil then collects into large volumes that can be subsequently removed.

2.3 Morphological transitions

The transition from the Wenzel state to the Cassie-Baxter state on a microstructured surface thus has large consequences for liquid removal. However, besides microscale roughness and wettability variations, rock grains also exhibit larger-scale structuring. In this section, various types of morphological transitions are considered. We are now interested in drops positioned on structured or patterned surfaces, where the drops have a size comparable to the characteristic length scale of the topographic or chemical feature. Local instead of averaged geometry and wettability then govern the drop shape. We will first discuss general considerations concerning morphological transitions and then show some typical examples.

2.3.1 Determination of locally or globally stable equilibrium morphologies

Drops are considered for which the shape is determined entirely by minimization of the surface energy (given the boundary conditions provided by the bounding walls). The drop size can range from tens of nanometers to several millimeters, such that effects from molecular distances and line tension and the effects of gravity can be ignored. For a drop of liquid β deposited on a surface σ and surrounded by the vapor phase or an immiscible liquid α, the free energy functional is given by $F = \gamma A_{\alpha\beta} + \int_{A_{\sigma\beta}} dA\big[\gamma_{\sigma\beta}(x) - \gamma_{\sigma\alpha}(x)\big]$. Here, the solid-liquid and solid-vapor interfacial tensions can be position-dependent due

to (large scale) chemical heterogeneity, like the presence of adjacent surface domains from different materials.

To find locally or globally stable equilibrium morphologies of a certain amount of liquid, the interfacial free energy is minimized under the constraint of fixed volume, *i.e.*, the quantity $G = F - \Delta p_L V$ is minimized. The volume constraint is implemented using a Lagrange multiplier, which is the Laplace pressure difference between both fluid phases. A vanishing first variation of the energy with respect to small displacements of the liquid-vapor interface and associated displacements of the contact line yields two conditions for stationarity. The drop attains a mean curvature shape satisfying the Laplace equation $\Delta p_L = 2\gamma H$ and the contact line satisfies the Young equation $\cos\theta_Y = \left(\gamma_{\sigma\alpha} - \gamma_{\sigma\beta}\right)/\gamma$. However, these stationary states of the free energy could also correspond to a maximum or a saddle point of the free energy. Mechanical stability is only guaranteed if the second variation of the interfacial free energy is positive for small but arbitrary deformations of the liquid interface. Mechanically stable solutions and their stability limits can only be calculated analytically for highly symmetric shapes, such as liquid channels [15] and cylindrically symmetric barrel drops on fibers [12]. Numerical methods are used to study the existence and stability of non-axisymmetric drop morphologies. A widely used software application is Surface Evolver [16]. Within this numerical algorithm, the liquid-vapor interface is triangulated, and the total free energy is minimized under global (*e.g.*, constant volume) and local constraints using a conjugate gradient descent method. Some details of the numerical procedure, specific to the problems in this thesis, can be found in Eral *et al.* [12] and Chapter 6.

The minimum interfacial free energy shape depends in general on a number of external control parameters, which are the wettability – or wettabilities in case of patterned surfaces – of the solid substrate, and the geometry of the bounding surfaces. If the solid substrate has an intrinsic length scale, the volume of the liquid (rescaled with the cubic length scale) is such a parameter. Additional length scales of the substrate yield additional control parameters. Moreover, for topographically structured substrates with a sharp corner, the opening angle is of importance. These external control parameters can (ideally) be varied experimentally to induce changes in the attained shape. Due to the non-linearity of the underlying equations, one can in general observe several mechanically stable solutions. The transition between these different morphologies can be continuous or discontinuous, depending on the details of the interfacial free energy landscape. In the numerical calculations one can apply additional global constraints to the shape of the

liquid-vapor interface to get more insight in the behavior of the system. Frequently, the position of the center of mass of the liquid is a suitable parameter that distinguishes clearly between the different liquid morphologies.

2.3.2 Continuous and discontinuous transitions

In the following, two examples from this thesis are used to illustrate the differences between the two types of transitions. In the absence of pinning forces, the transitions between axisymmetric and non-axisymmetric liquid bridges in a sphere/ plane geometry are continuous (Chapter 5), while the transitions between barrels and clamshells on fibers are discontinuous (Chapter 6, see also Figure 4). The latter morphological transition also involves a transition in the topology of the interface, from multiply connected to simply connected. Yet this is not necessarily the case for all discontinuous transitions. In these examples, the contact angle is the relevant control parameter and the center of mass position x_{cm} is the parameter distinguishing the morphologies. The remaining control parameters (the liquid volume rescaled with the cubic radius of either the sphere or the fiber, respectively, and the sphere/ plane separation rescaled with the cubic radius of the sphere) are taken as constants. For clarity all interfacial free energies are taken relative to the axisymmetric shape at the corresponding contact angle.

2.3.2.1 Energy landscapes

Analysis of the so-called energy landscape, where the minimal interfacial free energy is plotted versus x_{cm} for several values of one of the control parameters (Figure 9), yields substantial insight in the nature of, and the conditions for the transitions. The minima in these graphs represent stable morphologies. Although the maxima also fulfill the Laplace and Young equations, these points have a negative second variation of the energy and thus represent unstable morphologies. If the curves (for every combination of the control parameters) have a single energy minimum, one only finds continuous transitions between the different morphologies. The transition occurs under the same conditions, *i.e.*, for the same values of the control parameters, in both directions, and is thus fully reversible. On the other hand, it is possible to find multiple energy minima for a range of the control parameters, in which case the transitions between the different morphologies are discontinuous. The local minima represent metastable configurations, which are separated from the global minima by means of an energy barrier. Thermal fluctuations are in general weak compared to these barriers, thus pronounced morphological hysteresis is found. The system remains in a metastable configuration until the energy barrier has been taken away, although a stable state with lower energy is possible. A consequence hereof is

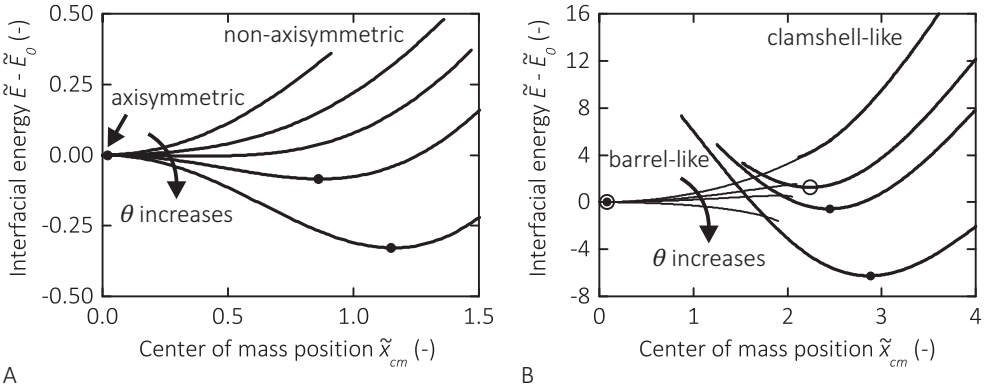

Figure 9 Energy landscape showing the minimal interfacial free energy versus center of mass position for several values of the contact angle. Filled points indicate global energy minima and open points indicate local energy minima. (A) Drops in a sphere/ plane geometry ($\tilde{V} = 1$ and $\tilde{s} = 0.5$) and (B) drops on a fiber ($\tilde{V} = 200$).

that the values of the control parameters where the morphological transition takes place depend on the path of the variation. Thus, a history dependence or hysteresis is found. In the intermediary regime, both morphologies are mechanically stable.

2.3.2.2 Bifurcation diagrams

Upon changes in the control parameter, the system attains a series of consecutive shapes corresponding to the (local) energy minima. The bifurcation diagram shows the evolution of x_{cm} of these attained shapes (Figure 10). The transition between different morphologies is characterized by a bifurcation of x_{cm}. The evolution of the center of mass position behaves differently for both morphologies, offering a clear distinction. In case of continuous transitions the morphology is stable up to the transition, and x_{cm} does not show a step-change at the instability. In case of discontinuous transitions the morphology can be metastable, and the transition does not occur until disappearance of the energy barrier. At that moment a step-change in x_{cm} is observed. The two examples in Figure 10 both represent a symmetry-breaking transition. One of the morphologies is axisymmetric, *i.e.*, $x_{cm} = 0$, while the other is non-axisymmetric. It should be noted that both morphologies can in principle break their symmetry in any azimuthal direction, which is not immediately clear from these two-dimensional diagrams.

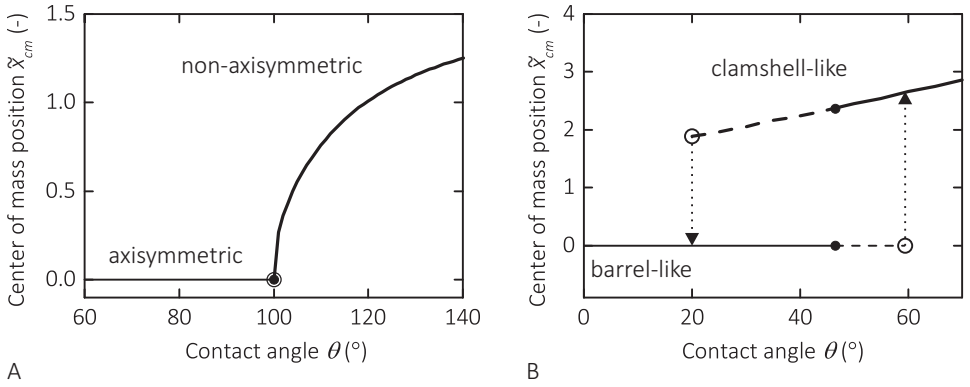

Figure 10 Bifurcation diagram showing the center of mass position of the liquid volume versus contact angle. All data correspond to the energy minimum for either an axisymmetric or a symmetry-broken state. The points of equal energy (closed symbols) and the transition points (open symbols) are indicated. (A) Drops in a sphere/ plane geometry ($\tilde{V} = 1$ and $\tilde{s} = 0.5$) and (B) drops on a fiber ($\tilde{V} = 200$).

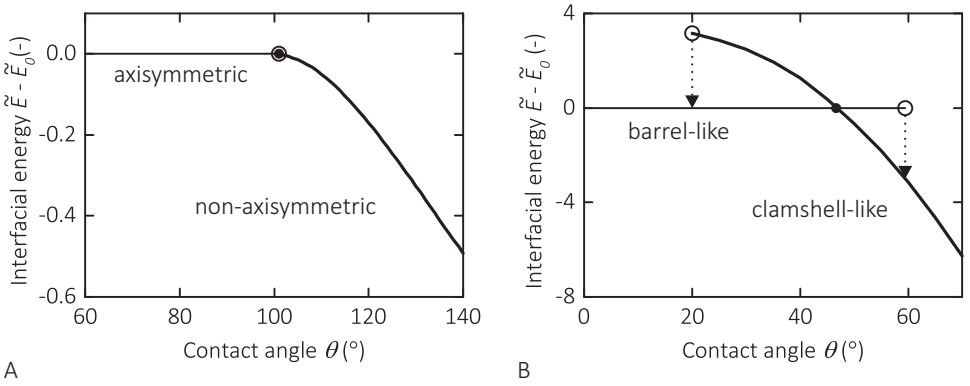

Figure 11 Interfacial free energy of the (quasi-)equilibrium drop shapes versus contact angle. The points of equal energy (closed symbols) and the transition points (open symbols) are indicated. (A) Drops in a sphere/ plane geometry ($\tilde{V} = 1$ and $\tilde{s} = 0.5$) and (B) drops on a fiber ($\tilde{V} = 200$).

Another representation is given by the evolution of the interfacial free energy upon changes in the control parameter (Figure 11). A transition between two morphologies takes places when the corresponding branches of the interfacial free energy either join smoothly (continuous transition) or intersect (discontinuous transition). In the latter case, the energy branch terminates upon disappearance of the minimum and the energy barrier, indicating that the morphology loses its stability.

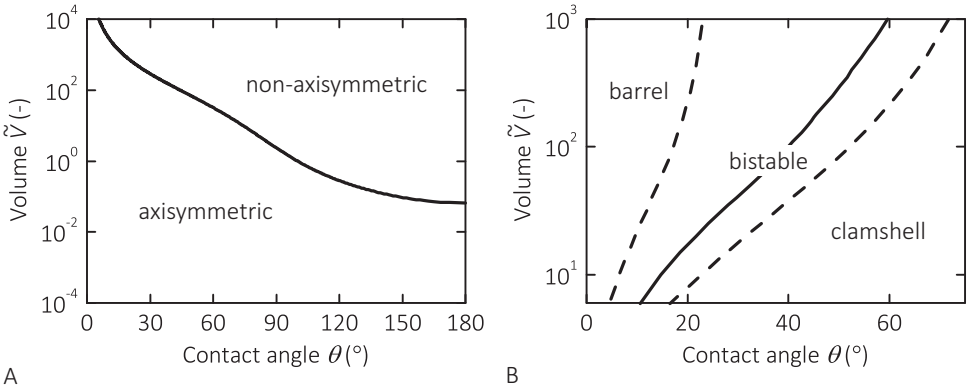

Figure 12 Morphology and instability diagrams in the $(\theta, \tilde{V})$ plane. Solid lines are morphological transition lines, and dashed lines are instability lines. (A) Drops in a sphere/ plane geometry ($\tilde{s} = 0.5$) and (B) drops on a fiber.

2.3.2.3 Morphology and instability diagrams

If the minimum interfacial free energy shape depends on more than one external control parameter, the analysis can be extended and the results can be summarized in morphology and instability diagrams (Figure 12). For discontinuous transitions, the instability lines indicate the stability limits of the morphologies and enclose a region where both morphologies are mechanically stable. The morphological transition line indicates the conditions for equal energy, and divides this region in two parts, in each of which one of the morphologies is stable and the other is only metastable.

2.4 Some examples of morphological transitions

In this section some representative examples of morphological transitions are discussed. Most transitions described in literature involve either a structured surface with kinks or a patterned surface with surface domains in a matrix with different wettabilities. In many cases, the large number of possible morphologies is a result of the immobilization of the three phase contact line, either at the corners of the topographic substrate or at the domain boundaries of the patterned substrate. However, not all morphological transitions rely on pinning of the contact line, amongst others the transitions for drops in a sphere/ plane geometry (Chapter 5) and for drops on fibers (Chapter 6).

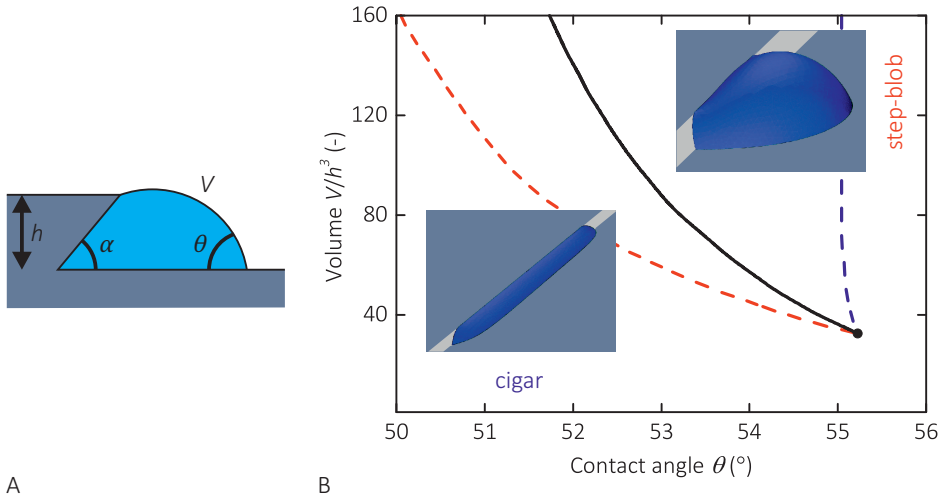

Figure 13 Morphological transitions on a topographic step. (A) Schematic of a topographic step wetted by a drop with constant cross section. (B) Morphology and instability diagram in the $(\theta, V/h^3)$ plane with $\alpha = \pi/2$. The diagram is shown for large volumes $V \gg h^3$ and for a narrow contact angle region above the spreading angle. The solid line is the morphological transition line, and the dashed lines are the instability lines. Figure adapted from Brinkmann *et al*. [17].

2.4.1 Structured surfaces

A comprehensive review covering wetting morphologies and their transitions on various simple structured substrates is given by Seemann *et al*. [18]. The spectrum and complexity of possible wetting morphologies increases with the number of kinks in the structure. One of the most fundamental topographies is an infinite wedge [19-22], which has no intrinsic length scale. The equilibrium drop shape then only depends on the opening angle α of the wedge and the contact angle θ of the underlying substrate material. The complexity is increased upon introducing a length scale to the problem *via* a step height h; the rescaled volume V/h^3 then represents the third relevant control parameter [17]. Grooves exhibit an even larger variety of possible wetting morphologies, as the equilibrium shape then also depends on the aspect ratio of the groove [23].

As an example, we consider the behavior for drops with large volumes $V \gg h^3$ on topographic steps (Figure 13A). For contact angles below the spreading angle $\theta_s = (\pi - \alpha)/2$, complete spreading of the liquid along the bottom edge of the step is observed. For contact angles above the spreading angle, the contact line becomes pinned to the upper edge of the step, and the liquid can attain different morphologies (insets

Figure 13B). The most common morphology is a drop sitting on the lower half plane beside the step ('step blob'). However, in a narrow region above the spreading angle one can observe elongated filaments of homogeneous cross section and positive Laplace pressure wetting a finite section of the step ('cigar'). Finally, at contact angles above $\theta_a = (\pi + \alpha)/2$, step blobs lose contact with the lower edge and an air wedge is found below the drop.

Figure 13B shows the morphology and instability diagram for an opening angle $\alpha = \pi/2$, for a narrow contact angle region above the spreading angle. A bifurcation point is found at a critical contact angle $\theta_c = 55°$ and a critical reduced volume $V_c/h^3 = 33$. For contact angles below θ_c, the transitions between filaments and drops upon volume changes are discontinuous. In contrast, for contact angles above θ_c, the system shows a gradual and smooth change from an extended drop in the wedge to a localized drop on the lower half-plane.

2.4.2 Patterned surfaces

Next, we consider chemically structured planar surfaces consisting of lyophilic domains γ ($\theta_\gamma < \pi/2$) in a more lyophobic matrix δ ($\theta_\delta > \theta_\gamma$). Surface domains with varying chemical heterogeneity can for example be created by microcontact printing, monolayer lithography, and vapor deposition through grids. In practice, the domain boundaries have a certain width, resulting in a gradually changing interfacial energy and thus a position-dependent contact angle. In theoretical studies, one generally considers the limit of zero width, such that the contact angle is a step function with a jump at the domain boundary.

2.4.2.1 Circular lyophilic surface domains

In case of two identical circular domains, the equilibrium morphology is determined by the wettabilities of the surface pattern and the total volume of the liquid (Figure 14) [24, 25]. Volume can be exchanged between the lyophilic domains to minimize the total free energy. Locally stable equilibrium morphologies need to satisfy the Laplace equation and, unless the contact line is pinned at the domain boundary, the Young equation. Next to three single-drop regimes, four two-drop regimes are found (of which one is only metastable), in which cases both drops have equal radii of curvature. This condition is complemented by the necessary stability criterion that at least one of the drops is pinned at the domain boundary with $\theta < \pi/2$. Otherwise, if one drop grows and the other shrinks by perturbative volume exchange, the resulting pressure difference would drive further volume transfer.

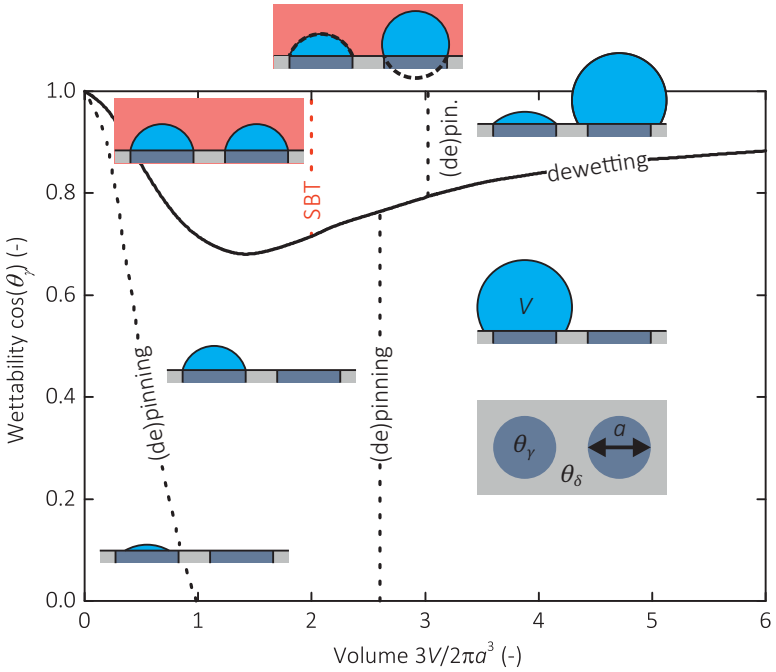

Figure 14 Morphological transitions on two identical lyophilic circular domains in a more lyophobic matrix. The morphology diagram shows the possible stable drop configurations (for $\cos\theta_\delta = -0.5$). Solid and dotted lines indicate discontinuous and continuous transitions, respectively. Only the morphological transition lines are shown. The symmetry breaking transition (SBT) is indicated in red. Figure adapted from Blecua *et al*. [25].

Three classes of phase transitions can be encountered, namely (de)pinning transitions where the contact line (de)pins from the domain boundary, dewetting transitions that involve dewetting of one of the lyophilic domains, and symmetry breaking transitions [25]. A symmetry breaking transition can occur when both drops are pinned at the domain boundary. Two equilibrium morphologies are then possible: a symmetric configuration with two identical drops with $\theta^{(1)} = \theta^{(2)}$, and an asymmetric configuration with two complementary drops with $\theta^{(1)} = \pi - \theta^{(2)}$. Upon increasing the volume, the stability criterion requires a symmetry breaking transition as soon as a contact angle $\theta = \pi/2$ is attained. This transition is only continuous for two drops on two lyophilic domains. For $N > 2$, the liquid exhibits a discontinuous transition from a state with N identical pinned drops to a state with one large pinned drop and $N - 1$ small pinned ones [24]. A linear array of N identical circular surface domains can be considered as a somewhat crude approximation for a lyophilic stripe [26], which will be discussed in the next section.

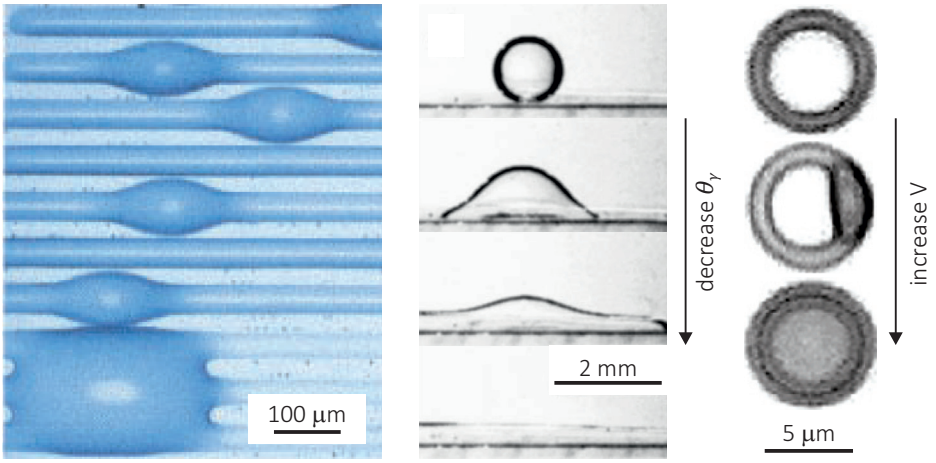

Figure 15 Bulging transitions on various lyophilic surface domains in a more lyophobic matrix. Upon increasing V or θ_Y, a transition from channels to bulges is found. (A) Completely wetting drops on long stripes. Figure adapted from Gau *et al*. [26]. (B) Partially wetting drops on a stripe electrode. Figure adapted from Klingner *et al*. [27]. (C) Drops on a ring-shaped surface domain. Figure adapted from Schäfle *et al*. [28].

2.4.2.2 Bulging on (in)finite lyophilic stripes

So-called bulging transitions were first observed by Gau *et al*. in the limit of completely wetting drops on asymptotically long stripes (Figure 15A) [26]. For small volumes, the liquid forms a channel with spatially constant cross section. A linear stability analysis indicates that such a cylindrical channel with pinned contact lines is locally stable for contact angles $\theta < \pi/2$ [26, 29]. Upon increasing the volume, the system undergoes a discontinuous transition to a heterogeneous state with a single bulge. Dependent on the wettability of the lyophobic matrix, the contact line of the bulge might detach from the domain boundary and move onto the lyophobic matrix. Similar bulging transitions were observed for partially wetting drops on long stripes (Figure 15B) [27, 30], for completely wetting drops on finite stripes [31], and for drops on ring-shaped surface domains (Figure 15C) [28], which can be considered as stripes with periodic boundary conditions.

In the case of finite wettability $\theta_Y > 0$ and long stripes [30], the ends of the liquid drop are bounded by short, transverse segments of contact line, which can move along the lyophilic domain (Figure 15B). The equilibrium morphology is then dependent on the wettabilities of the surface pattern and the volume of the liquid. For the channel to bulge transition, a bifurcation point $(\theta_{Y,c}, V_c)$ in the terms of the contact angle and the volume is found. For

small contact angles, the transition between the channel state and the bulge state upon variations in the volume is discontinuous, while for contact angles above the bifurcation point, a gradual and smooth change is obtained. In the case of complete wetting and finite stripe size, a bifurcation point in terms of the length to width ratio and the volume is found [31]. The height of the morphology only exhibits a discontinuous change upon changing the volume for long stripes.

2.5 Modifying wettability *via* electrowetting

Experimental validation of the numerically predicted instability diagrams can be achieved by variations in the external control parameters, of which most often the volume is chosen. Depositing various liquid volumes gives an indication of the instability lines; in the regime where two morphologies are mechanically stable, the attained morphology depends on the method of deposition. Thus, one could obtain a range of volumes where both morphologies are observed. The precise conditions for instability can only be obtained by gradually increasing and decreasing the liquid volume, either by condensation and evaporation, or *via* a small capillary in or near the substrate to add and remove liquid.

An additional control parameter for morphological transitions is the wettability of the substrate. Chemical modification of the substrate, for example by using self-assembled monolayers with different functional groups [32, 33], provides a means to vary the wettability. However, realizing specific values of the wettability within a wide range is difficult, the stability of these substrates can be poor, and – most importantly – the static nature again prevents precise determination of the instability lines. Active control of the liquids is possible when using electrowetting to modify the wettability. Electrowetting comprises the reduction of the macroscopic contact angle upon applying a voltage to a partially wetting conductive liquid drop on an electrode covered by a thin insulating layer (Figure 16). The contact angle can be tuned continuously and reversibly over a range of tens of degrees, which makes it a very convenient method for observing morphological transitions. In addition, the dynamic control provides the opportunity to study the dynamics of the transitions. In the following sections, some aspects of electrowetting are discussed with the focus on application of the technique. An extensive review on the basics of electrowetting is written by Mugele and Baret [5].

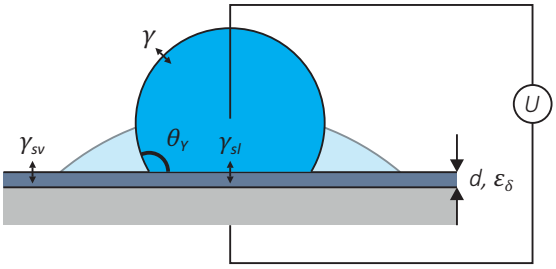

Figure 16 Electrowetting set-up: a partially wetting conductive drop is deposited on a planar substrate, consisting of an electrode covered by a thin insulating layer. Upon application of a potential to the electrode, the contact angle decreases.

2.5.1 Macroscopic picture of electrowetting

We consider a partially wetting drop on a planar substrate, which consists of an electrode covered by a thin insulating layer (Figure 16). A thin wire is immersed in the drop to keep the drop at ground potential. Upon application of a potential U to the electrode below the drop, an electric double layer builds up at the insulator-drop interface. The drop phase is assumed to be perfectly conductive, such that surface charges screen the electric field from the interior of the liquid. As long as the dielectric layer thickness *d* is much larger than the thickness of the Debye layer (a few nanometers), the contribution of the latter to the electric capacitance of the system can be neglected.

For drops smaller than the capillary length, gravity can be neglected and the free energy is composed of an interfacial contribution and an electrostatic contribution [5]. The electric field between the electrode and the drop is U/d as in a parallel plate capacitor. All other contributions to the electrostatic energy are negligible: the fringe fields in the vicinity of the contact line only yield a (very small) line energy, inside the drop the electric field vanishes, and next to the drop the electric field is only of order $U/R \ll U/d$. The total electrostatic energy is thus given by the volume integral over the density of the electric field in the dielectric layer $\int(\bar{E}\cdot\bar{D}/2)\,dV = \varepsilon_0\varepsilon_d U^2 A_{sl}/(2d) = cU^2A_{sl}/2$. Here, $\bar{E}$ and $\bar{D} = \varepsilon_0\varepsilon_d\bar{E}$ are the electric field and the electric displacement, ε_0 and ε_d are the vacuum permittivity and the dielectric constant of the insulator, A_{sl} is the solid/ liquid interfacial area, and $c = \varepsilon_0\varepsilon_d/d$ is the capacitance per unit area of the insulator. The total electrical work upon charging the capacitor consists of a positive work associated with building up the electrostatic energy in the capacitor and a negative work associated with charge leaving the battery. The free energy gain of the latter process is twice as large as the free energy cost of the former process, resulting in a net energy gain as charge is redistributed

from the battery (at constant potential) to the capacitor. The contact angle thus tends to decrease because spreading of the drop increases the capacitance, which allows for redistribution of additional charge.

The total free energy of the drop is thus given by $F = \gamma A + A_{sl}(\gamma_{sl} - cU^2/2 - \gamma_{sv})$. Since the gain in electrostatic energy is proportional to the solid/ liquid interfacial area, it can be combined with the solid-liquid interfacial tension to obtain an effective, voltage-dependent, solid-liquid interfacial tension ${\gamma_{sl}}^{eff} = \gamma_{sl} - cU^2/2$. It should be noted that the reduction only has an effective character, as the actual energy gain is taking place in the battery. Inserting this expression in the Young equation yields the voltage-dependent reduction of the macroscopic contact angle as defined by the electrowetting equation $\cos\theta = \cos\theta_Y + \eta$, where $\eta = cU^2/(2\gamma)$ is the dimensionless electrowetting number. The electrowetting number compares the strength of the electrostatic forces that tend to spread the drop, with surface tension forces that oppose spreading.

From the expression for the effective solid-liquid interfacial tension, one can interpret the quantity $f_{el} = cU^2/2$ as an electrostatic force per unit length pulling on the contact line. The localization at the contact line is however only valid macroscopically. The contact angle decreases gradually from θ_Y at the substrate to the macroscopic contact angle, over a distance of order d [34].

2.5.2 Implications for the experiments

Upon application of a potential, the macroscopic contact angle varies according to the electrowetting equation $\cos\theta = \cos\theta_Y + \eta = \cos\theta_Y + \varepsilon_0\varepsilon_d U^2/(2d\gamma)$. Taking into account the microscopic description, measurement of the macroscopic contact angle is only possible for drops with a size R much larger than the dielectric layer thickness d. We then obtain a linear relationship between the cosine of the contact angle and the squared voltage for sufficiently low voltages (typically for $\eta < 1$) (Figure 17). The electrowetting response is more pronounced for insulators with a larger dielectric constant and a smaller layer thickness, and for drops with a smaller interfacial tension.

Since electrowetting always reduces the contact angle of the conductive aqueous phase, the range of experimentally accessible contact angles can be increased by starting with a mostly non-wetting situation. This can be achieved by using a hydrophobic insulating layer, such as a fluoropolymer (*e.g.*, Teflon), or by covering an insulating layer with a very thin hydrophobic layer, for example a self-assembled monolayer. Water drops in air on Teflon exhibit a contact angle of about 120°, which can be further increased to about 160°

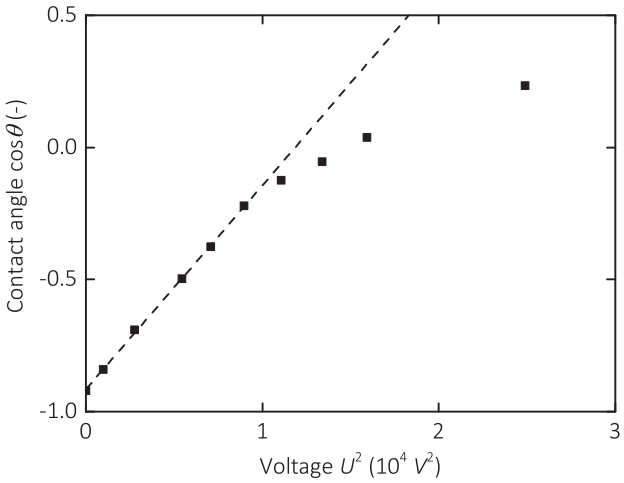

Figure 17 Example of an electrowetting curve showing $\cos\theta$ versus U^2. Data points are for a water drop on a Teflon surface in ambient silicon oil. The dashed line is a linear fit to the data at low voltages.

by using an ambient insulating immiscible oil phase. The presence of oil as a surrounding phase also reduces the contact angle hysteresis in the system from about 10° to a value below 2°.

Electrowetting can be performed with both DC and AC electric fields. Variations in the contact angle as a result of changes in the electric field are typically much faster than the hydrodynamic response of the drop, which typically takes 10 ms for millimeter-sized drops (corresponding to 100 Hz in the frequency domain). If an AC electric field with a frequency much larger than the hydrodynamic response of the drop is used, the contact angle reduction depends on the time average of the applied voltage. Thus, the root mean square (RMS) value is used in the electrowetting equation. AC electric fields are often preferred over DC fields as they minimize charge accumulation and reduce contact angle hysteresis [35]. When using an AC electric field, one needs to be careful that the assumption of a perfect conductor is still valid [5]. Beyond a conductivity-dependent critical frequency, dissolved ions cannot follow the applied field, and the electric field penetrates substantially into the drop. The liquid then behaves as a dielectric, and actuation is only possible with dielectric body forces. For the purpose of this thesis, we only consider experimental frequencies below the critical frequency.

The electrowetting equation predicts a transition from partial wetting to complete wetting at a critical electrowetting number $\eta_c = 1 - \cos\theta_Y$. This transition has never been observed experimentally, since for larger voltages the contact angle response deviates from the ideal behavior (Figure 17). The reason why the contact angle becomes independent of the applied voltage is not yet fully understood, however, a non-linear response of the dielectric material to strong electric fields in the vicinity of the contact line is believed to be the origin of this so-called 'contact angle saturation'. For water drops in oil on Teflon, the saturated contact angle is generally about 60°.

When using electrowetting as a tool to change the wettability while studying morphological transitions, one can either use a water-in-oil or an oil-in-water system. The choice is dependent on the value of the contact angle at which the transition is expected, and experimental circumstances. For water drops in ambient oil on Teflon, the contact angle decreases from 160° to 60° upon electrowetting, thus for oil drops in water, the (complementary) contact angle increases from 20° to 120°. As the water phase is kept at ground potential, using a water-in-oil system requires the presence of a thin wire electrode in the drop. This can be avoided by using an oil-in-water system, which however increases the chances of dielectric breakdown. Ideally, the insulating layer only shows dielectric breakdown at a sufficiently high voltage that is dependent on the material and the layer thickness. Nevertheless, small defects in the insulating layer cause breakdown, and thus electrolysis, at lower voltages.

References

[1] P.-G. De Gennes, F. Brochard-Wyart and D. Quere, *Capillarity and wetting phenomena: Drops, bubbles, pearls, waves*, Springer Science (2004).

[2] D. Quere, *Non-sticking drops*, Rep. Prog. Phys. 68 (2005), 2495-2532.

[3] D. Quere, *Wetting and roughness*, Ann. Rev. Mater. Res. 38 (2008), 71-99.

[4] D. Bonn, J. Eggers, J. Indekeu, J. Meunier and E. Rolley, *Wetting and spreading*, Rev. Mod. Phys. 81 (2009), 739-805.

[5] F. Mugele and J.C. Baret, *Electrowetting: From basics to applications*, J. Phys. Condens. Matter 17 (2005), R705-R774.

[6] H. Bruus, *Theoretical Microfluidics*, Oxford University Press (2008).

[7] J.C. Baret, *Morphological transitions in simple electrocapillary systems - Tools for microfluidic liquid manipulation*, PhD thesis, University of Twente (2005).

[8] C. Delaunay, *Sur la revolution dont la courbure moyenne est constante*, 6 (1841), 309-319.

[9] D. Langbein, *Capillary surfaces: Shape - stability - dynamics, in particular under weightlessnes*, Springer (2002).

[10] B.J. Carroll, *Equilibrium conformations of liquid-drops on thin cylinders under forces of capillarity - a theory for the roll-up process*, Langmuir 2 (1986), 248-250.

[11] G. Mchale and M.I. Newton, *Global geometry and the equilibrium shapes of liquid drops on fibers*, Colloids Surf. A 206 (2002), 79-86.

[12] H.B. Eral, J. De Ruiter, R. De Ruiter, J.M. Oh, C. Semprebon, M. Brinkmann and F. Mugele, *Drops on functional fibers: From barrels to clamshells and back*, Soft Matter 7 (2011), 5138-5143.

[13] S. Herminghaus, *Universal phase diagram for wetting on mesoscale roughness*, Phys. Rev. Lett. 109 (2012), 236102.

[14] S. Herminghaus, *Wetting, spreading, and adsorption on randomly rough surfaces*, Eur. Phys. J. E 35 (2012), 43.

[15] P. Lenz and R. Lipowsky, *Stability of droplets and channels on homogeneous and structured surfaces*, Eur. Phys. J. E 1 (2000), 249-262.

[16] K.A. Brakke, *The Surface Evolver*, Exp. Math. 1 (1992), 141-165.

[17] M. Brinkmann and R. Blossey, *Blobs, channels and "cigars": Morphologies of liquids at a step*, Eur. Phys. J. B. 14 (2004), 79-89.

[18] R. Seemann, M. Brinkmann, S. Herminghaus, K. Khare, B.M. Law, S. Mcbride, K. Kostourou, E. Gurevich, S. Bommer, C. Herrmann and D. Michler, *Wetting*

morphologies and their transitions in grooved substrates, J. Phys. Condens. Matter 23 (2011), 184108.

[19] P. Concus and R. Finn, *On behavior of a capillary surface in a wedge*, Proc. Natl. Acad. Sci. 63 (1969), 292-299.

[20] D. Langbein, *The shape and stability of liquid menisci at solid edges*, J. Fluid Mech. 213 (1990), 251-265.

[21] P. Concus and R. Finn, *Discontinuous behavior of liquids between parallel and tilted plates*, Phys. Fluids 10 (1998), 39-43.

[22] K. Khare, M. Brinkmann, B.M. Law, E.L. Gurevich, S. Herminghaus and R. Seemann, *Dewetting of liquid filaments in wedge-shaped grooves*, Langmuir 23 (2007), 12138-12141.

[23] R. Seemann, M. Brinkmann, E.J. Kramer, F.F. Lange and R. Lipowsky, *Wetting morphologies at microstructured surfaces*, Proc. Natl. Acad. Sci. 102 (2005), 1848-1852.

[24] P. Lenz and R. Lipowsky, *Morphological transitions of wetting layers on structured surfaces*, Phys. Rev. Lett. 80 (1998), 1920-1923.

[25] P. Blecua, M. Brinkmann, R. Lipowsky and J. Kierfeld, *Morphological transitions of liquid droplets on circular surface domains*, Langmuir 25 (2009), 13493-13502.

[26] H. Gau, S. Herminghaus, P. Lenz and R. Lipowsky, *Liquid morphologies on structured surfaces: From microchannels to microchips*, Science 283 (1999), 46-49.

[27] A. Klingner and F. Mugele, *Electrowetting-induced morphological transitions of fluid microstructures*, J. Appl. Phys. 95 (2004), 2918-2920.

[28] C. Schäfle, M. Brinkmann, C. Bechinger, P. Leiderer and R. Lipowsky, *Morphological wetting transitions at ring-shaped surface domains*, Langmuir 26 (2010), 11878-11885.

[29] R.L. Speth and E. Lauga, *Capillary instability on a hydrophilic stripe*, New J. Phys. 11 (2009), 075024.

[30] M. Brinkmann and R. Lipowsky, *Wetting morphologies on substrates with striped surface domains*, J. Appl. Phys. 92 (2002), 4296-4306.

[31] D. Ferraro, C. Semprebon, T. Toth, E. Locatelli, M. Pierno, G. Mistura and M. Brinkmann, *Morphological transitions of droplets wetting rectangular domains*, Langmuir 28 (2012), 13919-13923.

[32] T.P. Sullivan and W.T.S. Huck, *Reactions on monolayers: Organic synthesis in two dimensions*, Eur. J. Org. Chem. (2003), 17-29.

[33] C. Haensch, S. Hoeppener and U.S. Schubert, *Chemical modification of self-assembled silane based monolayers by surface reactions*, Chem. Soc. Rev. 39 (2010), 2323-2334.

[34] F. Mugele and J. Buehrle, *Equilibrium drop surface profiles in electric fields*, J. Phys. Condens. Matter 19 (2007), 375112.

[35] F. Li and F. Mugele, *How to make sticky surfaces slippery: Contact angle hysteresis in electrowetting with alternating voltage*, Appl. Phys. Lett. 92 (2008), 244108.

Chapter 3

Influence of cationic composition and pH on the formation of metal stearates at oil-water interfaces

We study the formation of layers of metal stearates at the interface between a decane solution of stearic acid and aqueous salt solutions of variable composition and pH by monitoring the evolution of their mechanical, optical, and chemical properties as a function of time after formation of the interface. For values of the pH below the pK_a of stearic acid hardly any interfacial activity is observed. For pH $>$ pK_a, stearic acid deprotonates at the interface and forms metal stearates, eventually leading to the formation of macroscopic solid layers. Dynamic interfacial tension measurements reveal that the process takes place in several stages, which we attribute to the successive formation of dilute and dense monolayers followed by three-dimensional growth. In the presence of divalent ions, the solid layers display a significant increase in the dilatational storage modulus. Experiments performed with an aqueous phase containing multiple cation species (artificial seawater) give rise to particularly pronounced growth of solid layers, which preferentially incorporate Ca^{2+} as revealed by X-ray photoelectron and infrared spectroscopy. Our results highlight in particular the importance of the complex synergistic effects of simultaneously present monovalent and divalent cation species on the interfacial adsorption.

This chapter has been published as R. de Ruiter, R.W. Tjerkstra, M.H.G. Duits and F. Mugele, *Influence of cationic composition and pH on the formation of metal stearates at oil-water interfaces*, Langmuir 27 (2011), 8738-8747. Barbara Mojet (Catalytic Processes and Materials, University of Twente) is kindly acknowledged for IR spectroscopy and Arun Banpurkar for layer preparations.

3.1 Introduction

The formation of adsorbed layers at oil-water interfaces can have a strong influence on the stability of emulsions as well as on the flow of two-phase fluids in microchannels or porous media. This makes it an interesting case from both fundamental scientific and application oriented viewpoints. Application areas include geology and environmental sciences, biology, and food science.

A prominent example is found in oil recovery, where such layer formation can cause problems. Here, the extensive contact between crude oil and injection water allows organic acids from the oil to react across the interface with cations in the water. This leads to the formation of interfacial layers of metal soaps, which can then act as stabilizers for emulsified oil drops. Such an emulsification can seriously hamper the oil-water separation. In addition, also solid agglomerates of metal stearates can be formed, leading to blockage of pores in the rock [1, 2]. Besides problems, interfacial layer formation can also offer opportunities. Examples hereof are found in the food industry, where microscopic bubbles or droplets are stabilized using solid-like layers of proteins, polymers, or particles. In connection to these applications, also fundamental studies have been performed, focusing at either planar [3, 4] or curved [5-8] interfaces.

However, relatively few studies have been aimed at the *in situ* formation of interfacial solid layers *via* reaction, nucleation, and growth processes at the oil-water interface [9-11]. More insight into the formation mechanism and the physical properties of such layers is therefore needed: both to solve problems with unwanted layer formation and to enable possible new applications, like droplets or bubbles coated with a layer of tunable thickness and/ or mechanical properties.

An obstacle in obtaining such insights, especially in biologically and geologically oriented studies, is the enormous complexity generated by the composition of the involved materials. These compositions are often dictated by practice. For example, most biological cells (stabilized by lipid bilayers) need to be in an environment that contains various ions in a specific composition. Even slight disturbances thereof can cause the cell to disfunction or die. Another example is found in oil recovery, where crude oil containing a variety of complex molecules with diverse physicochemical properties [12-14] is exposed to aqueous fluid containing many different ions. In this case the ionic composition of the water can be adapted to increase the recovery efficiency [15, 16]. However, the mechanism(s) underlying this effect are still poorly understood.

These examples underline the need to address the role of phase composition in the formation of interfacial layers. Again, relatively few studies have been performed. Most of the existing work is focused on comparing different individual ions in their effects on surfactant adsorption and/ or layer formation. Examples are the papers by Brandal *et al.* [1, 17] and Havre *et al.* [2], who studied the formation of interfacial layers between naphthenic acid from oil and divalent cations from the aqueous phase. Also some studies on interfacial charging due to adsorption of ionic species have been reported [18-20]. However, how the insights obtained from studies with individual (cat/ an)ions translate to the case of their mixtures remains to be seen. For example, ions of the same charge could compete with each other, perhaps following a Hofmeister series [21], but alternatively they might also show synergistic effects.

To contribute to this underexplored field, we performed an experimental study aimed at the formation of solid interfacial layers, with particular focus on the role of the aqueous phase composition. The latter is varied extensively *via* the pH, the salt concentration, and the occurrence of mono- and divalent cations. Various combinations of cations are considered, from individual types like Na^+, Mg^{2+}, and Ca^{2+} to the complexity of artificial seawater [22]. To reduce the complexity of the overall system, the oil phase is represented by a model fluid of stearic acid ($CH_3(CH_2)_{16}COOH$) dissolved in *n*-decane ($CH_3(CH_2)_8CH_3$).

Fatty acid monolayers spread at the water-air (W/A) interface have been studied for many different aspects: the orientation and ordering of the molecules [23, 24], incorporation of metal ions in the film [25-27], formation of super lattice structures [28-30], viscoelastic properties [31, 32], phase transitions [33-36], film stability [37], Langmuir-Blodgett mono- and multilayer deposition [24, 38, 39], and monolayer collapse [40-44]. The behavior of fatty acids at water-oil (W/O) interfaces has been investigated much less often, and studies have mainly been restricted to their absorption behavior [1]. Interestingly, the case of water in contact with oil presents additional degrees of freedom, like the solubility of surfactants and/ or their precursors in bulk oil. This means that the formation of interfacial layers might also occur *via* different mechanisms.

We follow the interfacial behavior of the stearic acid molecules and their associated metal complexes by performing dynamic (*i.e.*, time dependent) interfacial tension measurements using the pendant drop technique. Different stages of layer formation will be identified and discussed, based on the signature of the interfacial tension and its dependence on the compositions of the oil and the aqueous phase. The ultimately formed

layers are mechanically characterized *via* the interfacial dilatational moduli, while the elemental composition and the presence of specific functional groups are accessed by X-ray photoelectron and infrared spectroscopy.

In particular, we will demonstrate that layer formation of metal stearates occurs through distinct stages. Deprotonation of the stearic acid is an enabling step for the whole sequence. For subphases containing both mono- and divalent cations, the formation is initiated by the monovalent ions, while in later stages the divalent ions become dominant. As a result, in the mixtures layers are formed through a kinetics that is different than that for the individual valencies, but always leading to thick solid layers in the end.

3.2 Materials and methods

3.2.1 Chemicals and solutions

All chemicals are purchased from Sigma-Aldrich. Ultrapure water with a resistivity of 18.2 MΩ·cm is obtained from a Millipore Synergy UV instrument. Artificial seawater [22] (see Table 1 for the composition) is prepared by mixing solutions of individual salts of ACS reagent grade. The pH of this solution varies between 7.5 and 8.0. Aqueous phase samples of the individual salts $CaCl_2$, $MgCl_2$, and NaCl are prepared at 1M and diluted to the required concentrations, after which the pH is adjusted with KOH or HCl. To remove any undissolved impurities, all salt solutions are passed through a 1 μm filter. Anhydrous *n*-decane (purum grade, viscosity 0.9 mPa·s) is cycled five times through a column with basic aluminum oxide (150 mesh) to remove surface active impurities that might originate from native residues or oxidation processes [45]. A 1 mM stearic acid (StA) stock solution in *n*-decane is prepared and diluted to the required concentrations.

3.2.2 Dynamic interfacial tension experiments

Pendant drop experiments are executed with an OCA 20L contact angle measuring and contour analysis system and analyzed with SCA 22 pendant drop software (both from DataPhysics). During and after injection of a drop of aqueous phase with a volume of 10-30 μL into a large amount of ambient oil phase, a movie is recorded at 50 frames/s. The time required to make a stable drop amounts to 1 s. The video recording allows to monitor the layer formation at the water-decane interface online from the moment it becomes visible and to obtain the evolution of the interfacial tension (IFT) offline. The latter is achieved by fitting the contour of the drop to the Young-Laplace equation

Table 1 Composition of artificial seawater.

type of cation	salt	concentration in aqueous solution (mM)
monovalent	NaCl	426
	Na_2SO_4	29.4
	KCl	9.45
	$NaHCO_3$	2.43
	KBr	0.857
	H_3BO_3	0.438
	NaF	0.0744
divalent	$MgCl_2{\cdot}6H_2O$	55.5
	$CaCl_2{\cdot}2H_2O$	10.8
	$SrCl_2{\cdot}6H_2O$	0.0937

combined with the hydrostatic pressure equation. Bond numbers (the ratio between buoyancy and interfacial tension forces) vary generally from 0.1 to 1, which enables this approach [46]. Since the drops have typical curvature radii in the millimeters range, the obtained IFTs generally compare well to those measured for truly planar interfaces [47].

3.2.3. Interfacial rheology experiments

To investigate the onset and advancement of dilatational surface viscoelasticity, oscillating drop experiments are executed with the OCA 20L with an ODG20 oscillating droplet generator extension and analyzed with SCA 26 oscillation/ relaxation software (DataPhysics). A pendant drop of aqueous phase with a volume of 15-25 µL is formed in an ambient oil phase. A movie is recorded at 50 frames/s while the drop volume is oscillated sinusoidally at 1 Hz driven by a piezo element. The frequency of 1 Hz was chosen slightly higher than usual for this type of measurement [48] to obtain a better time resolution in measuring the transient phenomena in layer formation. Consequently, the measured interfacial moduli can become slightly overestimated [49]. In our case, a reference measurement on a bare water/decane interface (at 1 Hz) gave E' values $\ll$ 5 mN/m, which is indeed nonzero, but still much smaller than the values found for our solid interfacial layers.

The time-dependent drop area and interfacial tension (IFT) are extracted from the contour of the drop in individual movie frames. The relative interfacial area variation $\mathrm{d}A/A$ is kept

below 0.05 to remain in the linear viscoelastic regime. From the mean values and amplitudes of the sinusoidal oscillations in drop area (A_0 and $\bar{A}$) and interfacial tension (γ_0 and $\bar{\gamma}$) and the phase shift (δ) between the two responses, the average IFT and the dilatational interfacial moduli are determined $E^* = E' + iE'' = \left(\bar{\gamma}/(\bar{A}/A_0)\right)e^{i\delta}$ [50, 51], where E', the interfacial dilatational storage (elastic) modulus, measures the energy stored during a periodic deformation of the interface, and E'', the interfacial dilatational loss (viscous) modulus, accounts for energy dissipation due to relaxation processes. Measurements of E' and E'' are performed in 10 s intervals, using five oscillation cycles per measurement.

3.2.4 Multilayer preparation

Layers are allowed to form for 2 h at a planar interface between an aqueous phase and a solution of stearic acid in decane. After transfer to a silicon wafer by dipping and retracting the latter, the sample is washed with ultrapure water to remove excess salt and subsequently air-dried before characterization. Because of the rapidly evolving, initially very thin and fragile layers at the liquid-liquid interface, we have only been able to transfer and analyze the layers in stage 6. These layers are characterized by scanning electron microscopy, X-ray photoelectron spectroscopy, and infrared spectroscopy.

3.2.5 Scanning Electron Microscopy

SEM micrographs are made in a JEOL 5610 field emission gun SEM, using an acceleration voltage of 0.55 kV and an in-lens detector.

3.2.6 X-ray Photoelectron Spectroscopy (XPS)

The XPS measurements, in which the elemental composition of the sample is measured from the kinetic energies of the electrons that escape upon X-ray irradiation, are performed using a Quantera SXM instrument (Physical Electronics).

3.2.7 Infrared (IR) Spectroscopy

IR absorption spectroscopy is performed on the layers transferred to a silicon wafer. Reference spectra for pure stearic acid and pure calcium stearate (CaSt) are obtained by grinding these compounds with KBr powder and pressing the mixture into a pellet. The IR measurements are performed using a Tensor FTIR spectrometer (Bruker). The presence of functional groups is identified by comparison of peaks with the reference samples and with literature data.

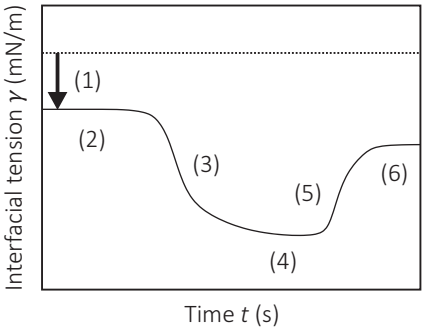

Figure 1 Typical evolution of the interfacial tension after an aqueous salt solution and a stearic acid solution in decane are brought into contact. The horizontal dashed line indicates the IFT of the pure water/ decane interface.

3.3 Results

3.3.1 Distinct stages in the formation of interfacial layers

The behavior of the interfacial tension as a function of the time lapsed after the first contact between aqueous salt solution and stearic acid in decane turns out to be qualitatively similar in most cases. It comprises a number of steps, which are illustrated in Figure 1. After creating a fresh water-oil interface, one can observe an instantaneous IFT decrease (1) from the tension of pure water-decane to a plateau (2) with an IFT value that depends on the compositions of the fluids. The actual decline cannot be observed due to the finite formation time of the pendant drop. The existence of a plateau is suggestive of an adsorption equilibrium. At the end of the lag time, a sharp decrease in IFT (3) is observed, indicating a rapid and drastic change, which we interpret as a structural transition (see Section 3.4). Then after a period with minor IFT changes (4), the IFT increases again (5). Sometimes this increase evolves to another plateau value (6). The characteristic times of the successive stages and the values of the IFT acquired depend on the compositions of the aqueous phase and the oil phase. The conditions also determine when the formation of an interfacial layer becomes visible to the naked eye. In experiments in which both [StA] and pH are high, layer formation is already observed in stage 3, while in experiments with low [StA], layer formation is only observed at the end of stage 5.

The decrease and subsequent increase of the IFT in stages 3-5 is often such a strong effect that it can be directly observed from the stretching and subsequent retraction of the drop

(at constant volume) in the image-time series. This confirms that the formation of a visible surface layer initially does not interfere too much with the optical measurement of the drop contour (as needed to calculate the 'IFT'). Dependent on the conditions, very thick solid layers can be observed at the end of stage 5. Under these conditions a reliable IFT cannot be obtained from the fitted drop contour. Apparent IFT data that are affected by this uncertainty are excluded from our analysis.

3.3.2 Effect of stearic acid concentration and pH

The interfacial tension of the bare decane-water interface is close to 50 mN/m. When drops of demineralized water are formed in ambient decane with stearic acid concentrations ranging from 1 to 1000 μM, the IFT shows only a minor instantaneous effect. Subsequently, we find a weak decrease in interfacial tension with time, which depends weakly on the StA concentration in the oil phase (results not shown). On the basis of earlier observations with liquids that were used as received, we attribute this slowly decreasing IFTs to either remaining impurities in the system (in the aqueous phase or in the purified decane) or to very small amounts of adsorbed StA. In any case, it is clear that the stearic acid is barely interfacially active when dissolved in oil and brought into contact with demineralized water.

However, when artificial seawater is used to form the drops, the stearic acid dissolved in the decane does show interfacial activity, and the characteristic IFT response can be observed (Figure 2A). For [StA] $\leq$ 10 μM, the interfacial tension decreases only slightly with time. The amount of stearic acid might be too low to induce multilayer formation; however, one might also argue that the system is still in its lag time at the end of the experiment. However, for [StA] $\geq$ 30 μM the stages 1-5 can clearly be discerned (compare Figure 2A with Figure 1). For [StA] $>$ 100 μM the formation of an interfacial layer even becomes visible to the naked eye within 1000 s (the typical duration of our experiments). Our observations clearly indicate that with increasing stearic acid concentration the IFT value at the plateau, the lag time, and the achieved minimum IFT all decrease, while the steepness of the IFT decrease and the extent of layer formation increase.

The difference in behavior for drops of demineralized water and ASW could be caused by differences in the ionic strength, the presence of specific ions, or the pH. While demineralized water has a pH of about 5.5 due to dissolution of carbon dioxide from the air, artificial seawater has a slightly elevated pH (~7.5-8) due to the presence of sodium bicarbonate. To investigate the effect of pH, drops of artificial seawater at various

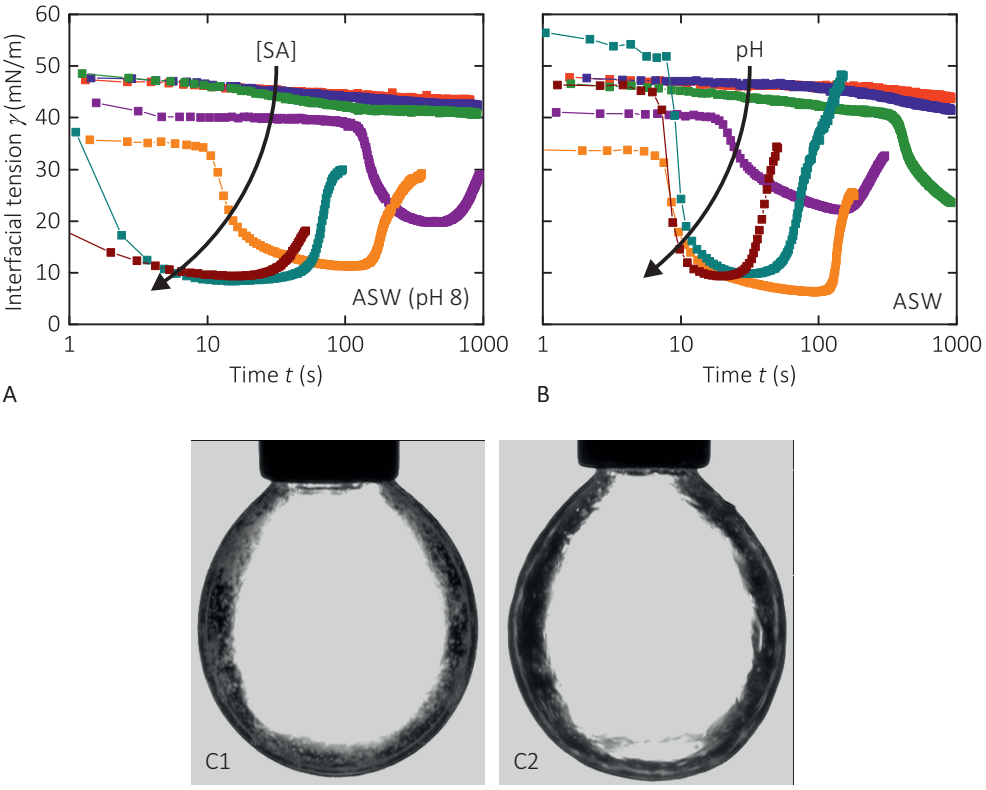

Figure 2 Interfacial tension versus time for (A) a drop of artificial seawater (pH 8) in ambient decane with various concentrations of stearic acid: 1 µM (red), 3 µM (blue), 10 µM (green), 30 µM (purple), 100 µM (orange), 300 µM (cyan), and 1000 µM (brown); and (B) a drop of artificial seawater in ambient decane with 100 µM stearic acid, at various pH values of the aqueous phase: pH 4 (red), pH 5 (blue), pH 6 (green), pH 7 (purple), pH 8 (orange), pH 9 (cyan), and pH 10 (brown). We remark that $Mg(OH)_2$ precipitation cannot be excluded at pH = 10. (C) Layer formation after creation of an interface between artificial seawater (pH 8) and decane with 1 mM stearic acid, (C1) after 15 min and (C2) after 40 min (note the somewhat crumpled structure of the drop surface).

(adjusted) pH values are formed in ambient decane with 100 µM stearic acid (Figure 2B). The characteristic response is observed starting at a pH of 6. The effect of increasing the pH of ASW (Figure 2B) is remarkably similar to that of increasing [StA] at elevated pH (Figure 2A). From this observation we can conclude that the deprotonation of the stearic acid is a crucial step in interfacial layer formation.

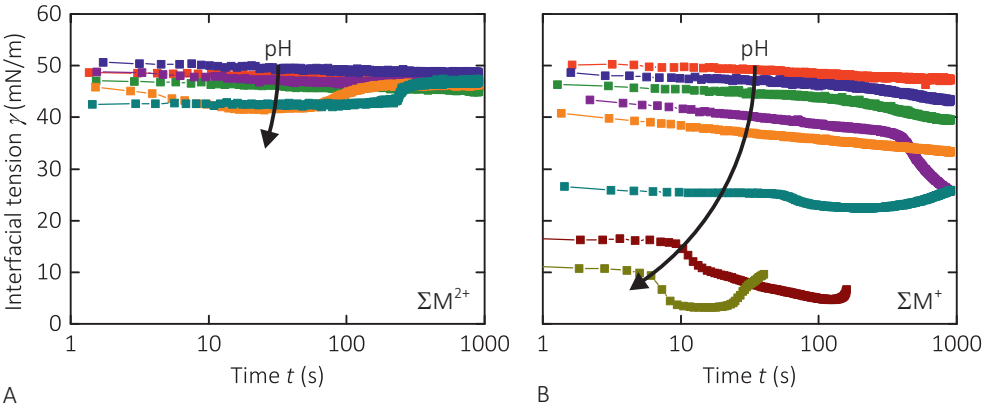

Figure 3 Interfacial tension versus time for aqueous drops in contact with a 100 µM stearic acid solution in decane. The aqueous phase consists of exclusively (A) the divalent cations and (B) the monovalent cations of ASW. In both graphs the pH of ASW is varied: pH 4 (red), pH 5 (blue), pH 6 (green), pH 7 (purple), pH 8 (orange), pH 9 (cyan), pH 10 (brown), and pH 11 (olive).

3.3.3 Effect of cation valency and salt concentration

Since artificial seawater contains a variety of cations, each of which could in principle form a chemical complex with stearate anions, it is still not clear how the observed layers are formed. To examine the possibility that either mono- or divalent cations are responsible, we prepare two solutions: one with all the monovalent cations of ASW and another with all the divalent ions. The concentrations of the individual cations are identical to those in Table 1. To explore also the pH dependence, relatively small amounts of KOH or HCl ($<$ 2% in total molarity) are added (as explained in Section 3.2). After bringing these solutions into contact with an oil phase consisting of 100 µM stearic acid in decane, the time-dependent IFT is measured as before. The results are shown in Figure 3.

Remarkably, in case of the divalent cations (ΣM^{2+}, Figure 3A), the changes in IFT are only minor. The IFT shows only a small instantaneous decrease, which grows only slightly as the pH is increased from 4 to 9. For pH $<$ 8, the IFT remains essentially constant. For pH $=$ 8 and 9 the initial decrease is followed up by a small increase. For pH $=$ 10 the typical IFT response with stages 15 is observed (result not shown), but for these conditions, the system is above the solubility limit of $Mg(OH)_2$.

For the monovalent cations (ΣM^{+}, Figure 3B), the IFT signature looks rather different. The instantaneous IFT decrease is again pH dependent, as for ΣM^{2+}, but the magnitude of the

effect is much larger. For pH $\geq$ 7 the stages 1-3 of Figure 1 can be recognized. Apparently, the monovalent cations of ASW are needed to induce interfacial layer formation; changing the IFT in the typical way as sketched in Figure 1. However, the changes in IFT occurring in stage 3 are clearly less pronounced as those for ASW. This suggests that the thermodynamic driving force for further structural transitions (after the initial adsorption) is relatively small for the ΣM^{+} ions. Thus, in ASW the ΣM^{2+} ions are expected to be involved in the subsequent stages (see Section 3.4).

Another noteworthy observation for the monovalent cations is that layer formation is visually observed (within the time span of the experiment) only at pH $\geq$ 10. Apparently, the kink in the IFT curve that marks the beginning of stage 3, is correlated to multilayer formation. This is not unexpected, since the transition from a 2D to a 3D layer is generally a discontinuous one. What is however surprising, is that the bulk pH at which it happens is much higher than for ASW. This points at a synergistic effect of ΣM^{2+} and ΣM^{+} ions in ASW (see Section 3.4).

In an attempt to further disentangle the cation contributions, additional experiments are conducted, now using aqueous subphases that contain (almost) exclusively Ca^{2+}, Mg^{2+}, or Na^{+} as the cation species. The concentration of their chloride salts was chosen to be 100 mM, to allow direct comparison between the three cations. Moreover, this concentration is also much larger than the $[K^{+}]$ ($<$ 1mM) originating from the KOH that was used to adjust the pH, which was also varied.

The pendant drop results in Figures 4A, B show essentially a lack of IFT response for the subphases of both $CaCl_2$ and $MgCl_2$ up to pH $=$ 8. This seems consistent with the findings in Figure 3A. For pH $\geq$ 9 we do not consider solutions at $[Mg^{2+}] = 0.1$ M due to the possibility of $Mg(OH)_2$ precipitation at the O/W interface. For the Ca^{2+} solutions, the pH can be increased much further without this problem. For pH $\geq$ 10 the characteristic IFT response is observed for the Ca^{2+} ions (albeit stage 4 is missing). It clearly indicates that in absence of all the other (cat)ions of ASW the aqueous phase pH has to be much higher, in order to obtain interfacial layers. Again this points to a synergistic effect of the ΣM^{2+} and ΣM^{+} ions in ASW.

The response in case of a subphase of NaCl (Figure 4C) only weakly resembles the response for the fraction with monovalent cations (Figure 3B). Considering the strong dominance of Na^{+} in the ΣM^{+} mixture, one might expect much more similar behaviors in Figures 3B and 4C. However, this appears not to be the case. For the 0.1 M NaCl solution,

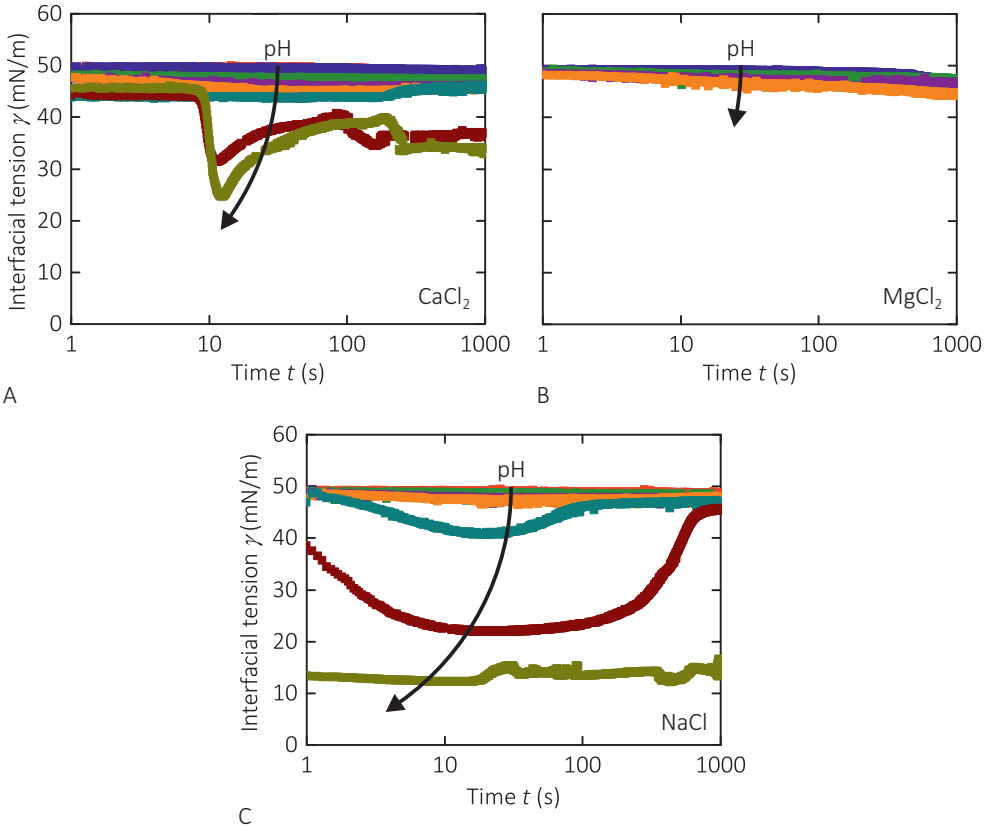

Figure 4 Interfacial tension versus time for aqueous drops with 100 mM (A) $CaCl_2$, (B) $MgCl_2$, and (C) NaCl, in ambient decane with 100 µM stearic acid, at various pH values of the aqueous phase: pH 4 (red), pH 5 (blue), pH 6 (green), pH 7 (purple), pH 8 (orange), pH 9 (cyan), pH 10 (brown), and pH 11 (olive).

the pH dependence of the IFT(time) function is weaker than for the ΣM^+ mixture at ~0.5 M. Besides that, also the detailed shapes of the IFT-time graphs are different. This is in spite of the fact that the [StA] is the same, *i.e.*, 100 µM. Comparing the IFT signatures for the subphase NaCl to those of $CaCl_2$ suggests that the mechanisms of initial layer formation are different for Na^+ or Ca^{2+} ions.

Finally, experiments are also performed for aqueous drops with various concentrations of $CaCl_2$ and NaCl at pH 10, in ambient decane with 1 mM stearic acid (Figure 5). At this high [StA], the duration of the IFT plateau (stage 2 in Figure 1) is reduced to O(1 s); this confirms that the accumulation of stearate species at the interface (as needed for the subsequent structural transition) proceeds more quickly for higher [StA] in the oil. For the

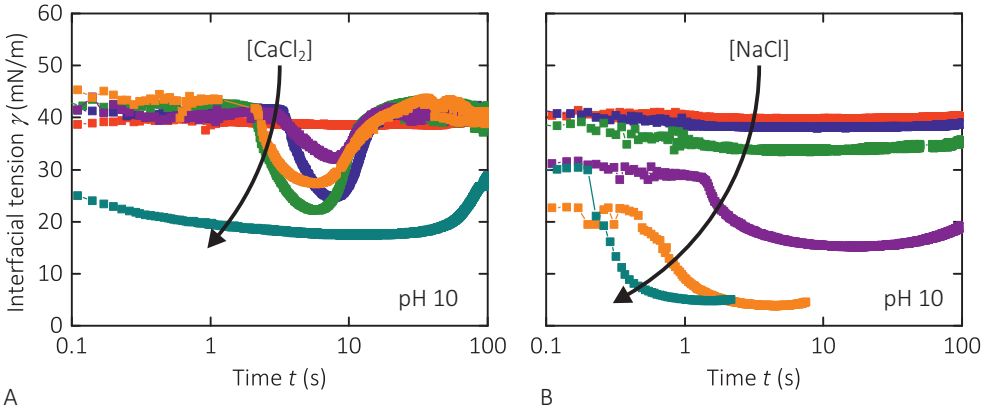

Figure 5 Interfacial tension versus time for aqueous drops at pH 10 in contact with ambient decane containing 1 mMstearic acid. The aqueous phase contains (A) $CaCl_2$ and (B) NaCl. Concentrations of these salts are 0.01 mM (red), 0.1 mM (blue), 1 mM (green), 10 mM (purple), 100 mM (orange), and 1000 mM (cyan). Note that the zero of the time axis is defined as the point where the drop just has been formed. The injection itself takes typically 1 s.

subphases containing $CaCl_2$, two remarkable observations are made: both the immediate IFT decrease and the lag time remain more or less constant, as the Ca^{2+}concentration is varied from 0.1 to 100 mM. Apparently, the [Ca^{2+}] does not play a key role in the kinetics of initial layer formation – at least not in this concentration range and pH. At the highest [Ca^{2+}] of 1 M, the IFT signature has changed, suggesting a different mechanism of layer formation.

At all [Ca^{2+}] $>$ 10 µM, solid layer formation is visually observed: above 100 mM within 1000 s and longer for lower [Ca^{2+}]. This indicates that the growth rate of the layer does depend on [Ca^{2+}] (in contrast to the formation rate of the initial layer). For the subphases of NaCl, the response is much more dependent on the salt concentration. At the highest [Na^{+}] ($>$ 100 mM), the IFT even becomes so low that it passes the minimum value that is needed to counteract the gravity force on the drop (*i.e.*, keep the drop attached).

3.3.4 Interfacial dilatational rheology

For a drop of artificial seawater dispersed in decane with a stearic acid concentration as high as 1 mM, the accumulation of material on the water-decane interface can be visually observed (as in Figure 2C) within several seconds after creation of the interface. Distinguishable individual patches nucleate and grow until the interface is fully covered. At longer time scales, the layer collapses and starts to buckle. Since the time scales of these

processes are shorter than the 10 s time resolution of the oscillating drop technique, we adjust the concentration of stearic acid in decane to 10 µM. As aqueous phases we explore artificial seawater and 1 M aqueous solutions of $CaCl_2$ or NaCl at pH 9 or 10.

Figure 6A shows the IFT and the dilatational storage modulus E' versus time for an aqueous drop of 1 M $CaCl_2$ at pH 10 (in ambient decane with 10 µM StA). The onset of the viscoelastic behavior coincides with the sharp decrease in interfacial tension, and when the IFT is at its minimum, a maximum E' of about 300 mN/m is reached. Subsequently, the (apparent) interfacial tension increases again, while the elasticity decreases. E' continues to decrease over time, reaching a value of about 30 mN/m after 4 h (not shown). Visibility of the layer is reached only after several hours at this low [StA]. The maximum magnitude of E' (well above the IFT of bare water-decane) indicates that the dilatational elasticity has to originate (mainly) from the stretching of a (solid-like) elastic surface layer.

We remark here that drops covered by such an elastic shell provide a case that is fundamentally different from that of classic adsorption layers and which gives rise to deviations from the Laplacian drop shape. For a modulus of 100 mN/m and IFT of 50 mN/m (roughly comparable to our case), these deviations have been predicted to be still small [11, 52]. However, this also implies that very accurate shape measurements are needed for simultaneously extracting the values of γ and E' in this regime. Therefore, although the shape deviations are small in our measurements, the obtained values of γ and E' should no longer be taken as truly quantitative measures, in cases that solid layers are present.

An additional observation at pH of 10 is that the total harmonic distortion (the power of all higher harmonics divided by the power at the fundamental frequency) in the interfacial area oscillation occasionally shows a steep increase shortly after the start of the increase in E'. This loss of linearity in the mechanical response indicates that even for small imposed deformations ($\mathrm{d}A/A < 0.05$), the surface layer cannot maintain its structural integrity, as a solid. Figure 6B shows the dilatational storage modulus for aqueous drops of artificial seawater and 1 M $CaCl_2$ and NaCl at pH 9 (in ambient decane with 10 µM stearic acid). The Ca^{2+} cations and ASW show similar results, while in case of NaCl only a slight increase in elasticity is observed. The maximum storage modulus of about 12 mN/m is reached quickly after the creation of the water-decane interface and remains fairly constant afterward. The loss modulus (not shown) shows considerable variation among experiments but is generally much smaller than the storage modulus, with a maximum value of about 50 mN/m for the divalent cations and about 10 mN/m for the monovalent

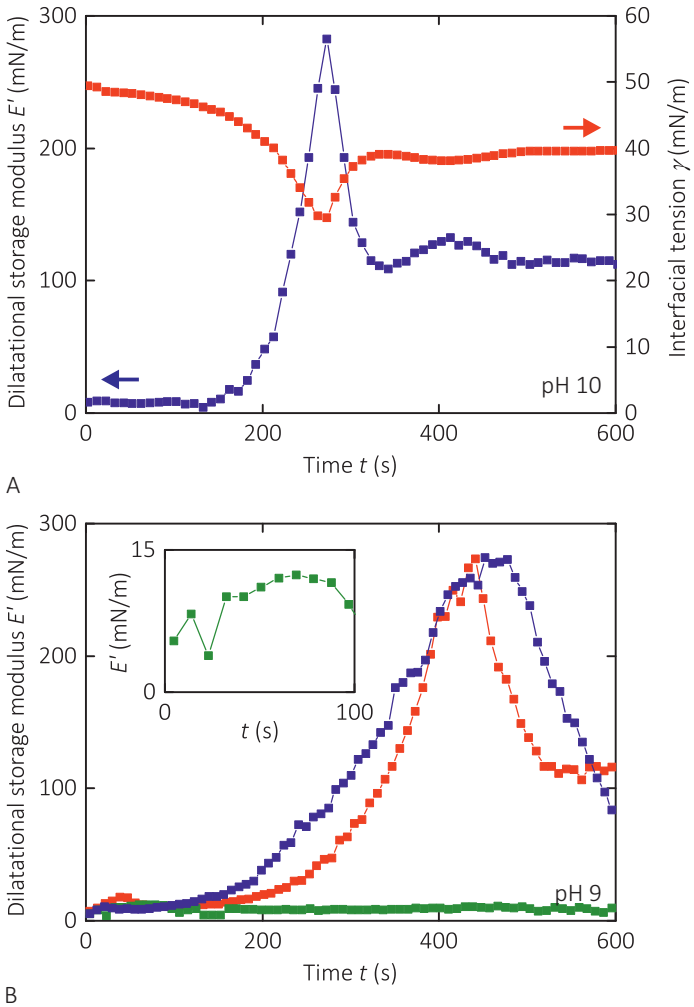

Figure 6 (A) Dilatational storage modulus E' (blue) and interfacial tension γ (red) versus time for an aqueous drop of 1M $CaCl_2$ (pH 10) in ambient decane with 10 µM stearic acid. (B) E' versus time for aqueous drops (pH 9) of artificial seawater (red), 1 M $CaCl_2$ (blue), and 1 M NaCl (green) in ambient decane with 10 µM stearic acid. The inset shows the result for NaCl in close-up.

cation. The layers formed at pH = 9 did not show the brittleness that is sometimes encountered at pH = 10.

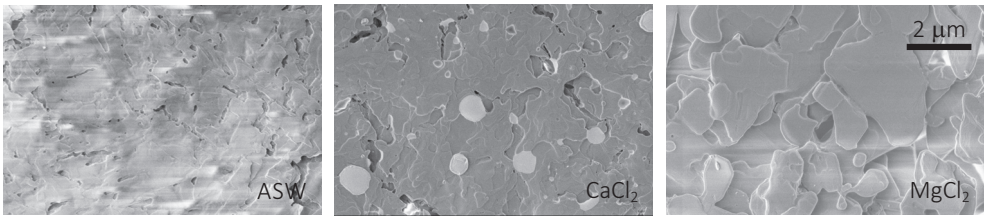

A B C

Figure 7 SEM images of the surface of layers grown at the interface between (A) ASW, or 0.5 M (B) $CaCl_2$ or (C) $MgCl_2$ solution (pH 9), and decane with 2 mM stearic acid.

3.3.5 SEM imaging

In Figure 7, SEM pictures of the surfaces of layers made from subphases of ASW, 0.5 M $CaCl_2$ (pH 9), and 0.5 M $MgCl_2$ (pH9) in contact with a 2 mM solution of StA in decane are shown. Large plateaus of several hundreds of nanometers in height can be seen on all surfaces. The morphology of the layers made using ASW is very different from the layers made using solutions of either $CaCl_2$ or $MgCl_2$. Besides that, it is noted that the plateaus formed in the presence of Mg^{2+} are higher than for Ca^{2+}.

3.3.6. XPS and IR experiments

XPS spectra give information about the elemental composition of the interfacial layer formed after prolonged contact (*i.e.*, in stage 6) between the aqueous and oil phases. The layers obtained from subphases containing either 0.5 M $CaCl_2$ or 0.5 M $MgCl_2$ (at pH 9) are used as references. The found elemental compositions (see Table 2) confirm the absence of other cations, while the levels of chloride indicate to which extent this anion could not be washed out (whereas metal stearates are not soluble, $CaCl_2$ is). Whereas for the sample from ASW the chloride content is insignificant, it is remarkably high for the subphase of $CaCl_2$. This is most likely due to precipitation of $CaCl_2$ during the drying step. Alternatively, also some CaCl-(St) complexes might be present [53]. In the sample from the $MgCl_2$ subphase, also some $Mg(OH)_2$ might be present.

Importantly, the layer formed from the subphase of artificial seawater (at pH 8) shows an elemental composition which is rather different from that of the aqueous subphase. Although magnesium is 5 times more abundant in artificial seawater than calcium, the amount of calcium that ends up in the interfacial layer exceeds the amount of magnesium by a factor of 20. Clearly, ultimately it is principally the calcium that is selectively incorporated.

Table 2 Relative amounts of different elements present in the layers grown at the interface between an aqueous phase and decane with 2 mM stearic acid as determined by XPS.[a]

element	ASW (pH 8)	0.5 M $CaCl_2$ (pH 9)	0.5 M $MgCl_2$ (pH 9)
C	48 ± 2	35 ± 3	46 ± 6
O	4.2 ± 0.2	3.2 ± 0.4	4.9 ± 0.7
Ca	1	1	–
Mg	0.05 ± 0.07	–	1
Cl	0.02 ± 0.02	0.7 ± 0.2	0.16 ± 0.07

[a] Normalizations are made relative to the Ca for ASW and $CaCl_2$ and to Mg for $MgCl_2$. No sodium was detected.

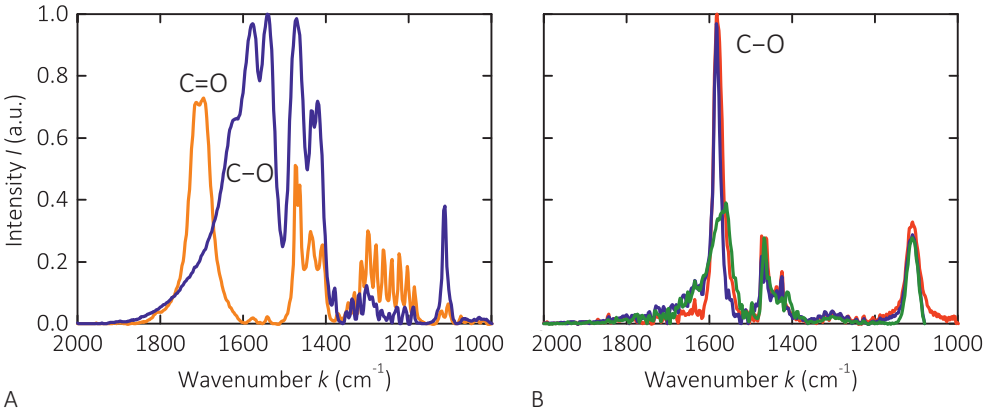

Figure 8 Part of the infrared spectra for (A) pure stearic acid (orange) and calcium stearate (blue), and (B) the layers grown at the interface between ASW (red), or 0.5 M $CaCl_2$ (blue) or $MgCl_2$ (green) solution (pH 9), and decane with 2 mM stearic acid.

Analysis of the same layers with IR spectroscopy serves to identify the chemical groups, in particular the ones involving the carboxyl unit. In the IR spectrum for pure stearic acid, the C=O stretching vibration of the carboxylic acid group is identified around 1710 cm^{-1} [54, 55] (see also Figure 8A). This absorption peak is absent in all our layer samples (see Figure 8B), which clearly indicates that none of the layer samples contains significant amounts of (protonated) stearic acid. This result matches the expectation, since at the high pH where the layers are formed, nearly all acid groups should be ionized.

Ionized states of the carboxylate group can be identified from the C—O antisymmetric stretching vibration. For pure calcium stearate, the main peak is identified around 1580

cm^{-1}, while also a second peak is visible around 1540 cm^{-1}. This double peak has been assigned to a hydrated species and to the coexistence of carboxylate groups that interact with calcium ions in two different modes, namely unidentate (1580 cm^{-1}) and bidentate (1540 cm^{-1}) [54-56]. In the spectrum of the layers prepared on a subphase of $CaCl_2$ or $MgCl_2$ (see Figure 8B) only the C—O antisymmetric stretching vibration around 1580 cm^{-1} is present. It turns out that the width of this peak depends on the metal ion that is associated with the carboxylate group: for layers created from the $MgCl_2$ subphase this peak is broadened (between 1560 and 1580 cm^{-1}) whereas with $CaCl_2$ it is not. Consequently, one can distinguish between calcium distearate and magnesium distearate. In the spectrum of the layer formed on a subphase of artificial seawater, the carboxylate peak is highly similar to the one present in the spectrum of the layer prepared on a subphase of $CaCl_2$. This corroborates our earlier XPS findings that the Ca^{2+} is selectively incorporated in the layer.

3.4 Discussion and interpretation

In our discussion of the formation of the interfacial layers of metal stearates, we refer to the first three stages that were distinguished in the typical response of the interfacial tension. Here we will focus on the most prominent trends in the data. We think that this is appropriate, considering the complexity of the layer formation in multicomponent mixtures, and the inherent limitations in insight that can be obtained, even from our combination of different techniques. On the basis of our observations (and literature) we speculate that the following general scenario could take place.

(i) Directly after the contact between the aqueous and oil phases, adsorption equilibria are set. The surface density of metal-stearate complexes is set by a dynamic exchange of cations and stearates between the interface and the bulk (aqueous respectively oil) phases. This is governed by equilibrium constants. In cases where multiple species can adsorb, the interfacial composition will be enriched by the species that have the strongest interfacial activity (*i.e.*, thermodynamic driving force for adsorption). Stearate anions have a stronger interfacial activity than undissociated StA, and M^+ ions have a stronger interfacial activity than M^{2+} ions. The total surface density is low enough to allow new complexes to be formed at the interface.

These hypotheses are supported by the following observations. The IFT changes ‘instantaneously’ (no transients could be observed) from the equilibrium value for bare water-decane to a lower value, after which it remains constant for some time. If diffusive

transport of species from either side of the interface would be rate-limiting, then the IFT should show a steady decrease starting from about 50 mN/m. For the ASW subphase, the immediate decrease of the IFT grows with increasing [StA]. This adaptability of the IFT indicates that there is still room for more stearate species in the interfacial layer. The stronger IFT decrease for ΣM^{+} as compared to ΣM^{2+} indicates that the former group creates species that are more interfacially active (in line with Refs. [1, 17]).

(ii) After the lag time plateau, nucleation and growth of a new phase occur. This is initiated at the interface, but the growth continues to take place in the third dimension (perpendicular to the interface). Here the subsequent layers will have an architecture that differs from the first one and possibly also have a different chemical composition. Multilayers built up from divalent cations and stearate anions develop a high dilatational storage modulus because of a dense and ordered structure, which can store mechanical energy if deformed. Since this elastic behavior originates from short-ranged interactions, the layer behaves like a brittle solid shell. The subsequent decline of E' is due to the formation of cracks in the layer, which cannot heal anymore. These cracks also facilitate the further growth of the layer in the third dimension.

Nucleation and growth are suggested by the existence of a lag time, and the shorter duration hereof as the [StA] or the pH is increased. This behavior bears similarity to the precipitation of solids from bulk liquids. Here the new phase is more stable, but its formation involves an activation energy barrier, which gets lower as the monomer density ('supersaturation') increases. Differences in architecture between the first and subsequent layers are known to contribute to the energy barrier [24, 53]. The formation of a solid phase of high chemical purity is suggested by our observations with XPS and IR. The solid-like behavior and brittleness are indicated by the large E' values and the low critical strain.

(iii) Growth of the layer continues as long as both cations and StA remain available in the bulk phases. New metal stearates are then continually formed at the O/W interface. Formed calcium stearates reside in the oil phase in the form of stacked bilayers, with the aliphatic chains pointing outward in each bilayer.

This hypothesis is supported by the known tendency of calcium stearates to assume conformations in which the calcium ion is sandwiched between two stearates [24]. The main steps of the proposed mechanism of 3D layer formation and growth are illustrated in Figure 9.

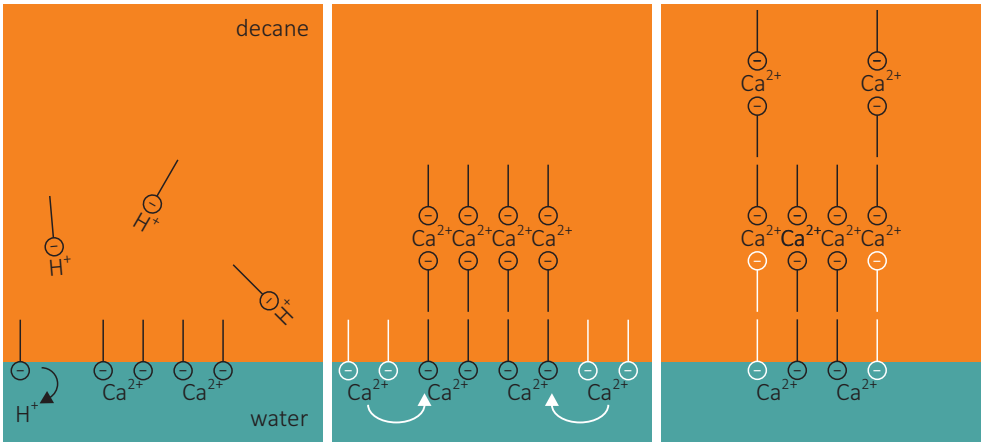

Figure 9 Proposed mechanism for multilayer formation. (A) Stearic acid molecules diffuse to the decane-water interface, deprotonate, and form metal-biacid complexes. (B) After nucleation of multilayer islands, new stearic acid molecules absorb onto the interface and (C) are subsequently incorporated in the interfacial layer. We note that this illustration is simplified. Chain orientations are taken equal in the first and subsequent layers, and the participation of monovalent ions in the initial stages is left out.

3.4.1. Remarks on artificial seawater

While this proposed sequence of events could apply to several of the considered aqueous salt solutions (at sufficiently high pH) in contact with stearic acid solutions in decane, the observations with ASW as the aqueous subphase remain most intriguing. A remarkable synergy between the ΣM^{+} and ΣM^{2+} ions appears to play a role. We speculate that in ASW the elemental composition of the interfacial layer changes in the course of time. The stronger interfacial activity of the stearates formed from monovalent cations, and especially the strong abundance of Na^{+} in ASW, makes it likely that the initially adsorbed molecules are predominantly sodium stearates. Stearates of divalent cations are less interfacially active when occurring in the form of charged monostearate complexes. However, calcium distearates are thermodynamically more stable than any of the other stearates, at least as a bulk phase. The circumstance that as individually adsorbed species the sodium stearates are more stable, but as a collective bulk phase the calcium stearates are, implies that strong changes in cation composition must take place during the development of the layer. Different mechanisms would be possible, *e.g.*, 'heterogeneous nucleation' of $CaSt_2$ on top of a NaSt monolayer or replacement of Na by Ca in the first

layer, followed by 'homogeneous nucleation'. In both scenarios, the synergy could have a strong effect on the kinetics of layer formation, as observed in the present study.

3.4.2. Remarks on the influence of pH

One aspect that remains to be understood is why the bulk pH required to obtain solid layers in ASW is so much lower than the required bulk pH in solutions of individual salts. This observation should be seen in the light of possible differences between the pH in bulk aqueous phase and the pH at/ near the interface. Such differences are known to occur if the interface is charged. In this case, electrostatic attraction and repulsion will modulate the local distributions of the ions in the solution, including the protons. The ionic strength of the subphase and specific ion effects influence the proton distribution and hence the local pH [57-59]. The sign and magnitude of the interfacial charge are set by the absorbed species, which can be negative (stearate anions), neutral (stearates of monovalent cations or distearates of divalent cations), or positive (monostearates of divalent cations). Knowledge of which of these species adsorb at which stage of the layer formation would be needed to further understand the dependence on subphase pH. This cannot be assessed with the methods we used and hence explanation of this issue has to fall beyond the scope of this chapter.

3.5 Conclusions and outlook

The formation of metal stearate layers at oil-water interfaces proceeds *via* distinct stages. Deprotonation of stearic acid is always required to initiate the multistep process. Immediate adsorption of surface active species is followed by molecular rearrangements that lead to the nucleation of a surface phase. Subsequently, layers are formed that continue to grow as multilayers inside the oil phase. The details of these scenarios are strongly dependent on the pH and cationic composition of the aqueous subphase. Stearates of monovalent cations appear to have stronger interfacial activity, but solid phases formed from them are thermodynamically less stable as compared to stearates of divalent cations, in particular Ca^{2+}. As a consequence, although the stages leading to the final layers appear to be common, the underlying mechanisms are different for monovalent cations, divalent cations, and their mixtures. This is best illustrated in artificial seawater, in which layer formation is strongly facilitated by synergistic effects of the mono- and divalent cations.

We also like to mention some remaining and new questions. First, it remains to be fully understood why the required pH for the formation of thick layers is so much higher for either mono- or divalent cations, than for ASW. This is most probably related to differences in the accumulated charge density at the interface and to the ion distributions in the associated Stern and diffuse layers. Characterization with, *e.g.*, infrared reflection adsorption spectroscopy could perhaps shed more light on this issue. Second, the details of the nucleation and growth of the layers remain obscure. Visualization by imaging ellipsometry at the oil-water interface might allow monitoring this process. And third, the response of the (developing) stearate layer to compositional changes in the fluids could be studied to gain more insight into the formation and mechanical properties of the layers. For this, microfluidics could be used.

References

[1] O. Brandal, J. Sjoblom and G. Oye, *Interfacial behavior of naphthenic acids and multivalent cations in systems with oil and water. I. A pendant drop study of interactions between n-dodecyl benzoic acid and divalent cations*, J. Disper. Sci. Technol. 25 (2004), 367-374.

[2] T.E. Havre, M.H. Ese, J. Sjoblom and A.M. Blokhus, *Langmuir films of naphthenic acids at different pH and electrolyte concentrations*, Colloid Polym. Sci. 280 (2002), 647-652.

[3] B.P. Binks, H. Kellay and J. Meunier, *Bending elastic-modulus of monolayers at oil-water interfaces*, Thin Solid Films 210 (1992), 118-120.

[4] A. Bonfillon and D. Langevin, *Viscoelasticity of monolayers at oil-water interfaces*, Langmuir 9 (1993), 2172-2177.

[5] E. Dickinson, *Adsorbed protein layers at fluid interfaces: interactions, structure and surface rheology*, Colloids Surf. B 15 (1999), 161-176.

[6] N. Aske, R. Orr and J. Sjoblom, *Dilatational elasticity moduli of water-crude oil interfaces using the oscillating pendant drop*, J. Disper. Sci. Technol. 23 (2002), 809-825.

[7] M. Jeribi, B. Almir-Assad, D. Langevin, I. Henaut and J.F. Argillier, *Adsorption kinetics of asphaltenes at liquid interfaces*, J. Colloid Interface Sci. 256 (2002), 268-272.

[8] J.K. Ferri, C. Kotsmar and R. Miller, *From surfactant adsorption kinetics to asymmetric nanomembrane mechanics: Pendant drop experiments with subphase exchange*, Adv. Colloid Interface Sci. 161 (2010), 29-47.

[9] J.B. Li, Y. Zhang and L.L. Yan, *Multilayer formation on a curved drop surface*, Angew. Chem. Int. Ed. 40 (2001), 891-894.

[10] G. Lu, H. Chen and J.B. Li, *Forming process of folded drop surface covered by human serum albumin, beta-lactoglobulin and beta-casein, respectively, at the chloroform/water interface*, Colloids Surf. A 215 (2003), 25-32.

[11] J.K. Ferri, W.F. Dong, R. Miller and H. Mohwald, *Elastic moduli of asymmetric ultrathin free-standing polyelectrolyte nanocomposites*, Macromolecules 39 (2006), 1532-1537.

[12] R.L. Martin and J.C. Winters, *Composition of crude oil through seven carbons as determined by gas chromoatogrpahy*, Anal. Chem. 31 (1959), 1954-1960.

[13] D.W. Westlake, A. Jobson, Phillipp.R and F.D. Cook, *Biodegradability and crude-oil composition*, Can. J. Microbiol. 20 (1974), 915-928.

[14] W. Meredith, S.J. Kelland and D.M. Jones, *Influence of biodegradation on crude oil acidity and carboxylic acid composition*, Org. Geochem. 31 (2000), 1059-1073.

[15] A. Lager, K.J. Webb and I.R. Collins, *LoSal™ enhanced oil recovery: Evidence of enhanced oil recovery at the reservoir scale*, SPE/DOE Symposium on Improved Oil Recovery, Tulsa (2008).

[16] J. Seccombe, A. Lager, G. Jerauld, B. Jhaveri, T. Buikema, S. Bassler, J. Denis, K.J. Webb, A. Cockin and E. Fueg, *Demonstration of low-salinity EOR at interwell scale, Endicott Field, Alaska*, SPE Improved Oil Recovery Symposium, Tulsa (2010).

[17] O. Brandal and J. Sjoblom, *Interfacial behavior of naphthenic acids and multivalent cations in systems with oil and water. II: Formation and stability of metal naphthenate films at oil-water interfaces*, J. Disper. Sci. Technol. 26 (2005), 53-58.

[18] A. Bonfillon, F. Sicoli and D. Langevin, *Dynamic surface-tension of ionic surfactant solutions*, J. Colloid Interf. Sci. 168 (1994), 497-504.

[19] K.D. Danov, P.M. Vlahovska, P.A. Kralchevsky, G. Broze and A. Mehreteab, *Adsorption kinetics of ionic surfactants with detailed account for the electrostatic interactions: effect of the added electrolyte*, Colloids Surf. A 156 (1999), 389-411.

[20] I.B. Ivanov, K.G. Marinova, K.D. Danov, D. Dirnitrova, K.P. Ananthapadmanabhan and A. Lips, *Role of the counterions on the adsorption of ionic surfactants*, Adv. Colloid Interface Sci. 134-35 (2007), 105-124.

[21] Y.J. Zhang and P.S. Cremer, *Interactions between macromolecules and ions: the Hofmeister series*, Curr. Opin. Chem. Biol. 10 (2006), 658-663.

[22] D.R. Kester, I.W. Duedall, D.N. Connors and R.M. Pytkowic, *Preparation of artificial seawater*, Limnol. Oceanogr. 12 (1967), 176-179.

[23] A. Gericke and H. Huhnerfuss, *The effect of cations on the order of saturated fatty-acid monolayers at the air-water-interface as determined by infrared reflection-absorption spectrometry*, Thin Solid Films 245 (1994), 74-82.

[24] J.B. Peng, G.T. Barnes and I.R. Gentle, *The structures of Langmuir-Blodgett films of fatty acids and their salts*, Adv. Colloid Interface Sci. 91 (2001), 163-219.

[25] I. Langmuir and V.J. Schaefer, *Composition of fatty acid films on water containing calcium or barium salts*, J. Am. Chem. Soc. 58 (1936), 284-287.

[26] J.M. Bloch, W.B. Yun, X. Yang, M. Ramanathan, P.A. Montano and C. Capasso, *Adsorption of counterions to a stearate monolayer spread at the water-air interface - A synchrotron x-rax study*, Phys. Rev. Lett. 61 (1988), 2941-2944.

[27] M. Yazdanian, H. Yu and G. Zografi, *Ionic interactions of fatty-acid monolayers at the air-water-interface*, Langmuir 6 (1990), 1093-1098.

[28] J. Kmetko, A. Datta, G. Evmenenko and P. Dutta, *The effects of divalent ions on Langmuir monolayer and subphase structure: A grazing-incidence diffraction and Bragg rod study*, J. Phys. Chem. B 105 (2001), 10818-10825.

[29] V. Dupres, S. Cantin, F. Benhabib, F. Perrot, P. Fontaine, M. Goldmann, J. Daillant and O. Konovalov, *Superlattice formation in fatty acid monolayers on a divalent ion subphase: Role of chain length, temperature, and subphase concentration*, Langmuir 19 (2003), 10808-10815.

[30] J. Pignat, S. Cantin, R.C.W. Liu, M. Goldmann, P. Fontaine, J. Daillant and F. Perrot, *pH-dependent kinetics of MgCl2 adsorption under a fatty-acid Langmuir film*, Eur. Phys. J. E 20 (2006), 387-394.

[31] M. Yazdanian, H. Yu, G. Zografi and M.W. Kim, *Divalent-cation stearic acid monolayer interactions at the air-water interface*, Langmuir 8 (1992), 630-636.

[32] R.S. Ghaskadvi, S. Carr and M. Dennin, *Effect of subphase Ca++ ions on the viscoelastic properties of Langmuir monolayers*, J. Chem. Phys. 111 (1999), 3675-3678.

[33] M.C. Shih, T.M. Bohanon and J.M. Mikrut, *Pressure and pH-dependence of the structure of a fatty-acid monolayer with calcium-ions in the subphase*, J. Chem. Phys. 96 (1992), 1556-1559.

[34] V.M. Kaganer, H. Mohwald and P. Dutta, *Structure and phase transitions in Langmuir monolayers*, Rev. Mod. Phys. 71 (1999), 779-819.

[35] S. Cantin, S. Péralta, P. Fontaine, M. Goldmann and F. Perrot, *Evolution toward the X phase of fatty acid Langmuir monolayers on a divalent cation solution*, Langmuir 26 (2010), 830-837.

[36] R. Johann, D. Vollhardt and H. Mohwald, *Shifting of fatty acid monolayer phases due to ionization of the headgroups*, Langmuir 17 (2001), 4569-4580.

[37] R. Aveyard, B.P. Binks, N. Carr and A.W. Cross, *Stability of insoluble monolayers and ionization of Langmuir-Blodgett multilayers of octadecanoic acid*, Thin Solid Films 188 (1990), 361-373.

[38] R.D. Neuman and J.W. Swanson, *Multilayer deposition of stearic acid-calcium stearate mono-molecular films*, J. Colloid Interface Sci. 74 (1980), 244-259.

[39] M. Gönen, S. Öztürk, D. Balköse, S. Okur and S. Ülkü, *Preparation and characterization of calcium stearate powders and films prepared by precipitation and Langmuir-Blodgett techniques*, Ind. Eng. Chem. Res. 49 (2010), 1732-1736.

[40] R.D. Neuman, *Stearic acid and calcium stearate monolayer collapse*, J. Colloid Interface Sci. 56 (1976), 505-510.

[41] A. Angelova, D. Vollhardt and R. Ionov, *2D-3D transformations of amphiphilic monolayers influenced by intermolecular interactions: A Brewster angle microscopy study*, J. Phys. Chem. 100 (1996), 10710-10720.

[42] S. Kundu, S. Datta and S. Hazra, *Effect of metal ions on monolayer collapses*, Langmuir 21 (2005), 5894-5900.

[43] S. Kundu and D. Langevin, *Fatty acid monolayer dissociation and collapse: Effect of pH and cations*, Colloid Surf. A 325 (2008), 81-85.

[44] S. Seok, T.J. Kim, S.Y. Hwang, Y.D. Kim, D. Vaknin and D. Kim, *Imaging of collapsed fatty acid films at air-water interfaces*, Langmuir 25 (2009), 9262-9269.

[45] A. Goebel and K. Lunkenheimer, *Interfacial tension of the water/n-alkane interface*, Langmuir 13 (1997), 369-372.

[46] N.J. Alvarez, L.M. Walker and S.L. Anna, *A non-gradient based algorithm for the determination of surface tension from a pendant drop: Application to low Bond number drop shapes*, J. Colloid Interface Sci. 333 (2009), 557-562.

[47] A.G. Banpurkar, K.P. Nichols and F. Mugele, *Electrowetting-based microdrop tensiometer*, Langmuir 24 (2008), 10549-10551.

[48] R. Miller, J.K. Ferri, A. Javadi, J. Kragel, N. Mucic and R. Wustneck, *Rheology of interfacial layers*, Colloid Polym. Sci. 288 (2010), 937-950.

[49] M.E. Leser, S. Acquistapace, A. Cagna, A.V. Makievski and R. Miller, *Limits of oscillation frequencies in drop and bubble shape tensiometry*, Colloids Surf. A 261 (2005), 25-28.

[50] R. Myrvold and F.K. Hansen, *Surface elasticity and viscosity from oscillating bubbles measured by automatic axisymmetric drop shape analysis*, J. Colloid Interface Sci. 207 (1998), 97-105.

[51] F. Ravera, G. Loglio and V.I. Kovalchuk, *Interfacial dilational rheology by oscillating bubble/drop methods*, Curr. Opin. Colloid Interface Sci. 15 (2010), 217-228.

[52] J.K. Ferri and P.A.L. Fernandes, *Axisymmetric drop shape analysis with anisotropic interfacial stresses: Deviations from the Young-Laplace equation*, in Bubble and Drop Interfaces, edited by R. Miller and L. Liggieri, VSP (2011).

[53] S. Garoff, H.W. Deckman, J.H. Dunsmuir, M.S. Alvarez and J.M. Bloch, *Bond-orientational order in Langmuir-Blodgett surfactant monolayers*, Journal De Physique 47 (1986), 701-709.

[54] J. Bagg, M.D. Haber, H.P. Gregor, M.B. Abramson and M. Fichman, *Composition of stearic acid monolayers from calcium-containing substrates*, J. Am. Chem. Soc. 86 (1964), 2759-2763.

[55] D.W. Deamer, D.W. Meek and D.G. Cornwell, *Properties composition and structure of stearic acid-stearate monolayers on alkaline earth solutions*, J. Lipid Res. 8 (1967), 255-263.

[56] Y.Q. Lu and J.D. Miller, *Carboxyl stretching vibrations of spontaneously adsorbed and LB-transferred calcium carboxylates as determined by FTIR internal reflection spectroscopy*, J. Colloid Interface Sci. 256 (2002), 41-52.

[57] E. Le Calvez, D. Blaudez, T. Buffeteau and B. Desbat, *Effect of cations on the dissociation of arachidic acid monolayers on water studied by polarization-modulated infrared reflection-absorption spectroscopy*, Langmuir 17 (2001), 670-674.

[58] P.B. Miranda, Q. Du and Y.R. Shen, *Interaction of water with a fatty acid Langmuir film*, Chem. Phys. Lett. 286 (1998), 1-8.

[59] J.C.T. Eijkel and A. Van Den Berg, *Nanofluidics and the chemical potential applied to solvent and solute transport*, Chem. Soc. Rev. 39 (2010), 957-973.

Chapter 4

Use of electrowetting to measure dynamic interfacial tensions of a microdrop

The adsorption of surface active species to liquid-liquid and to solid-liquid interfaces can have dramatic effects in microfluidics. In this chapter we show how electrowetting on dielectric can be used to monitor a dynamic liquid-liquid interfacial tension (IFT) with a time resolution of $O(1\ \mathrm{s})$ using amplitude modulation of the AC voltage. This straightforward method, which requires less than a microliter of sample, is demonstrated for aqueous drops containing Triton X-100 surfactant on a Teflon AF-coated substrate and with heptane as the immiscible oil ambient. Under these conditions, next to extracting the oil-water IFT (γ_{ow}), also the effective water-substrate IFT difference ($\Delta\gamma_{ws}$) can be obtained from the oil-water IFT and the Young angle. Both γ_{ow} and γ_{ws} decrease over time due to adsorption. The measured dynamic oil-water IFT compares well to results of pendant drop experiments.

This chapter has been published as R. de Ruiter, P. Wennink, A.G. Banpurkar, M.H.G. Duits and F. Mugele, *Use of electrowetting to measure dynamic interfacial tensions of a microdrop*, Lab on a Chip 12 (2012), 2832-2836.

4.1 Introduction

Microfluidic systems are characterized by large surface-to-volume ratios. Interfacial tensions and their variation due to adsorption therefore play a key role for both the physical behavior of the systems and for the performance of devices. This is particularly true for the increasingly popular digital microfluidic systems, which make use of small drops serving simultaneously as closed containers to manipulate the sample of interest and as microscopic reactors [1-3]. Especially, the analysis of physiological fluids like blood, urine, and saliva [4], and of cultured pathogenic cells [5] increasingly find application. Frequently, such biochemical assays are based on reactions of the sample with ligands that are attached to the walls of the device [6-9]. Since most digital microfluidic systems make use of oil as an ambient medium (to prevent amongst others evaporation), good control and characterization of all interfaces including in particular the complex drop-(oil)-substrate interface is crucial. Several approaches have been implemented to measure IFTs in microfluidic systems [10-16].

Electrowetting (EW) is arguably the most versatile technique to achieve detailed control over individual drops including all relevant operations such as drop formation, positioning, merging, mixing, and splitting [17-20]. EW relies on the balance of electrostatic forces acting on a conductive liquid drop in a nonconductive ambient medium with capillary forces resulting from the various interfacial tensions in the system. Since the electrostatic forces are determined exclusively by the geometry of both the drop and the electrodes, variations of the response of the drop to the electric fields as a function of time can be attributed to temporal variations of the interfacial tensions.

Previously, our group and others demonstrated that the EW response can be used to determine the equilibrium values of oil-water interfacial tensions for a variety of complex systems ranging from aqueous solutions of surfactants to milk [21, 22]. It is shown that this method is especially suitable for small sample volumes, as opposed to conventional techniques, such as Wilhelmy plate, Du Noüy ring, and pendant drop tensiometry. More recently, this EW approach was adapted for measuring capacitance [23], and for determining elastic moduli and extensional viscosities [24, 25].

In the present chapter, we demonstrate a new method to monitor the temporal evolution of an oil-water interfacial tension due to the adsorption of surface active compounds by simply analyzing the time-dependent EW response of sessile drops. Under the conditions used, one simultaneously obtains information about the complex drop-(oil)-substrate

interface. The method is readily integrated into open digital microfluidic systems [26]. It offers a time resolution of a few seconds and is applicable for sample volumes down to approximately 20 nL. For the specific water-soluble surfactant under consideration here we find that the effective water-substrate interfacial tension varies in a very similar manner as the oil-water interfacial tension, which suggests the presence of a presumably molecularly thin oil film below the drop.

4.2 Materials and methods

A microscopic glass plate with a conductive indium tin oxide (ITO) layer is covered with a 3.5 µm thick layer of Teflon AF 1600 (DuPont), by twice dipcoating from a 3 wt% solution in FC-75 and heating in a vacuum oven. The thickness of the dielectric layer is determined in a calibration measurement with a water drop in ambient silicone oil (Fluka), where the interfacial tension γ_{ow} is known to be 38 mN/m. Solutions of the nonionic surfactant Triton X-100 (Fluka) at 0.0005 and 0.001 wt% are prepared in ultrapure water (Millipore Synergy UV instrument, resistivity 18.2 MΩ·cm). At those concentrations, which are well below the critical micelle concentration, the relaxation time of γ_{ow} due to adsorption is of O(10-100 s). KCl (Merck) was added to all aqueous phases to increase the conductivity to 3 mS/cm. Heptane (Fluka, $\gamma_{ow} = 48$ mN/m) was used as the ambient phase.

In the experiments, an aqueous drop of 10 µL is dispensed onto the substrate, while the system is submerged in the oil (Figure 1A). Since the dispensing needle also serves as the electrical connection, the measurements can start within a few seconds after introducing the drop. We apply an electric field *via* a high frequency (10 kHz) carrier wave to avoid charge accumulation and to minimize possible effects of contact angle hysteresis [27]. The carrier wave is modulated with a low-frequency step profile, allowing to probe 5 (rms) voltages within each ramp (Figure 1B). The total ramp time is varied between 2 to 25 s, while the discrete voltages U are distributed linearly between the square of the minimum (0) and maximum (50 V_{rms}). The time- and voltage-dependent contact angle θ (Figure 1C) is recorded (and measured off-line) using an OCA 20L contact angle measuring and contour analysis system (DataPhysics). Dynamic oil-water IFTs extracted from these experiments are compared to measurements using the pendant drop technique.

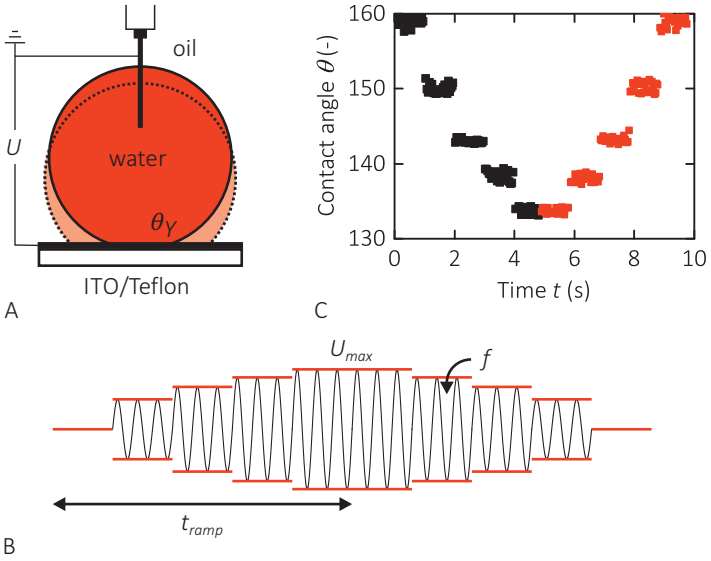

Figure 1 Schematic showing (A) the electrowetting setup, (B) the applied signal (U_{max} = 50 V_{rms}, f = 10 kHz, t_{ramp} = 2, 5, 25 s), and (C) the corresponding stepwise changes in contact angle.

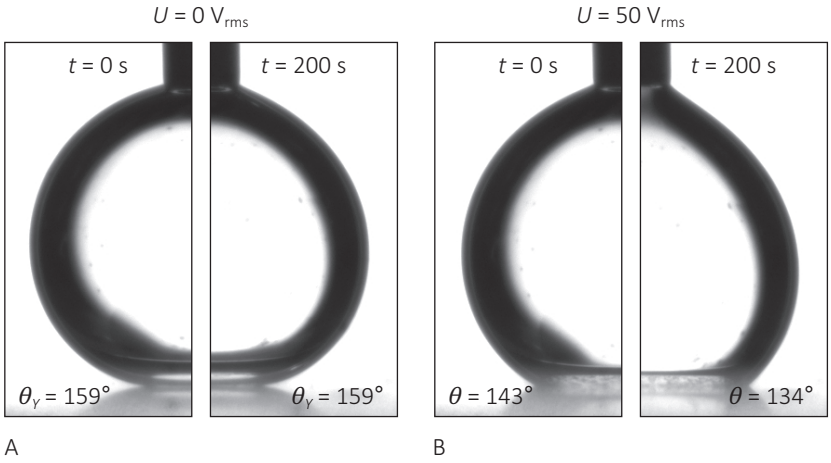

Figure 2 Pictures showing the difference in contact angle (A) without and (B) with applied electric field, for a freshly deposited (left) and aged (right) aqueous drop with 0.001 wt% Triton X-100 in ambient heptane.

4.3 Results and discussion

Figure 2 illustrates the basic observation underlying our method: the contact angle of a drop decreases with increasing voltage as expected for electrowetting. However, the

contact angle decrease is less pronounced for a freshly deposited drop ($t = 0$) than for an aged drop ($t = 200$ s). In contrast, the contact angle at zero voltage, *i.e.*, the Young angle (θ_Y), appears to remain constant.

To analyze this behavior in more detail, we deposit a drop onto the substrate ($t = 0$) and continuously ramp the voltage up and down (as in Figure 1B). As illustrated by Figure 3, $\cos\theta$ increases proportionally with U^2, as expected based on the general electrowetting equation [28]:

$\cos\theta(U) = \cos\theta_Y + (C/2\gamma_{ow})U^2$ (**Equation 1**),

where C represents the electric capacitance per unit area of the drop-substrate interface and is given by $C = \varepsilon_0\varepsilon_d/d$ with $\varepsilon_0\varepsilon_d$ the permittivity and d the thickness of the dielectric layer [29]. Over time, however, a gradual increase of the slope is observed; this can also be seen from the difference between subsequent ramps of increasing and decreasing voltage in Figure 3. After approximately 10 cycles (of 5 s each) the variation of the slope saturates and the EW curve does not change anymore. Within the same time span, the Young angle $\theta(U = 0)$ hardly changes, as shown in the inset.

We now consider the time-dependence of our measurements in more detail. In general, the force balance at the three-phase contact line for a mechanically equilibrated drop reads:

$\gamma_{ws}(t) + \gamma_{ow}(t)\cos\theta(U,t) = \gamma_{os}(t) + f_{el}(t)$ (**Equation 2**),

where $f_{el}(t) = CU(t)^2/2$ is the electrostatic force per unit length pulling on the contact line in the outward direction. In principle all interfacial tensions can vary over time, due to adsorption processes. The time dependence of the contact angle is the result of the slowly varying interfacial tensions $\gamma(t)$ in combination with the imposed $U(t)$ signal.

The data in Figure 3 clearly demonstrate that there is a separation of time scales in the present experiments. On the one hand the drop responds quickly to variations of the amplitude of the applied (rms) voltage, on the other hand the interfacial tensions in the system slowly vary due to the adsorption of surfactant. Under these conditions, we can separate the EW response from the surfactant adsorption. For suitably chosen ramp times, the slope of each EW curve is determined exclusively by the momentary value of the oil-water interfacial tension. The increase in the slope of the EW curves with sample age then reflects the decrease of γ_{ow} with increasing surfactant adsorption. From a

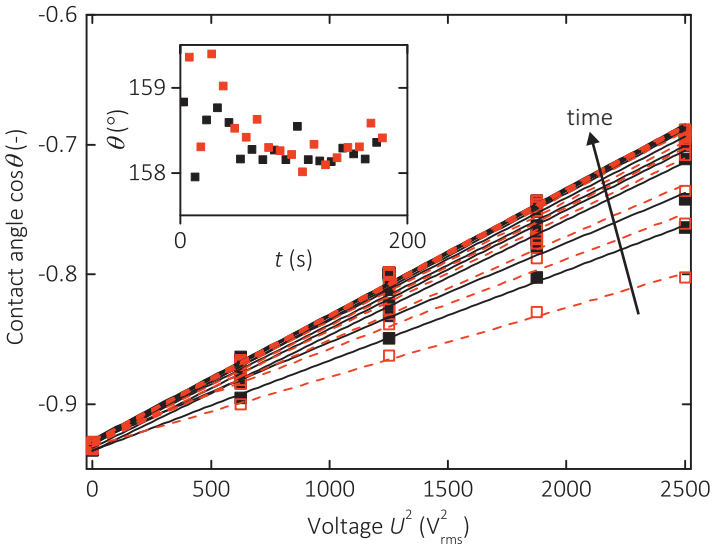

Figure 3 Electrowetting curves for an aqueous drop with 0.001 wt% Triton X-100 in ambient heptane ($t_{ramp} = 5$ s), as determined for increasing (black, solid) and decreasing (red, open and dashed) voltage. The inset shows the evolution of the contact angle at 0 V, as extracted from the linear fits.

practical perspective, this implies that the ramp time must be chosen faster than the characteristic time for variations of the interfacial tension. The latter is related to the diffusion and/ or adsorption time of the surfactant. If the ramp time is chosen too long we observe deviations from linearity in the $(\cos\theta\,, U^2)$ relation (similar to Raccurt *et al.* [21]). For a typical drop size of the order of 10 µL, the hydrodynamic response time of the drop (O(10-50 Hz)) provides a lower limit of O(1 s) to the ramp time.

In Figure 4A we make use of the separation of time scales to extract the oil-water interfacial tension as a function of time from the data in Figure 3. We find that γ_{ow} decreases gradually, in an almost exponential manner. The first measurement point ($t \approx 0$) gives an IFT of 46 mN/m, which corresponds well with that of a pure heptane-water interface. This corroborates that the time used for introducing the drop and starting the experiment was short compared to the timescale for Triton X-100 adsorption at the oil-water interface. After a 'decay time' of about 60 s, γ_{ow} remains constant within 1%, an uncertainty that is also found in experiments with clean interfaces. We therefore assume that equilibrium has been reached.

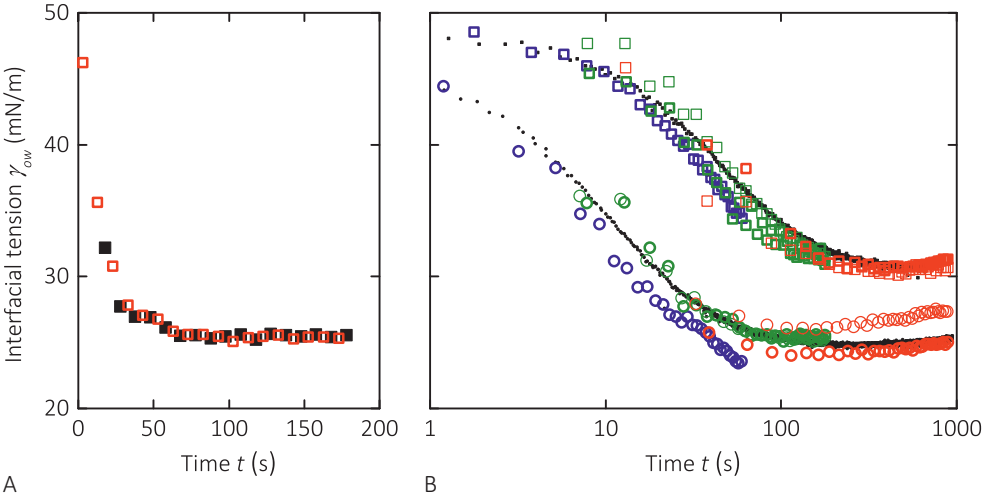

Figure 4 Oil-water interfacial tension versus time for aqueous drops with Triton X-100 in ambient heptane. (A) Example for 0.001 wt% Triton X-100 ($t_{ramp} = 5$ s), as determined for increasing (black, closed) and decreasing (red, open) voltages. (B) Validation of electrowetting based tensiometry for various ramp times (2 s (blue), 5 s (green), and 25 s (red)) against pendant drop tensiometry (black) for Triton X-100 concentrations of 0.0005 wt% (squares) and 0.001 wt% (circles). Thick and thin symbols indicate duplicate measurements.

To validate these electrowetting-based results, we compare the extracted IFTs to pendant drop tensiometry measurements for the same concentrations of Triton X-100, see Figure 4B. The shapes of the $\gamma_{ow}(t)$ curves agree well, and deviations between the two types of measurements are typically less than 5-10% (< 3 mN/m). We consider this a good correspondence, taking into account the standard errors of both techniques, and small differences between the samples (like the geometry of the drop and its surroundings, and flow patterns inside the drops). It illustrates for the first time that also EW can be used to measure oil-water interfacial tensions with a time resolution of $O(1\text{ s})$.

From an applied perspective a few additional remarks can be made. Firstly, we note that our time resolution is enabled by choosing the voltages within the linear regime given by Equation 1. This is normally achieved by keeping $\Delta\cos\theta < 0.7$ [28]. In this regime, sampling a straight line at 5 points offers an optimal trade-off between precision in IFT and resolution in time. After calibrating or calculating the capacitance C, the voltage range can be adjusted to the expected range of IFT values. Secondly, we note that EW-based tensiometry has distinct advantages when compared to pendant drop experiments. Unlike the latter method, EW does not require the Bond number to be above $O(0.1)$ [30]. Hence

much smaller drops can be used, which is very useful when only tiny amounts of sample are available. This applies in the wire-drop geometry of the present study, and even more so in configurations with interdigitated EW electrodes. Another advantage of the low Bond number regime is that also systems with a small density difference between the drop phase and the ambient medium can be studied.

An additional capability of the EW-based method is that besides the oil-water interface, also the water-substrate interface can be characterized indirectly. After determination of γ_{ow} and θ_Y (independently) from the slope and intersection of the EW curve, Equation 2 can be used to determine $\gamma_{ws} - \gamma_{os}$. In the inset of Figure 3 we showed that θ_Y is essentially constant throughout the present measurements. Since γ_{ow} decreases over time, $\gamma_{ws} - \gamma_{os}$ has to decrease as well (note that $\cos\theta_Y < 0$). The drop substrate interface may actually contain a thin film of a few layers of oil molecules separating the aqueous drop from the water repelling Teflon AF surface. Previous theoretical [31] and experimental [32] studies suggest the existence of such a layer in EW systems presumably due to a short-range repulsive component in the disjoining pressure. For the present system with a purely water soluble surfactant and assuming no direct contact between the drop and the substrate, it is reasonable to assume that γ_{os} remains constant (see also Ahmadi *et al.* [23]). Based on this assumption we can extract the change in γ_{ws} from the variation of γ_{ow} and θ_Y with time. The results in Figure 5 indeed indicate that γ_{ws} decreases in a very similar manner as γ_{ow}. In the present experiments, a few molecular layers of adsorbed oil might make the effective water-substrate interface 'look' similar to the oil-water interface for adsorbing Triton X-100 molecules. This rationalizes the similar trend for γ_{ws} and γ_{ow} in Figure 5.

Note that a constant θ_Y is not required to extract $\Delta\gamma_{ws}$. The present situation is merely a specific case caused by the similar response in γ_{ws} and γ_{ow}. From an applied perspective, this situation is very desirable since it indicates that there is no excessive adsorption directly onto the solid surface. In fact, we find a very similar response for drops of cell medium in ambient silicone oil. Variations in the Young angle over time are to be expected in experiments where the drop is in direct contact with the substrate, *e.g.*, when air is used as the ambient phase. However, in that case additional pinning forces at the contact line introduce a (time-dependent) contact angle hysteresis, which complicates the experiments. As we cannot exclude variations in the air-substrate IFT (γ_{vs}), the additional quantity that results from the combined analysis of γ_{ow} and θ_Y under such conditions is merely the difference $\gamma_{ws} - \gamma_{vs}$.

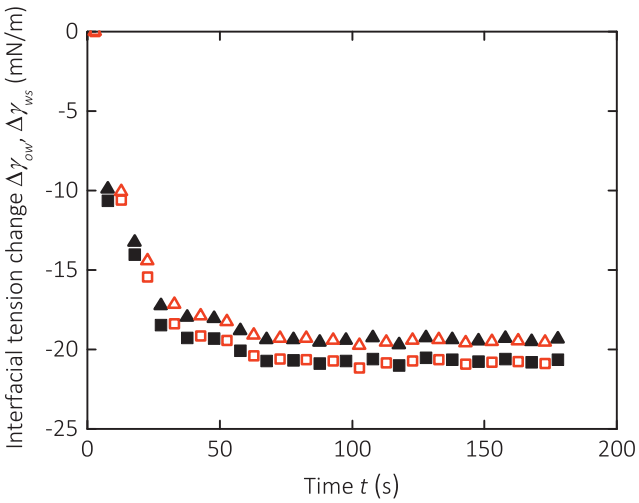

Figure 5 Change in oil-water (squares) and water-substrate (triangles) interfacial tension versus time for aqueous drops with 0.001 wt% Triton X-100 in ambient heptane (t_{ramp} = 5 s), as determined for increasing (black, solid) and decreasing (red, open) voltages.

4.4 Conclusions

We demonstrated that time-resolved electrowetting in an open chip geometry can be used to measure the dynamic oil-water interfacial tension by analyzing the variation in contact angle with the applied voltage as a function of drop age. In addition, information about the complex drop-(oil)-substrate interface can be obtained. In the measurement strategy it is assumed that the drop's response to a voltage change occurs in a much shorter time than the characteristic adsorption time of the surfactant. Typical processes that can be resolved have a relaxation time of O(10 s) and involve interfacial tension changes by more than 10%.

Besides yielding more than one IFT, our method also has the advantage that it requires neither a density difference between the fluid phases, nor drop sizes of O(1 mm). Although not explicitly shown here it is obvious that the method can be implemented in wireless configurations using an EW single surface with interdigitated electrodes [22]. Next to integration into single-surface EW devices [26, 33] this also enables the analysis of sample volumes down to 20 nL or less.

References

[1] S.Y. Teh, R. Lin, L.H. Hung and A.P. Lee, *Droplet microfluidics*, Lab Chip 8 (2008), 198-220.

[2] M. Abdelgawad and A.R. Wheeler, *The digital revolution: A new paradigm for microfluidics*, Adv. Mater. 21 (2009), 920-925.

[3] M.J. Jebrail and A.R. Wheeler, *Let's get digital: digitizing chemical biology with microfluidics*, Curr. Opin. Chem. Biol. 14 (2010), 574-581.

[4] V. Srinivasan, V.K. Pamula and R.B. Fair, *An integrated digital microfluidic lab-on-a-chip for clinical diagnostics on human physiological fluids*, Lab Chip 4 (2004), 310-315.

[5] I. Barbulovic-Nad, H. Yang, P.S. Park and A.R. Wheeler, *Digital microfluidics for cell-based assays*, Lab Chip 8 (2008), 519-526.

[6] J.Y. Yoon and R.L. Garrell, *Preventing biomolecular adsorption in electrowetting-based biofluidic chips*, Anal. Chem. 75 (2003), 5097-5102.

[7] A. Bange, H.B. Halsall and W.R. Heineman, *Microfluidic immunosensor systems*, Biosens. Bioelectron. 20 (2005), 2488-2503.

[8] M.D. Goldberg, R.C. Lo, S. Abele, M. Macka and F.A. Gomez, *Development of microfluidic chips for heterogeneous receptor-ligand interaction studies*, Anal. Chem. 81 (2009), 5095-5098.

[9] A.H.C. Ng, U. Uddayasankar and A.R. Wheeler, *Immunoassays in microfluidic systems*, Anal. Bioanal. Chem. 397 (2010), 991-1007.

[10] S.D. Hudson, J.T. Cabral, W.J. Goodrum, K.L. Beers and E.J. Amis, *Microfluidic interfacial tensiometry*, Appl. Phys. Lett. 87 (2005), 081905.

[11] J.T. Cabral and S.D. Hudson, *Microfluidic approach for rapid multicomponent interfacial tensiometry*, Lab Chip 6 (2006), 427-436.

[12] N.T. Nguyen, S. Lassemono, F.A. Chollet and C. Yang, *Microfluidic sensor for dynamic surface tension measurement*, IEE Proceedings Nanobiotechnol. 153 (2006), 102-106.

[13] J.H. Xu, S.W. Li, W.J. Lan and G.S. Luo, *Microfluidic approach for rapid interfacial tension measurement*, Langmuir 24 (2008), 11287-11292.

[14] K. Wang, Y.C. Lu, J.H. Xu and G.S. Luo, *Determination of dynamic interfacial tension and its effect on droplet formation in the T-shaped microdispersion process*, Langmuir 25 (2009), 2153-2158.

[15] M.L.J. Steegmans, A. Warmerdam, K.G.P.H. Schroen and R.M. Boom, *Dynamic interfacial tension measurements with microfluidic Y-Junctions*, Langmuir 25 (2009), 9751-9758.

[16] H. Gu, M.H.G. Duits and F. Mugele, *Interfacial tension measurements with microfluidic tapered channels*, Colloids Surf. A 389 (2011), 38-42.

[17] M.G. Pollack, A.D. Shenderov and R.B. Fair, *Electrowetting-based actuation of droplets for integrated microfluidics*, Lab Chip 2 (2002), 96-101.

[18] S.K. Cho, H.J. Moon and C.J. Kim, *Creating, transporting, cutting, and merging liquid droplets by electrowetting-based actuation for digital microfluidic circuits*, J. Microelectromech. Syst. 12 (2003), 70-80.

[19] R.B. Fair, *Digital microfluidics: is a true lab-on-a-chip possible?*, Microfluid. Nanofluidics 3 (2007), 245-281.

[20] F. Mugele, M.H.G. Duits and D. Van Den Ende, *Electrowetting: A versatile tool for drop manipulation, generation, and characterization*, Adv. Colloid Interf. Sci. 161 (2010), 115-123.

[21] O. Raccurt, J. Berthier, P. Clementz, M. Borella and M. Plissonnier, *On the influence of surfactants in electrowetting systems*, J. Micromech. Microeng. 17 (2007), 2217-2223.

[22] A.G. Banpurkar, K.P. Nichols and F. Mugele, *Electrowetting-based microdrop tensiometer*, Langmuir 24 (2008), 10549-10551.

[23] A. Ahmadi, K.D. Devlin, H. Najjaran, J.F. Holzman and M. Hoorfar, *In situ characterization of microdroplet interfacial properties in digital microfluidic systems*, Lab Chip 10 (2010), 1429-1435.

[24] A.G. Banpurkar, M.H.G. Duits, D. Van Den Ende and F. Mugele, *Electrowetting of complex fluids: Perspectives for rheometry on chip*, Langmuir 25 (2009), 1245-1252.

[25] W.C. Nelson, H.P. Kavehpour and C.-J. Kim, *A miniature capillary breakup extensional rheometer by electrostatically assisted generation of liquid filaments*, Lab Chip 11 (2011), 2424-2431.

[26] M. Abdelgawad, S.L.S. Freire, H. Yang and A.R. Wheeler, *All-terrain droplet actuation*, Lab Chip 8 (2008), 672-677.

[27] F. Li and F. Mugele, *How to make sticky surfaces slippery: Contact angle hysteresis in electrowetting with alternating voltage*, Appl. Phys. Lett. 92 (2008), 244108.

[28] F. Mugele and J.C. Baret, *Electrowetting: From basics to applications*, J. Phys.: Condens. Matter 17 (2005), R705-R774.

[29] Note that compared to the measurements of Ahmadi et al. [23] much smaller variations of the capacitance are expected in our system, as the thickness of the dielectric layer (3.5 micrometers) is orders of magnitude larger than the thickness of the adsorption layer and the entrapped oil layer.

[30] N.J. Alvarez, L.M. Walker and S.L. Anna, *A non-gradient based algorithm for the determination of surface tension from a pendant drop: Application to low Bond number drop shapes*, J. Colloid Interf. Sci. 333 (2009), 557-562.

[31] C. Quilliet and B. Berge, *Investigation of effective interface potentials by electrowetting*, Europhys. Lett. 60 (2002), 99-105.

[32] A. Staicu and F. Mugele, *Electrowetting-induced oil film entrapment and instability*, Phys. Rev. Lett. 97 (2006).

[33] U.C. Yi and C.J. Kim, *Characterization of electrowetting actuation on addressable single-side coplanar electrodes*, J. Micromech. Microeng. 16 (2006), 2053-2059.

Chapter 5

Influence of contact angle hysteresis on the morphology and position of drops confined between a sphere and a plane

Drops confined between a sphere and a plane can attain different shapes and positions, depending on the contact angle (θ) of the liquid on the confining surfaces, the (normalized) drop volume ($\tilde{V}$), and the separation distance ($\tilde{s}$) between sphere and plane. In this study we compare experimental measurements to numerical calculations with Surface Evolver (SE). For the ideal system, a continuous and fully reversible transition between axisymmetric non-spherical shapes (for small θ and $\tilde{V}$) and non-axisymmetric spherical shapes (for large θ and $\tilde{V}$) is predicted. Increasing the contact angle above its critical value θ_c leads to a progressive outward motion of the drop. Experimentally, gradual variation of the contact angle is achieved *via* electrowetting. Discrepancies between the experiments and the calculations were found, in particular for weak confinement (small $\tilde{V}$ and/ or large $\tilde{s}$). A substantial history-dependence in the shape and position of the drop can then occur. Additional analysis with SE of the forces that drive the drop towards equilibrium reveals that even small counteracting pinning forces due to microscopic heterogeneities can drastically alter the drop behavior. Depending on the experimental conditions the outward movement of the drop following pinning can be either continuous or discontinuous.

This chapter is in preparation as R. de Ruiter, M. van Gorcum, C. Semprebon, M.H.G. Duits, M. Brinkmann and F. Mugele, *Influence of contact angle hysteresis on the morphology and position of drops confined between a sphere and a plane.* The numerical work is performed by C. Semprebon and M. Brinkmann.

5.1 Introduction

The trapping of small fluid volumes in contact with solid surfaces is a wide-spread phenomenon in nature and engineering. Examples include the entrapment of drops in the mesoscale roughness of a contacting surface [1], in the pore throats of a solid (*e.g.*, a catalyst particle, a filter, or oil-containing rock), or by specifically designed structures in microfluidic channels [2-4]. Release of the entrapped drops can then be attained in various ways, for example by changing the trapping force [5] or the external force (gravity or pressure drag), increasing the drop size *via* coalescence, or decreasing the wettability of the solids, *e.g.*, *via* surface modification. In many practical situations however, contact angle hysteresis originating from microscopic surface heterogeneities can seriously hamper the release and subsequent removal of drops. In this chapter we approach the problem of drop release by taking a sphere/ plane system as a model confining geometry (see Figure 1). To elucidate the role of hysteresis, we analyze the shape and position of the confined drop under equilibrium conditions, and compare the mechanical driving forces towards this equilibrium to typically occurring pinning forces.

In the absence of a net external force, liquid drops attain a constant mean curvature shape (see Section 2.1.4). Depending on the geometry of the confinement and the wettability of the surfaces, energy minimization can lead to different morphologies. Axisymmetric meniscus shapes between a sphere and a plane have been theoretically investigated by Orr *et al.* [6]. Upon increasing the liquid volume, the shape follows the sequence of Delaunay shapes [7] as described by Plateau [8] from a portion of an inner nodoid, to a catenoid, unduloid, cylinder, unduloid, sphere, and finally an outer nodoid. The actual start and end points within this sequence depend on the contact angle on both solids. For small liquid volumes or large solid separations, the liquid bridge breaks up and the liquid is distributed over the solids [9-13]. If gravity is negligible, the only forces acting on the contacting solids are the axial component of the surface tension acting at the three phase contact line, and the capillary pressure acting on the liquid-solid interfaces. The surface tension force is always attractive, and the capillary pressure force can be either attractive or repulsive depending on the curvature κ. While increasing the volume, a liquid bridge exerts an attractive net force on the solids until a spherical shape is attained [6, 14]. These attractive liquid bridges have been investigated intensively [9, 11, 12, 15-18] due to their relevance in the cohesion of wet granular materials [19] and colloids [20].

Of particular importance for the present work, is that a spherical profile is shown to have a critical curvature $\kappa = \kappa_c$ at which the liquid bridge no longer exerts a net attractive force

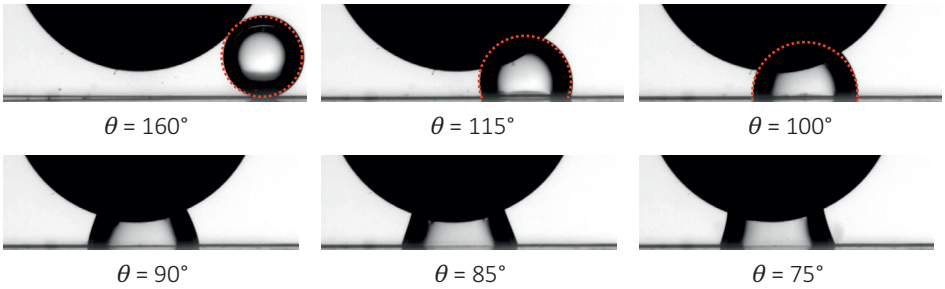

Figure 1 Sequence of experimental drop morphologies ($\tilde{V} = 0.1$ and $\tilde{s} = 0.2$, $\theta_c = 100°$).

[6, 14, 21]. Upon increasing the drop volume further such that an outer nodoid profile is obtained, the repulsive capillary pressure force will exceed the attractive surface tension force, resulting in a net repulsion. Outer nodoidal bridges have been shown to be unstable with respect to small asymmetric perturbations [14, 22]. The liquid bridge then breaks symmetry and moves away from the symmetry axis of the sphere/ plane geometry to assume a zero-force spherical shape. This non-axisymmetric liquid bridge is of lower free energy, and can be attained without passing energy barriers [14]. This situation is fundamentally different from drops which are wetting a single fiber [23, 24], or that are enclosed between two fibers [25, 26] (see Chapter 6), in which cases energy barriers between the different morphologies result in discontinuous transitions. Remarkably, although the actual radial position of the non-axisymmetric liquid bridge has been stated to depend on the volume and the boundary conditions [14], a quantification of this displacement was never reported. This off-axis distance is however important in scenarios where drops ultimately have to be removed from their confinement.

Contact line pinning provides an additional ingredient, which can drastically alter the morphology of a drop. Various examples hereof can be found in literature, where the pinning was 'engineered' by creating surface patterns on the scale of the drop size. Contact line pinning at the boundaries between surface domains with a large wettability contrast (*e.g.*, circular [27, 28], striped [29-32], and ring-shaped [33, 34] domains) or at the sharp edges of a structured substrate [35, 36] was found to be responsible for the existence of multiple possible morphologies. In many practical situations however, pinning forces instead originate from submicron scale heterogeneities of either chemical ('patchiness') or topographical ('roughness') nature, which are much smaller than the drop size. Such microscopic heterogeneities can be demonstrated with high resolution imaging techniques such as AFM, but in wetting studies they are mostly characterized at

the macroscopic level *via* the difference between the advancing and receding contact angles, *i.e.*, *via* the contact angle hysteresis.

In this chapter we study the shape and radial position of a drop in a sphere/ plane geometry using a twofold approach. We examine the symmetry breaking and radial position of the drop upon changes in the contact angle in the idealized system (*i.e.*, without microscopic heterogeneity) *via* numerical calculations using the Surface Evolver [37] and geometric analysis. This symmetry breaking involves movement of the contact lines on both the sphere and the plane. The influence of contact angle hysteresis is determined by comparing forces derived from the energy landscape to typical pinning forces. This framework is then used to analyze a series of experiments in which the drop volume, the sphere/ plane separation, and the equilibrium contact angle are varied systematically. Variation of the latter is facilitated by making use of electrowetting [38].

5.2 Materials and methods

5.2.1 Experimental set-up

A stainless steel sphere (radius $R = 1$, 2 mm) and an indium tin oxide-coated glass slide are coated with 2 µm of insulating Parylene C by vapor deposition. These substrates are then covered with a thin hydrophobic top layer *via* dip coating in dilute (0.01%) Teflon AF solution in FC40 (DuPont). Ambient silicon oil (Fluka AS 100, density $\rho \approx 995$ kg/m^3, interfacial tension with water $\gamma \approx 30$ mN/m) is used to prevent evaporation, reduce the intrinsic contact angle hysteresis to below 2°, and eliminate gravity effects as indicated by the small Bond number $Bo = g\Delta\rho r^2/\gamma \approx 10^{-2}$ (with g the gravitational acceleration, $\Delta\rho$ the density difference, and $r = V^{1/3}$ the typical length scale of the drop). A single aqueous drop (KCl added up to a conductivity of 3 mS/cm) of microliter volume V is pipetted onto the plane, after which the sphere is brought in contact with the drop. An alternating (AC) voltage is applied to the drop *via* a thin gold wire that is glued to the plane, and both substrates are grounded (Figure 2). The preferred direction for the radially outward movement upon increasing θ is usually along the gold wire, which is placed such that the drop moves in the field of view. Distortion of the drop shape by the gold wire is negligible.

5.2.2 Contact angle manipulation

Variations in the drop shape and position are obtained by varying the contact angle of the drop with the solid surfaces. We use electrowetting (EW) to continuously and reversibly

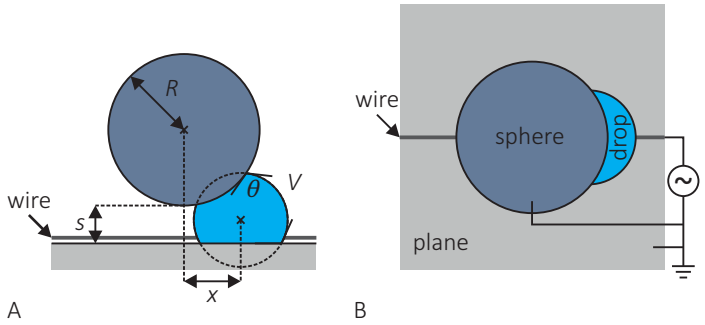

Figure 2 Schematic (A) side view and (B) top view of a drop confined in a sphere/ plane geometry. Both substrates consist of an electrode covered with an insulating layer and hydrophobic coating. The characteristic parameters (R, s, V, θ, x) are indicated in (A).

manipulate the contact angle [38]. The voltage is applied between the insulator-covered electrodes and the conductive drop. For the voltage range (U = 0-120 V; AC frequency: 1 kHz) used in our experiments, the macroscopic contact angle θ measured through the water drop varies between 170° and 70°, following the EW equation $\cos\theta = \cos\theta_Y + \varepsilon_0\varepsilon_d U^2/(2d\gamma) = \cos\theta_Y + \eta$. Here, $\theta_Y \cong 170°$ is the Young angle, ε_0 the permittivity of vacuum, ε_d the dielectric constant of the insulator, and d its layer thickness. The dimensionless electrowetting number η compares the magnitudes of the electrostatic and interfacial energies. The contact angle becomes more or less voltage-independent for $\eta >$ 1.3. We ensure equal contact angles on both contacting solids by grounding the sphere and the plane.

5.2.3 Measurement of characteristic geometric parameters

All characteristic parameters (R, s, V, θ, x) are extracted from side view recordings *via* a custom-written MATLAB code that locates the system boundaries by edge detection (Figure 2A). The lower apex of the sphere with radius R is separated from the plane by a distance s. The volume is determined at the maximum radial position, where the error introduced by the truncation of the spherical drop by the bounding solid surfaces is negligible compared to the error due to the determination of the radius (the latter is ~3%). Contact angles are measured on the sphere as determination on the plane is hindered by the gold wire. We found that the obtained θ values agree reasonably well with the electrowetting equation (especially for decreasing θ). Due to the finite optical resolution and the curved geometry of our system, the measured angles tend to underestimate the actual contact angles by about 5°. To quantify the drop behavior we

measure the radial position of the midpoint of the projected area of the drop with respect to the symmetry axis of the sphere/ plane geometry x.

It is convenient to make use of non-dimensionalized quantities (denoted by a tilde), where we choose the radius of the sphere R as characteristic length scale (the other length scale is s). Thus, all length scales are normalized by R, volumes by R^3, energies by the interfacial energy scale γR^2, and forces by the interfacial force scale γR.

5.2.4 Numerical analysis

Drop shapes are computed by minimizing the interfacial energy under the constraint of a fixed liquid volume V with public domain software Surface Evolver. The interface between the two immiscible liquids is represented by a mesh of nodes connected by the edges of triangular facets. Nodes belonging to the contact line are constrained to move in the plane of the planar substrate or on the surface of the sphere. Because of symmetry, only half of the system is considered, and the mesh is gradually refined close to the contact line and the symmetry center to improve the accuracy. To determine the energy landscape for a given set of parameters (R, s, V, θ), we impose an additional constraint on the position of the center of mass of the drop x_{cm}, and shift it inwards and outwards in small steps. The Lagrange multipliers for the volume and center of mass position constraints are the Laplace pressure of the drop and the force pulling the liquid in- or outward, respectively. The convergence of the minimization suffers from a critical slowing down close to the transition between axisymmetric and non-axisymmetric shapes. We thus performed *a posteriori* analysis of sequences of energy landscapes, by tracking the position of the energy minima, to precisely determine the critical angles and volumes for the symmetry-breaking.

5.3 Results

We determined the radial position $\tilde{x} = x/R$ during θ variations for various experimental conditions. Figure 3 shows the results for fixed drop volume $\tilde{V} = V/R^3$ and several sphere/ plane separation distances $\tilde{s} = s/R$. Initially, the drop is strongly non-wetting ($\theta_Y \approx 170°$), and attains a spherical shape at a radial position close to the theoretical maximum. As expected, this value is larger for more strongly confined drops, *i.e.*, for smaller $\tilde{s}$ and for larger $\tilde{V}$. A gradual decrease in contact angle initially causes the liquid to move progressively inward at increasing pace. The drop indeed retains a spherical shape (see the upper row of Figure 1) as mentioned in Section 5.1. We note in Figure 3 that

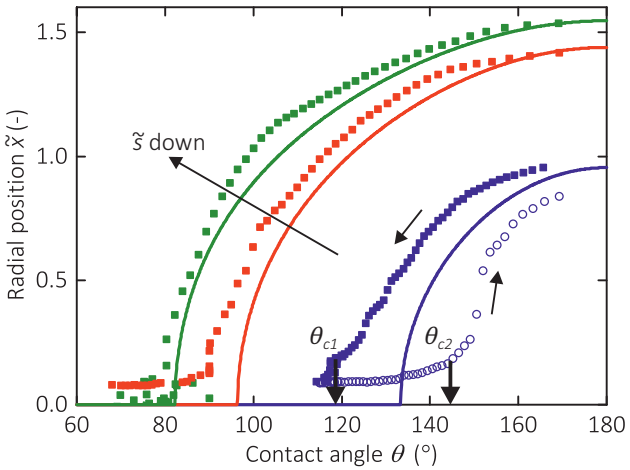

Figure 3 Bifurcation diagram: radial position versus contact angle for a drop ($\tilde{V} = 1$) with three different sphere/ plane separations; $\tilde{s} = 0.2$ (green), 0.5 (blue), and 1.0 (red). The experimental data for decreasing θ (filled squares) and increasing θ (open circles) are compared to the predicted radial positions as determined with a geometric analysis (solid lines). The data for increasing θ are only included if the drop moves outward perpendicular to the viewing direction (here for $\tilde{s} = 1$).

drops usually remain non-axisymmetric for the entire θ range and attain a small but finite value x_{min}. We thus define a threshold; $\theta_{c1}(\tilde{V}, \tilde{s})$ is defined as the contact angle where $\tilde{x}$ is reduced by 90% of the total difference $\tilde{x}_{max} - \tilde{x}_{min}$. For strongly confined drops a highly non-axisymmetric shape is favored, and thus θ_{c1} is smaller compared to weakly confined drops. After virtually reaching the symmetry axis, the drop attains a non-spherical shape. A sequence of constant mean curvature shapes is expected upon further decreasing the contact angle [6] (see the lower row of Figure 1). The types of mean curvature shapes that can be observed experimentally are restricted, as the contact angle does not decrease below ~70° due to contact angle saturation [38].

During the subsequent θ increase two different scenarios can be observed. In the first one the drop is momentarily pinned, after which a further gradual increase of θ results in a continuous outward movement of the drop. In the second scenario the drop remains stuck close to the symmetry axis of the sphere/ plane geometry for a longer interval (in some cases for the entire θ range), until it suddenly moves outward in a discontinuous manner. Depending on the minimum contact angle θ_{min} imposed during the experiment, one finds a contact angle $\theta_{c2} > \theta_{c1}$ at which the drop starts to move outward.

Experimentally, we thus find a history-dependence for the drop position, which is more pronounced for weakly confined drops.

These experimental findings can be compared to the $(\theta, \tilde{x})$ relationship as determined from a purely geometric analysis, assuming that the non-axisymmetric drop has a spherical shape (see Appendix 5A for the mathematical derivation). This assumption for the shape, which is in good agreement with our observations and is also corroborated by our Surface Evolver calculations, imposes a functional dependence of $\tilde{x}$ on θ, for each combination of $\tilde{s}$ and $\tilde{V}$ (which are constant in each experiment). As can be seen from Figure 3, the geometric analysis captures our experimental $\tilde{x}(\theta)$ data with different levels of success: for weakly confined drops (red symbols) the correspondence is only qualitative, while for strongly confined drops it is almost quantitative. The qualitative volume- and separation dependence of $\tilde{x}_{max}$ and θ_{c1} is predicted adequately (as shown here for the separation dependence). The observed deviations clearly indicate that a physical ingredient is missing in the modeling (the more so for weakly confined drops). As will be elaborated in Section 5.4, these deviations are very likely due to contact angle hysteresis.

The geometric analysis yields a critical contact angle θ_c characterizing the transition between non-axisymmetric and axisymmetric shapes. As shown in Figure 3, θ_c decreases upon repeating the experiments for a smaller sphere/ plane separation at the same drop volume. Similarly, experiments with larger $\tilde{V}$ for constant $\tilde{s}$ result in a θ_c decrease. As long as $\tilde{V}$ and $\tilde{s}$ are the same, identical results should be obtained, independent of the actual values of the drop volume, sphere/ plane separation, and the sphere radius. Plotting the critical contact angle as a function of the reduced volume thus yields a unique theoretical stability limit for every reduced sphere/ plane separation, and thus a theoretical morphology diagram in terms of the control parameters θ, $\tilde{V}$, and $\tilde{s}$. This diagram is plotted in Figure 4 as $\tilde{V}_c(\theta_c)$ for several discrete values of $\tilde{s}$.

Drops with small volumes and small contact angles are axisymmetric, and can break their symmetry upon increasing either θ or $\tilde{V}$. The stability limit shifts to larger θ and $\tilde{V}$ upon increasing $\tilde{s}$. Non-wetting (*i.e.,* $\theta > 90°$) axisymmetric drops in between a contacting sphere and plane ($\tilde{s} = 0$) can only form a nodoid profile, and thus always exerts a repulsive force [6]. Such drops will thus break symmetry regardless of their volume. In Figure 4 this condition is found as a vanishing critical drop volume at $\theta = 90°$ for $\tilde{s} = 0$. For non-contacting substrates $\tilde{s} > 0$ there is a minimum volume $\tilde{V}(\theta)$ for which liquid bridges exist. Upon decreasing the volume below the critical value the liquid bridge

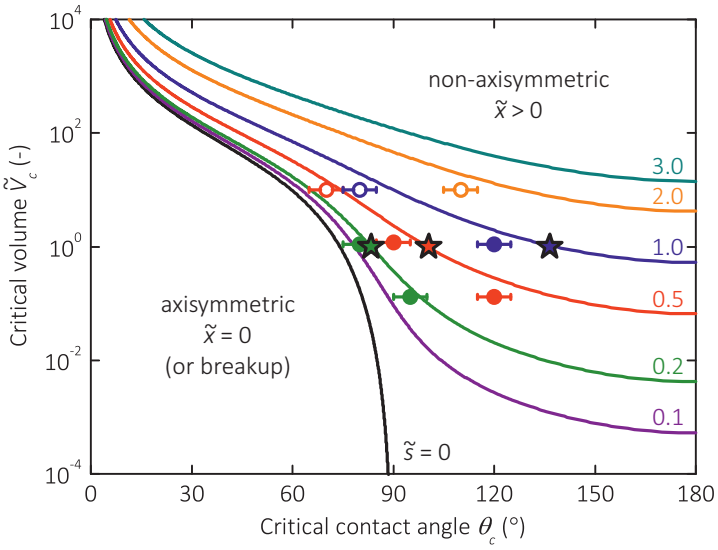

Figure 4 Morphology diagram showing the critical combinations $(\theta, \tilde{V})_c$ for various sphere/plane separations $\tilde{s}$. The experimental results for decreasing θ (circles, with error bars of ±5°) are compared to the predictions from the geometric analysis (solid lines). Experimental data are for spheres with radius $R = 1$ mm (open symbols) and $R = 2$ mm (closed symbols). Data obtained with Surface Evolver calculations are indicated by stars.

breaks. The transition line approaches this critical volume in the limit $\theta_c \rightarrow 180°$. The conditions for this small-volume instability at other θ values and the post-rupture liquid distribution are treated elsewhere [9-13] and will not be discussed here.

Also our experimental data are displayed in Figure 4. We compared θ_{c1} (for decreasing θ) to the predicted value for the critical contact angle, as we found that θ_{c2} (for increasing θ) is strongly dependent on the previously attained minimum contact angle θ_{min} (see also Section 5.4). We again see that θ_{c1} shows the same trends regarding changes in $\tilde{V}$ and $\tilde{s}$ as predicted by the geometric analysis. However, the experimentally determined θ_{c1} values are consistently lower than the predicted θ_c. These deviations are too large to be attributed to the slight underestimation of θ as mentioned in Section 5.2, and rather appear to be due to contact angle hysteresis.

5.4 Discussion

5.4.1 Energy and forces in the 'ideal' system

We numerically calculated the energy landscape of the symmetry breaking in absence of contact angle hysteresis. The interfacial free energy of the system is given by $\tilde{E} = E/\gamma R^2 = \tilde{A}_{wo} - \tilde{A}_{ws}\cos\theta$, where $\tilde{A}_{wo} = A_{wo}/R^2$ and $\tilde{A}_{ws} = A_{ws}/R^2$ are the water-oil and water-solid interfacial areas, respectively. The energy landscape is obtained by letting Surface Evolver minimize the free energy of the system under the additional global constraint of an imposed radial position of the center of mass $\tilde{x}_{cm}$, which is then repeated for an array of closely spaced $\tilde{x}_{cm}$ values. We remark that the definition of $\tilde{x}_{cm}$ deviates slightly from that of $\tilde{x}$ as used in our geometric analysis and experiments; this small discrepancy will however not affect any of our conclusions.

Figure 5A shows the energy landscape for several contact angles. For clarity, offsets are subtracted such that all axisymmetric shapes have zero interfacial energy. For every θ only one energy minimum is present, meaning that the equilibrium shape and position of the drop are uniquely defined by $\tilde{V}$, $\tilde{s}$ and θ in the ideal system. For small contact angles, axisymmetric shapes with $\tilde{x}_{cm} = 0$ display the lowest energy. However beyond a $\tilde{V}$- and $\tilde{s}$-dependent critical contact angle θ_c, the energy minimum is found at a finite radial position $\tilde{x}_{cm}$ corresponding to a non-axisymmetric drop, while the position $\tilde{x}_{cm} = 0$ transforms into a local maximum. As θ is increased further, the energy minimum shifts gradually to a larger $\tilde{x}_{cm}$. The absence of energy barriers implies that the transition should be continuous and fully reversible. To find the precise contact angle for the transition, one can use the requirement that the second variation $\mathrm{d}^2\tilde{E}/\mathrm{d}\tilde{x}_{cm}{}^2$ in the minimum of the potential should vanish at $\theta = \theta_c$; this is shown in Figure 5B. Critical contact angles thus obtained with Surface Evolver are in very good agreement with the geometric analysis (Figure 4).

From the energy landscapes, we can also determine the magnitude of the external body force that is required to remove (part of) the drop from the sphere/ plane geometry. The force on the drop corresponds to the Lagrange multiplier for the constraint on the center of mass position, and can be calculated either directly or *via* the first variation $\mathrm{d}\tilde{E}/\mathrm{d}\tilde{x}_{cm}$. All energy curves have an inflection point at large $\tilde{x}_{cm}$, which corresponds to the maximum force that can be exerted by the sphere/ plane geometry. As expected the force decreases with increasing θ, and vanishes for $\theta = 180°$ (Figure 5C, D). Surprisingly, for small contact angles an initial increase in the force is observed, which is most likely related

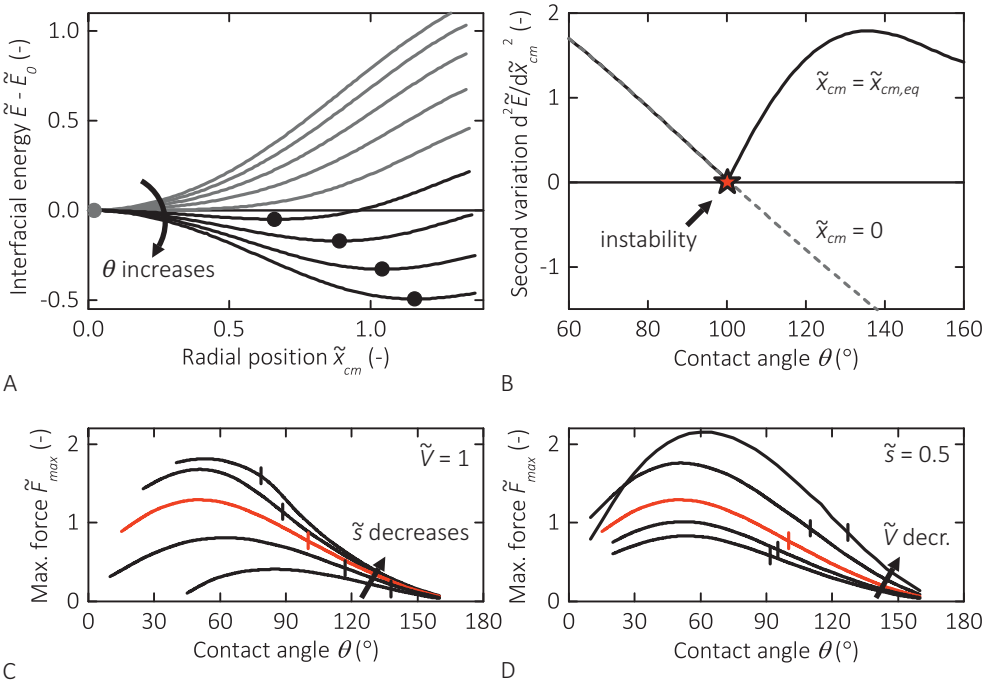

Figure 5 (A) Typical energy landscapes ($\tilde{V} = 1$ and $\tilde{s} = 0.5$, $\theta_c = 100$) calculated for a range of contact angles ($\theta = 60°, 70°, \ldots, 140°$). Gray and black lines indicate axisymmetric and non-axisymmetric equilibrium shapes. The minimum energy configurations are denoted with symbols. (B) The second variation of the energy (*i.e.*, the spring constant of the restoring force) versus contact angle, calculated for both the axisymmetric shape at $\tilde{x}_{cm} = 0$ (gray dashed line) and the minimum energy configuration at $\tilde{x}_{cm} = \tilde{x}_{cm,eq}$ (black solid line). (C, D) Maximum force versus contact angle for (C) a drop with $\tilde{V} = 1$ and various sphere/ plane separations ($\tilde{s} = 0.1$, 0.3, 0.5, 0.75, 1) and (D) a drop with $\tilde{s} = 0.5$ and various drop volumes ($\tilde{V} = 0.2$, 0.5, 1, 1.5, 2). The red curve corresponds to the data in A, B. The vertical lines indicate the respective critical contact angles.

to a change in the pinch off mechanism (for small θ the detachment likely involves the neck of the liquid bridge, while for large θ it involves the interface close to the solids). Curves are terminated at small contact angles close to the contact angle at which the bridge ruptures. Our analysis shows an increase of the maximum trapping force for decreasing $\tilde{s}$ and $\tilde{V}$.

5.4.2 The effect of contact angle hysteresis on the drop position

The most plausible explanation for the experimentally observed hysteresis in the drop position would be the existence of contact angle hysteresis (even though it is rather small for our system) due to microscopic heterogeneity of the used solid surfaces. In general the intrinsic contact angle hysteresis does not have a constant value over the entire θ range. In particular the advancing and receding contact angles θ_A and θ_R induced by topographic defects can be highly sensitive to very small variations in the material's contact angle [39]. Nevertheless, we assume in first approximation that the contact angle hysteresis $\Delta\cos\theta = \cos\theta_R - \cos\theta_A$ is constant. The maximum pinning force on the drop is then estimated by $\tilde{F}_p = F_p/\gamma R \approx \widetilde{W}\Delta\cos\theta$, with $\widetilde{W} = W/R$ the total width of the contact line [31, 40, 41] (consisting of contributions on the sphere and on the plane). The $x_{cm}(\theta)$ path under influence of hysteresis is determined by equating this pinning force to the driving force $\tilde{F} = F/\gamma R = -\mathrm{d}\tilde{E}/\mathrm{d}\tilde{x}_{cm}$, which is derived from the energy landscape (Figure 5A). Deviations from the 'ideal' drop shape induced by the additional stresses at the contact line are neglected.

The force balance is graphically represented in Figure 6. For clarity we only show a selection of the force curves and represent the pinning force by a constant value of $\tilde{F}_p = \pm$ 0.05. In reality (and in our calculations) $\tilde{F}_p$ decreases slightly for increasing θ and increasing $\tilde{x}_{cm}$, due to the decreasing contact line width. For the intermediate contact angles that we consider, $\tilde{F}_p$ ranges from 0.01 to 0.07 for a contact angle hysteresis $\Delta\cos\theta =$ 0.05. To find configurations that are attained for decreasing θ (red symbols) and increasing θ (blue symbols), we solve for $\tilde{F}(\tilde{x}_{cm}) + \tilde{F}_p(\tilde{x}_{cm}) = 0$, *i.e.*, we find the intersection points of the driving force and the pinning force (represented by the light colored lines in Figure 7A).

For decreasing θ (Figure 6A), we find a single intersection point for every θ at $\tilde{x}_{cm} > \tilde{x}_{cm,ideal}$ (the red and black symbols, respectively). As $\tilde{F}(\tilde{x}_{cm})$ is a decreasing function at the intersection points, stable configurations are obtained. While decreasing θ the intersection point shifts continuously to smaller $\tilde{x}_{cm}$, and the $\tilde{x}_{cm}(\theta)$ relationship (the red curve in Figure 7A) is uniquely defined. As opposed to the ideal case the center of mass will never reach the symmetry axis as the driving force goes to zero for $\tilde{x}_{cm} \to 0$. A transition to the axisymmetric shape will thus not be obtained.

For increasing θ (Figure 6B), every curve has either zero or two intersection points at $\tilde{x}_{cm} < \tilde{x}_{cm,ideal}$ (the blue and black symbols, respectively). Two different scenarios can be

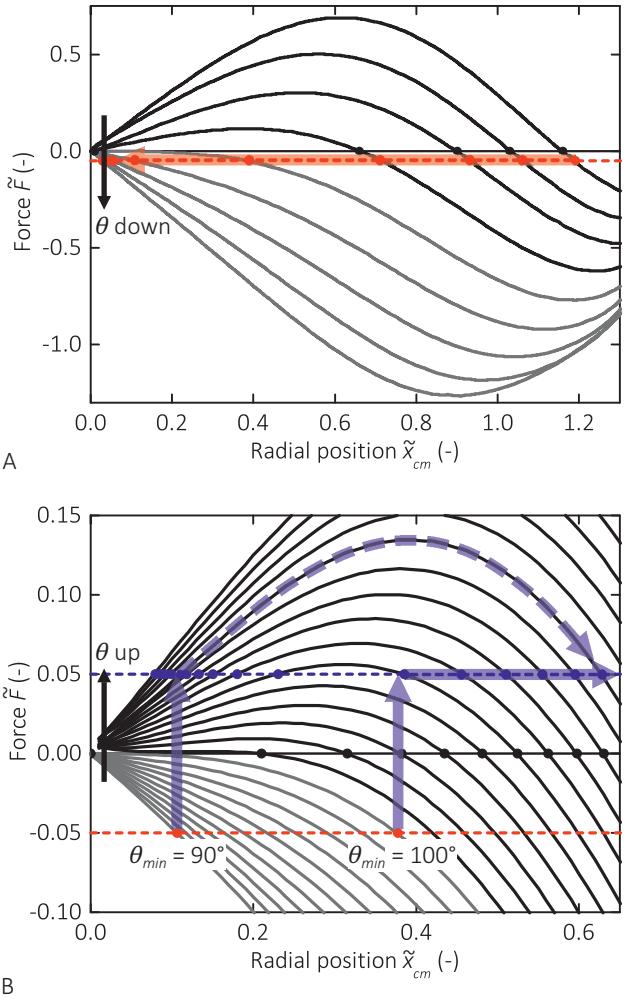

Figure 6 Force versus radial position of the center of mass ($\tilde{V} = 1$ and $\tilde{s} = 0.5$, $\theta_c = 100°$) for a range of contact angles ($\theta = 70°$, 100°, 120°, 140°). Grey and black lines represent axisymmetric and non-axisymmetric equilibrium shapes. The pinning force $\tilde{F}_p = \pm 0.05$ is denoted with dashed red and blue lines. Minimum energy configurations for the ideal system are denoted with black symbols, while the red and blue symbols are intersection points between the driving force and the pinning force. (A) The red arrows show the path taken for decreasing θ ($\theta = 60$, 70°, …, 140°). (B) The blue arrows show paths taken for increasing θ ($\theta = 90$, 91°, …, 115°). For $\theta_{min} = 100°$ the drop moves outward continuously, while for $\theta_{min} = 90°$ the drop moves outward discontinuously (as indicated with the dashed curved arrow).

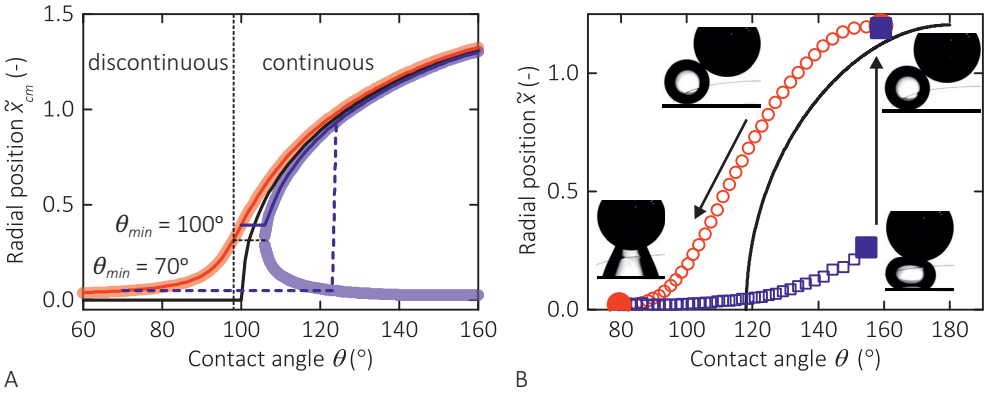

Figure 7 Radial position versus contact angle. The black line gives the equilibrium radial positions $\tilde{x}_{cm,ideal}$ in absence of hysteresis, while the red and blue lines show the effect of hysteresis for decreasing and increasing θ, respectively. (A) The light colored lines indicate the positions of the intersection points. For increasing θ two branches are present. A continuous and a discontinuous outward movement are shown for $\theta_{min} = 100°$ (solid line) and for $\theta_{min} = 70°$ (dashed line), respectively ($\tilde{V} = 1$ and $\tilde{s} = 0.5$, $\Delta \cos\theta = 0.05$). (B) Experimental curves ($\tilde{V} = 1.27$ and $\tilde{s} = 0.83$, $\theta_c = 118°$). The pictures correspond to the data points with large solid symbols.

observed depending on the minimum contact angle θ_{min} and the associated minimum radial position $x_{cm,min}$ that were previously imposed. When θ_{min} is relatively large, the driving force is initially smaller than the maximum pinning force upon increasing θ, causing the drop to be pinned at $x_{cm,min}$. At the intersection point that is reached subsequently, $\tilde{F}(\tilde{x}_{cm})$ is again a decreasing function. A stable configuration is thus obtained, and the drop moves outward continuously upon increasing θ further. An example of this continuous outward movement is given by the right path in Figure 6B and the solid blue line in Figure 7A. However, if θ_{min} is relatively small, we observe a different scenario. The drop is pinned for a larger θ range, and $\tilde{F}(\tilde{x}_{cm})$ is now an increasing function at the intersection point. An unstable configuration is attained, *i.e.*, the driving force increases when the drop moves outward. The drop thus moves outward discontinuously for a fixed θ until the force equilibrium is restored at the second intersection point. Further increasing the contact angle yields a continuous outward movement as in the first scenario. An example of this discontinuous behavior is given by the left path in Figure 6B and the dashed blue line in Figure 7A.

The consequences of even a modest contact angle hysteresis on the position of the drop are remarkably strong. Large deviations from the ideal behavior can be observed,

especially for contact angles close to θ_c. The curves in Figure 7A for $\Delta\cos\theta = 0.05$ correspond to a contact angle hysteresis of a few degrees. For $\Delta\cos\theta = 0.01$, *i.e.*, a hysteresis of about 1 degree, similar to our experiments in ambient oil, the results are very similar (not shown). We note that even for such small pinning forces, very large contact angles are required to move drops outward that have been brought close to the symmetry axis. We also observed this discontinuous outward movement experimentally; a typical result is shown in Figure 7B. A remaining noteworthy difference between the model and the experiments is that in the latter, the jump to a larger radial position is preceded by a stage in which $\tilde{x}_{cm}$ increases gradually. This can be related to deformation of the drop while the contact lines remain pinned, or a transient behavior due to the relatively fast θ ramp (about 1 second per θ step) and the large viscosity ($\eta \approx 100$ mPa·s) of the oil, such that mechanical equilibrium is not completely reached.

5.5 Conclusion

We studied the morphology and position of drops confined between a sphere and a plane, as a model system for ultimately understanding the trapping and release of drops in nature and technology. For ideal systems (without contact angle hysteresis), numerical calculations and geometric analysis demonstrate the presence of a continuous and fully reversible transition between axisymmetric and non-axisymmetric drops upon contact angle variations. Large contact angles and/ or strong confinements are predicted to displace the drop maximally from the axisymmetric position.

However, experiments with small contact angle hysteresis showed remarkable deviations from the ideal system. A transition to the axisymmetric shape was not observed, and in some situations, the drop position $\tilde{x}_{cm}(\theta)$ showed a wide hysteresis loop. This behavior can be explained by comparing the small magnitudes of the wetting forces that drive the drop to its equilibrium morphology to the pinning force. The analysis shows that drops are initially pinned on increasing θ, and can subsequently move outward either continuously or discontinuously, depending on the history of the sample.

References

[1] S. Herminghaus, *Universal phase diagram for wetting on mesoscale roughness*, Phys. Rev. Lett. 109 (2012), 236102.

[2] X. Niu, S. Gulati, J.B. Edel and A.J. Demello, *Pillar-induced droplet merging in microfluidic circuits*, Lab Chip 8 (2008), 1837-1841.

[3] S.S. Bithi and S.A. Vanapalli, *Behavior of a train of droplets in a fluidic network with hydrodynamic traps*, Biomicrofluidics 4 (2010), 044110.

[4] R. Dangla, S. Lee and C.N. Baroud, *Trapping microfluidic drops in wells of surface energy*, Phys. Rev. Lett. 107 (2011), 124501.

[5] R. De Ruiter, A.M. Pit, M. Martins De Oliveira, M.H.G. Duits, H.T.M. Van Den Ende and F. Mugele, *Electrostatic potential wells for on-demand drop manipulation in microchannels*, Lab Chip 14 (2014), 883-891.

[6] F.M. Orr, L.E. Scriven and A.P. Rivas, *Pendular rings between solids: meniscus properties and capillary force*, J. Fluid Mech. 67 (1975), 723-742.

[7] C. Delaunay, *Sur la revolution dont la courbure moyenne est constante*, J. Math. Pure. Appl. 6 (1841), 309-319.

[8] J. Plateau, *The figures of equilibrium of a liquid mass*, Ann. Rep. Smithsonian Inst. (1864), 338-369.

[9] G.P. Lian, C. Thornton and M.J. Adams, *A theoretical study of the liquid bridge forces between 2 rigid spherical bodies*, J. Colloid Interf. Sci. 161 (1993), 138-147.

[10] X. Pepin, D. Rossetti, S.M. Iveson and S.J.R. Simons, *Modeling the evolution and rupture of pendular liquid bridges in the presence of large wetting hysteresis*, J. Colloid Interf. Sci. 232 (2000), 289-297.

[11] C.D. Willett, M.J. Adams, S.A. Johnson and J.P.K. Seville, *Effects of wetting hysteresis on pendular liquid bridges between rigid spheres*, Powder Technol. 130 (2003), 63-69.

[12] L. Yang, Y.S. Tu and H.P. Fang, *Modeling the rupture of a capillary liquid bridge between a sphere and plane*, Soft Matter 6 (2010), 6178-6182.

[13] J.C. Baret and M. Brinkmann, *Wettability control of droplet deposition and detachment*, Phys. Rev. Lett. 96 (2006), 146106.

[14] R.K. Niven, *Force stability of pore-scale fluid bridges and ganglia in axisymmetric and non-axisymmetric configurations*, J. Petrol. Sci. Eng. 52 (2006), 1-18.

[15] G. Mason and W.C. Clark, *Liquid bridges between spheres*, Chem. Eng. Sci. 20 (1965), 859-866.

[16] D.N. Mazzone, G.I. Tardos and R. Pfeffer, *The effect of gravity on the shape and strength of a liquid bridge between 2 spheres*, J. Colloid Interf. Sci. 113 (1986), 544-556.

[17] C.D. Willett, M.J. Adams, S.A. Johnson and J.P.K. Seville, *Capillary bridges between two spherical bodies*, Langmuir 16 (2000), 9396-9405.

[18] Y.I. Rabinovich, M.S. Esayanur and B.M. Moudgil, *Capillary forces between two spheres with a fixed volume liquid bridge: Theory and experiment*, Langmuir 21 (2005), 10992-10997.

[19] M. Scheel, R. Seemann, M. Brinkmann, M. Di Michiel, A. Sheppard, B. Breidenbach and S. Herminghaus, *Morphological clues to wet granular pile stability*, Nat. Mater. 7 (2008), 189-193.

[20] E. Koos and N. Willenbacher, *Capillary forces in suspension rheology*, Science 331 (2011), 897-900.

[21] G. Mason and W. Clark, *Zero force liquid bridges between spherical particles*, Brit. Chem. Eng 10 (1965), 327-328.

[22] T.I. Vogel, *Convex, rotationally symmetric liquid bridges between spheres*, Pac. J. Math. 224 (2006), 367-377.

[23] G. Mchale and M.I. Newton, *Global geometry and the equilibrium shapes of liquid drops on fibers*, Colloids Surf. A 206 (2002), 79-86.

[24] H.B. Eral, J. De Ruiter, R. De Ruiter, J.M. Oh, C. Semprebon, M. Brinkmann and F. Mugele, *Drops on functional fibers: from barrels to clamshells and back*, Soft Matter 7 (2011), 5138-5143.

[25] C. Duprat, S. Protiere, A.Y. Beebe and H.A. Stone, *Wetting of flexible fibre arrays*, Nature 482 (2012), 510-513.

[26] S. Protiere, C. Duprat and H.A. Stone, *Wetting on two parallel fibers: Drop to column transitions*, Soft Matter 9 (2013), 271-276.

[27] P. Lenz and R. Lipowsky, *Morphological transitions of wetting layers on structured surfaces*, Phys. Rev. Lett. 80 (1998), 1920-1923.

[28] P. Blecua, M. Brinkmann, R. Lipowsky and J. Kierfeld, *Morphological transitions of liquid droplets on circular surface domains*, Langmuir 25 (2009), 13493-13502.

[29] H. Gau, S. Herminghaus, P. Lenz and R. Lipowsky, *Liquid morphologies on structured surfaces: From microchannels to microchips*, Science 283 (1999), 46-49.

[30] M. Brinkmann and R. Lipowsky, *Wetting morphologies on substrates with striped surface domains*, J. Appl. Phys. 92 (2002), 4296-4306.

[31] A. Klingner and F. Mugele, *Electrowetting-induced morphological transitions of fluid microstructures*, J. Appl. Phys. 95 (2004), 2918-2920.

[32] D. Ferraro, C. Semprebon, T. Toth, E. Locatelli, M. Pierno, G. Mistura and M. Brinkmann, *Morphological transitions of droplets wetting rectangular domains*, Langmuir 28 (2012), 13919-13923.

[33] P. Lenz, W. Fenzl and R. Lipowsky, *Wetting of ring-shaped surface domains*, Europhys. Lett. 53 (2001), 618-624.

[34] C. Schafle, M. Brinkmann, C. Bechinger, P. Leiderer and R. Lipowsky, *Morphological wetting transitions at ring-shaped surface domains*, Langmuir 26 (2010), 11878-11885.

[35] M. Brinkmann and R. Blossey, *Blobs, channels and "cigars": Morphologies of liquids at a step*, Eur. Phys. J. E 14 (2004), 79-89.

[36] R. Seemann, M. Brinkmann, E.J. Kramer, F.F. Lange and R. Lipowsky, *Wetting morphologies at microstructured surfaces*, Proc. Natl. Acad. Sci. 102 (2005), 1848-1852.

[37] K.A. Brakke, *The Surface Evolver*, Exp. Math. 1 (1992), 141-165.

[38] F. Mugele and J.C. Baret, *Electrowetting: From basics to applications*, J. Phys. Condens. Mat. 17 (2005), R705-R774.

[39] C. Semprebon, S. Herminghaus and M. Brinkmann, *Advancing modes on regularly patterned substrates*, Soft Matter 8 (2012), 6301-6309.

[40] C.G. Furmidge, *Studies at phase interfaces. 1. Sliding of liquid drops on solid surfaces and a theory for spray retention*, J. Colloid Sci. 17 (1962), 309-324.

[41] E.B. Dussan and R.T.P. Chow, *On the ability of drops or bubbles to stick to non-horizontal surfaces of solids*, J. Fluid Mech. 137 (1983), 1-29.

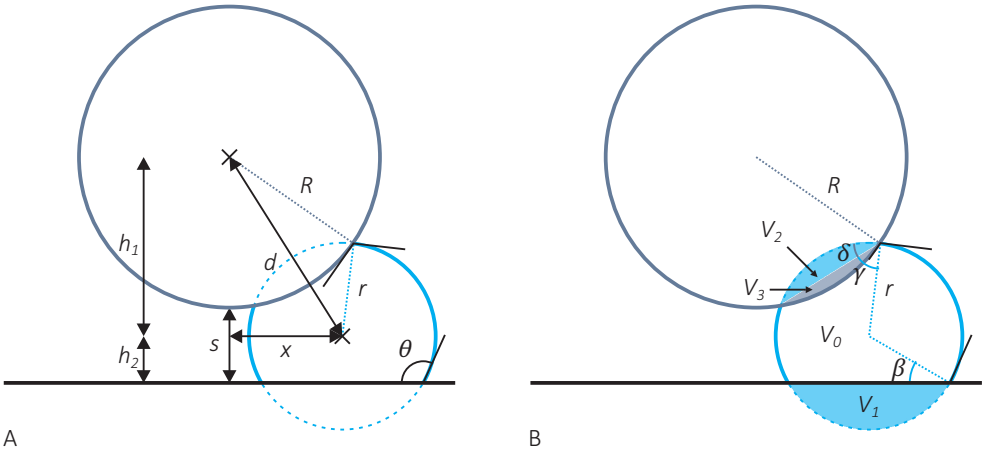

Figure A1 (A) Geometric analysis of a drop in between a sphere and plane (in the symmetry plane) yields the radial position of the center of the fitted sphere x in terms of R, s, θ, and r. (B) The radius of the fitted sphere r is determined from the drop volume V.

Appendix 5A Geometric analysis to obtain the ($\theta, \tilde{x}$) relationship

All non-axisymmetric drops are part of a sphere. The radial position of the center of a circle that is fitted to the drop profile x can be determined from geometry (see Figure A1A). We first write down the relations for the distance d between the centers of the confining sphere and the drop, the height difference h_1 between these centers, and the height difference h_2 between the center of the drop and the plane.

$$d = \sqrt{R^2 + r^2 - 2Rr\cos\theta}$$

$$h_1 = \sqrt{R^2 + r^2 - 2Rr\cos\theta - x^2}$$

$$h_2 = -r\cos\theta$$

The distance s between the lower apex of the sphere and the plane can be expressed as

$$s = h_1 + h_2 - R = \sqrt{R^2 + r^2 - 2Rr\cos\theta - x^2} - r\cos\theta - R$$

Solving for the radial position x yields

$$x = \sqrt{r^2\sin^2\theta - (2R + s)(2r\cos\theta + s)}$$

The maximum radial position x_{max} is attained at $\theta = 180°$. The radius of the spherical drop r can then simply be related to the drop volume, so we obtain

$$x_{max} = \sqrt{(2R + s)\left(2\left(\frac{3V}{4\pi}\right)^{\frac{1}{3}} - s\right)}$$

In the general case of arbitrary θ, the radial position of the drop is a function $x = f(r, R, s, \theta)$. As r is not known, it should first be determined from the drop volume V (see Figure A1B). The volume of the drop is given by

$$V = V_0 - V_1 - V_2 - V_3$$

Here, V_0 is the volume of the sphere with radius r, V_1 the volume of the spherical cap due to the intersection of the spherical drop with the plane, and V_2 and V_3 the volumes of the spherical caps due to the intersection of the spherical drop with the sphere.

$$V_0 = \frac{4}{3}\pi r^3$$

$$V_1 = \frac{1}{3}\pi r^3\{2 - 3\sin\beta + \sin^3\beta\}$$

$$V_2 = \frac{1}{3}\pi r^3\{2 - 3\sin\gamma + \sin^3\gamma\}$$

$$V_3 = \frac{1}{3}\pi R^3\{2 - 3\sin\delta + \sin^3\delta\}$$

The angles β, γ, and δ are given by

$$\beta = \theta - \frac{\pi}{2}$$

$$\gamma = \operatorname{atan}\frac{\frac{r}{R} - \cos\theta}{\sin\theta}$$

$$\delta = \operatorname{atan}\frac{\frac{R}{r} - \cos\theta}{\sin\theta}$$

Thus, the drop volume is a function $V = f(r, R, \theta)$. Knowing the volume, we can solve for r numerically. Subsequently, the radial position x is determined. All equations are non-

dimensionalized by dividing all length scales by R and all volumes by R^3. Examples of the radial position $\tilde{x} = f\left(\tilde{V}, \tilde{s}, \theta\right)$ can be found in Figure 3. The critical contact angle $\theta_c = f\left(\tilde{V}, \tilde{s}\right)$ – which is the angle at which $\tilde{x}$ becomes zero – is shown in Figure 4.

Chapter 6

Buoyant droplets on functional fibers

In the absence of gravity, the wetting of droplets on fibers is characterized by the competition between an axisymmetric barrel morphology engulfing the fiber and a symmetry-broken clamshell morphology with the droplet sitting on the side of the fiber. In the generic case of nonzero buoyancy the cylindrical symmetry of the barrel morphology is broken, yet barrels and clamshells can still be distinguished based on their different interfacial topologies being multiply and simply connected, respectively. Next to contact angle and droplet size the capillary length appears as a third parameter controlling the droplet morphology. For droplets of variable size, contact angle and buoyancy are independently varied in experiments by use of electrowetting and density mismatch. This approach – together with the complementary numerical calculations – provides new insights into the gradual shifts of the stability limits in the presence of an external volume force. Overall, the parameter space for stable clamshells is found to expand with increasing gravitational forces, gradually shrinking the regimes of stable barrels and bistability. In addition, a new stability limit is introduced for the clamshell morphology related to a partial detachment of the wetting liquid from the fiber, appearing toward higher droplet volumes.

This chapter has been published as R. de Ruiter, J. de Ruiter, H.B. Eral, C. Semprebon, M. Brinkmann and F. Mugele, *Buoyant droplets on functional fibers*, Langmuir 28 (2012) 13300-13306. R. de Ruiter and J. de Ruiter contributed equally to this work. The numerical work is performed by C. Semprebon and M. Brinkmann. We thank Astrid Molinier for performing initial experiments.

6.1 Introduction

Droplets on fibers are widely observed in nature, for instance as dew droplets on spider webs, grass, and pine needles, and in traditional engineering applications such as cleaning of textiles [1]. More recently, inspired from nature's way of collecting and transporting dew droplets on spider webs, digital microfluidics on a fiber [2, 3] and bio-inspired fibers for water collection in fog filters [4-6] have been developed. The accumulation of droplets by directional transport is critical to these systems. It has largely been achieved by tuning the fiber shape or inclination: on a horizontal conical wire, the motion of an axisymmetric droplet is driven by a gradient in Laplace pressure [7, 8]. On an inclined fiber, gravity is the driving force [9, 10]. As generally observed under partial wetting conditions contact angle hysteresis hinders droplet motion. To overcome this problem, bioinspired fibers are produced mimicking the structure of spider silk [4-6]: the so-called spindle knots have different surface roughness than the connection elements, thus exerting an additional driving force toward the knot due to the surface energy gradient.

The equilibrium morphology of the droplet on the fiber influences both its attachment to and its motion along the fiber [3] due to the difference in adhesion and contact area. In the absence of buoyancy, two competing droplet morphologies exist: the rotationally symmetric pearl-like 'barrel' structure and the symmetry-broken 'clamshell' that sits at the side of the fiber. The former was described by Plateau [11] in the context of the instabilities of liquid films covering cylindrical fibers; the latter was first noted by Adam [1]. More generally, the two morphologies can also be distinguished by their topology: the liquid interface of the barrel is multiply connected while that of the clamshell is simply connected. This aspect distinguishes the wetting of fibers from other geometries with competing liquid morphologies such as the wetting of stripes [12-14] and the Cassie and Wenzel wetting state on structured surfaces [15, 16]. The morphology transition from the barrel state to the clamshell state has been studied extensively [17-20]. These studies identified the droplet volume and the wettability of the fiber as key control parameters. Only recently, we demonstrated the existence of the inverse transition from the clamshell to the barrel state and showed that reversible switching between both morphologies is possible by tuning the wettability of the fiber using electrowetting [21]. In our combined experimental and numerical study, we identified the stability limits of both morphologies for a density matched oil-water system. Notwithstanding minor quantitative uncertainties, our study clearly revealed fundamental differences between the barrel-to-clamshell and the reverse clamshell-to-barrel transition: the former is caused by a soft

mode of the barrel morphology related to a radial deformation of the droplet, and the latter is linked to a topological transition of the liquid interface.

These results allowed us to construct a complete morphology diagram based on the two control parameters: contact angle and droplet size. The latter is normalized by the radius of the fiber, which is the only intrinsic length scale of the problem in the absence of gravity. In this diagram, clamshells are found to prevail for large contact angles and small volumes, and barrels prevail for small angles and large volumes. For intermediate parameter values, both morphologies are mechanically stable. In the absence of gravity all three regimes – barrel, clamshell, and bistability – extend infinitely toward large droplet volumes.

In the presence of buoyancy, the shape of both barrels and clamshells is distorted [20]. Gravity introduces an additional length scale into the problem, the capillary length $\lambda = (\gamma/g|\Delta\rho|)^{1/2}$. The morphology is thus controlled by three control parameters instead of two. Buoyancy will distinctly change droplet morphology – and thus adhesion to and motion along a fiber – if the droplet size exceeds the capillary length. This obviously happens for large droplet size $L = V^{1/3}$, large density difference $\Delta\rho$, and small interfacial tension γ. Gravitational distortion breaks the axisymmetry of the barrels and thereby lifts the distinction of barrels and clamshells on the basis of symmetry; the distinct topologies however prevail. Chou *et al.* [22] numerically calculated the morphology diagram for water droplets sitting on a fiber and surrounded by air (*i.e.*, for fixed nonzero buoyancy) and showed that the stability of the barrel conformation is greatly reduced. They note specifically that stable barrels are always accompanied by (meta)stable clamshells; *i.e.*, there is no parameter range of exclusive barrel stability. For very large volumes, drops can detach from the fibers.

In this work, we extend our previous work [21] to investigate systematically the stability and the competition of barrel and clamshell morphologies in the presence of buoyancy. Experimentally, we use electrowetting [21] to vary the contact angle on the fiber, and we use liquids of variable density and droplet volume to vary all control parameters independently. This approach provides new insights into the gradual shifts in stability being able to control buoyancy. This allows us to refine the understanding of the role of buoyancy in the appearance of droplet morphologies presented by Chou *et al.* [22]. Complementary numerical calculations minimizing the droplet energy (interfacial and gravitational) give a detailed picture of the energy landscape and show the qualitatively similar nature of the morphology transitions in the absence and presence of buoyancy.

6.2 Materials and methods

6.2.1 Solutions

Calcium chloride is added to a 3 mS/cm potassium chloride solution (both from Sigma-Aldrich) to obtain aqueous solutions with varying density ρ of 1.000, 1.049, 1.199, and 1.400 g/mL as determined with a pycnometer. The interfacial tension γ of the latter three solutions against silicone oil (Fluka, AS 100, viscosity $\eta = 6$ mPa·s) is measured with the pendant drop technique to be 33.0, 39.5, and 46.5 mN/m, respectively. Thus, the liquid-liquid systems have capillary lengths of $\lambda = \infty$, 8.29, 4.50, and 3.44 mm, respectively.

6.2.2 Electrowetting set-up

A stainless steel fiber with radius $r = 0.25$ mm is coated with a 2 µm thick insulating layer of Parylene C by vapor deposition. Subsequently, the fiber is dip coated twice in a 0.1% Teflon solution (DuPont) to obtain a nanometer thick hydrophobic layer. A silicone oil droplet of microliter volume V is placed on the fiber, adopting a low contact angle θ. The fiber is connected to an electrode to which an ac voltage is applied, and the circuit is closed through a grounded electrode in the surrounding aqueous solution (see Figure 1A). The choice for an oil-in-water system has two important implications: first, contact angle hysteresis is mostly eliminated and is thus not influencing the droplet shape (which is a complicating factor in water-air systems [22]). Second, the capillary length of the system can be tuned over a wide range. The ambient aqueous phase is replaced in increasing order of density by simultaneously removing the previous solution from the top of the cuvette and adding the new solution from the bottom, with two syringes pumps. Continuous replacement preserves the oil droplet, which is critical for its volume determination (that is only accurate in the fully symmetric state).

6.2.3 Contact angle manipulation

Continuous and reversible manipulation of the contact angle is achieved *via* electrowetting (EW) [23]. For the voltage range ($U = 0$, ..., 60 V; ac frequency: 1 kHz) in the present experiments, the macroscopic contact angle θ measured through the oil droplet varies between 10° and 80°, following the modified electrowetting equation: $\cos\theta = \cos\theta_Y - (\varepsilon_0\varepsilon_d/2d\gamma)U^2$, which for our curved interface is identical to the planar case [24]. $\theta_Y \cong$ 5-10° is the Young angle (measured through the oil droplet), ε_0 the electric constant, ε_d the dielectric constant of the insulator, and d its layer thickness. Since $d \ll r$, local EW effects near the contact line can be ignored here [25, 26]. The maximum contact

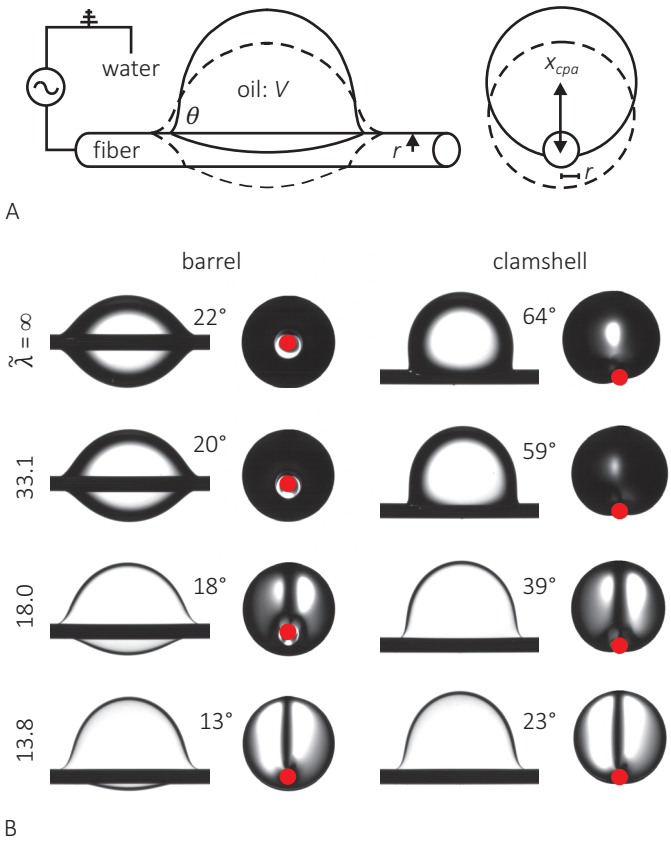

Figure 1 (A) Schematic of the electrowetting setup, showing the side (left) and head-on views (right) of the barrel (dashed) and clamshell (solid) morphologies. The barrel is asymmetric due to buoyancy. The effect of buoyancy is varied by changing the density of the ambient aqueous phase with calcium chloride. The characteristic parameters are the droplet volume V, the fiber radius r, the contact angle θ, and the position of the center of projected droplet area x_{cpa} (here indicated for the clamshell). (B) Side view and head-on view of the barrel and clamshell morphologies upon increasing the effect of buoyancy (decreasing from an infinite reduced capillary length $\tilde{\lambda}$ to a value of 33.1, 18.0 and 13.8) for a droplet with $\tilde{L} = 10.3$. The snapshots are taken just after the clamshell-to-barrel and barrel-to-clamshell transitions, respectively. In the head-on view the fiber is indicated in red (and the image of the vertical part of the bent fiber sticking out above the droplet is erased for clarity).

angle is ~80°. The intrinsic contact angle hysteresis is measured to be below 2°, ensuring that the observed hysteresis in the transitions between barrels and clamshells is indeed caused by the bistability of the two morphologies and not by contact angle hysteresis. The

homogeneity of the vapor deposited Parylene C coating guarantees minimal variations of the contact angle along the fiber. For each condition four subsequent electrowetting cycles are recorded to ensure repeatability of the observed morphology transitions.

6.2.4 Measurement of characteristic parameters

The droplets are observed with two cameras, recording a side view and a head-on view of the fiber. The head-on view enables to unambiguously distinguish the two morphologies from their different topologies, which is not always possible from the side view. The transition is indicated by a steep change in the distance between the center of projected droplet area and the axis of the fiber, x_{cpa} (see Figure 1A). This parameter is analogous to the (3D) center of mass and can be determined more easily in experiments. The characteristic parameters are extracted from the side (θ, V, r) and head-on (x_{cpa}) recordings, using a custom-written MATLAB code that determines the system boundaries by intensity thresholding. The droplet volume $V = f(n, \theta)$ is obtained from the density-matched system at zero buoyancy by integrating the cylindrically symmetric barrel profile using its analytical description [17, 27] in terms of the experimentally determined barrel radius n and contact angle θ. The characteristic length scale of the droplet is defined as $L = V^{1/3}$. The contact angles at the stability limits are obtained by fitting the barrel profile with a linear shape in the vicinity of the triple contact line. The angles are determined just before the barrel-to-clamshell transition and just after the clamshell-to-barrel transition, on the side of the fiber toward which the droplet is moving (*i.e.*, upper side; see Figure 1A). Intermediate contact angles shown in Figure 2 are obtained by interpolating constructed electrowetting curves. The error in the critical contact angles is 3° and is largely determined by the finite resolution of the contact angle measurements.

6.2.5 Numerical modeling

Equilibrium shapes and droplet energies are computed with the public domain software Surface Evolver [28]. In this model, the liquid-liquid interface is represented by a mesh of triangular facets with a gradually increasing refinement in the vicinity of the fiber. Mechanically stable configurations under the global constraint of fixed volume are determined by minimizing the sum of interfacial and gravitational energy

$$E = \gamma\left(A_{ow} - A_{of}\cos\theta - L^3 x_{cm}/\lambda^2\right) \quad \textbf{(Equation 1)},$$

where A_{ow} and A_{of} are the areas of the liquid-liquid (ow: oil-water) interface and the surface of fiber in contact the droplet (of: oil-fiber), respectively. In the numerical model,

the area of the liquid-liquid interface A_{ow} is the total area of all facets, while A_{of} is computed from a line integral along the facet edges forming the contact line. The last term on the right-hand side of Equation 1 is the gravitational contribution to the droplet energy, $E_{grav} = g\int|\Delta\rho|x\mathrm{d}V = g|\Delta\rho|x_{cm}V$, which is directly linked to the vertical displacement of the center of mass of the droplet, $x_{cm} = \int x\mathrm{d}V / \int \mathrm{d}V$. The gravitational term is, similar to the droplet volume, computed as the sum of suitable integrals over the liquid-liquid interface and the three-phase contact line. Hysteresis loops are obtained within a single run by changing the contact angle in small steps during the minimization while keeping the volume fixed. Applying a custom-made 'surgery' to specific elements of the contact line allows changes in the interfacial topology and to detect instability lines of barrel and clamshell morphologies. Transition lines for the droplet detachment are obtained by detecting the pinch off of the liquid neck while increasing the volume at a constant contact angle. All calculations are repeated for different values of λ. Alternatively to the minimization of the sum of interfacial and gravitational energy, we minimize the interfacial energy of the droplet while constraining x_{cm} to a certain, fixed value. Gravitational energy appears as a term linear in x_{cm} (*cf.* the droplet energy Equation 1) and can be added a posteriori to the restricted interfacial energy. Both approaches are thus equivalent and yield the same liquid interface shape. The resulting restricted (or constrained) droplet energy $E_c(x_{cm})$ allows us to determine stable equilibrium shapes of droplets as local energy minima and mechanically unstable configurations corresponding to local energy maxima. In addition, we are able to monitor energy barriers between different stable droplet shapes. More details of the numerical methods can be found in our previous publication [21].

In the remainder of this article we will make use of nondimensionalized quantities denoted by a tilde. In particular, we normalize all lengths by the fiber radius r, areas by r^2, and energies by the interfacial energy scale γr^2, respectively.

6.3 Results

The experiments are carried out as follows. We deposit a highly wetting oil droplet onto the cylindrical fiber in neutrally buoyant ambient water (see Figure 1A). By applying a voltage between the insulator-covered metal fiber and the ambient aqueous phase, the contact angle θ of the oil droplet can be continuously and reversibly changed by virtue of electrowetting [23] (see Section 6.2.3). At zero voltage, θ is small (~5-10°) and the oil droplet adopts the cylindrically symmetric barrel morphology. Upon increasing the voltage

and thus the contact angle, the morphology initially changes continuously while conserving the cylindrical morphology. Under these conditions, the center of the projected area remains at $\tilde{x}_{cpa} = 0$ (filled black symbols in Figure 2A). Upon approaching its stability limit the barrel morphology becomes slightly distorted with $\tilde{x}_{cpa}$ noticeably deviating from zero, presumably due to a minor residual density mismatch (see discussion below). At the critical contact angle θ_{c1}, $\tilde{x}_{cpa}$ abruptly jumps to a finite value as the droplet undergoes the transition from the barrel to the clamshell morphology (upward arrow in Figure 2A). In the clamshell state the droplet shape can again be tuned continuously and reversibly with a continuously decreasing $\tilde{x}_{cpa}$ with decreasing contact angle (open black symbols), until the contact angle decreases below the critical value $\theta_{c2} < \theta_{c1}$. Here, another abrupt transition toward $\tilde{x}_{cpa} = 0$ takes place (downward arrow in Figure 2A), *i.e.*, back to the barrel morphology as depicted in the upper left panel of Figure 1B. For contact angles $\theta_{c2} < \theta < \theta_{c1}$, both the barrel and clamshell morphologies are thus mechanically stable, whereas for $\theta < \theta_{c2}$ and for $\theta > \theta_{c1}$ only the barrel and only the clamshell morphology are stable, respectively. The morphology transition thus displays a strong hysteresis.

After recording the same loop several times, the ambient density-matched water is replaced by water with a higher salt concentration, *i.e.*, with a finite density match, and the same cycle of contact angle variation is repeated. While many qualitative aspects remain the same, the cylindrical symmetry of the barrel state is broken as anticipated and along with it various quantitative properties of the hysteresis loop change as shown by the colored symbols in Figure 2A, B. A number of trends can be seen immediately: comparison of Figures 2A and 2B shows that the effect of the density mismatch is more pronounced for larger droplets (A: $\tilde{L} = 10.3$) than for smaller ones (B: $\tilde{L} = 4.0$), as it should be. In all cases, the asymmetry $\tilde{x}_{cpa}$ increases with increasing density mismatch, as also shown in Figure 1B for barrels and clamshells with $\tilde{L} = 10.3$. The azimuthal orientation of $\tilde{x}_{cpa}$ is no longer random but directional (toward the top) in line with the buoyancy force. The effect of gravity – as quantified by $\tilde{x}_{cpa}$ – is more pronounced for the barrel state as compared to the clamshell state that is already symmetry broken in the absence of buoyancy. All critical angles shift toward smaller values; θ_{c1}, the stability limit of the barrels, more strongly than θ_{c2}, the stability limit of the clamshells. As a consequence, the width $\Delta\theta = \theta_{c1} - \theta_{c2}$ and area of the hysteresis loop in the asymmetry parameter curves both decreases with increasing density mismatch. Following the smaller jump in $\tilde{x}_{cpa}$ during the morphological transition, the difference between barrels and clamshells becomes less important. This qualitative trend also becomes apparent in the superimposed snapshots

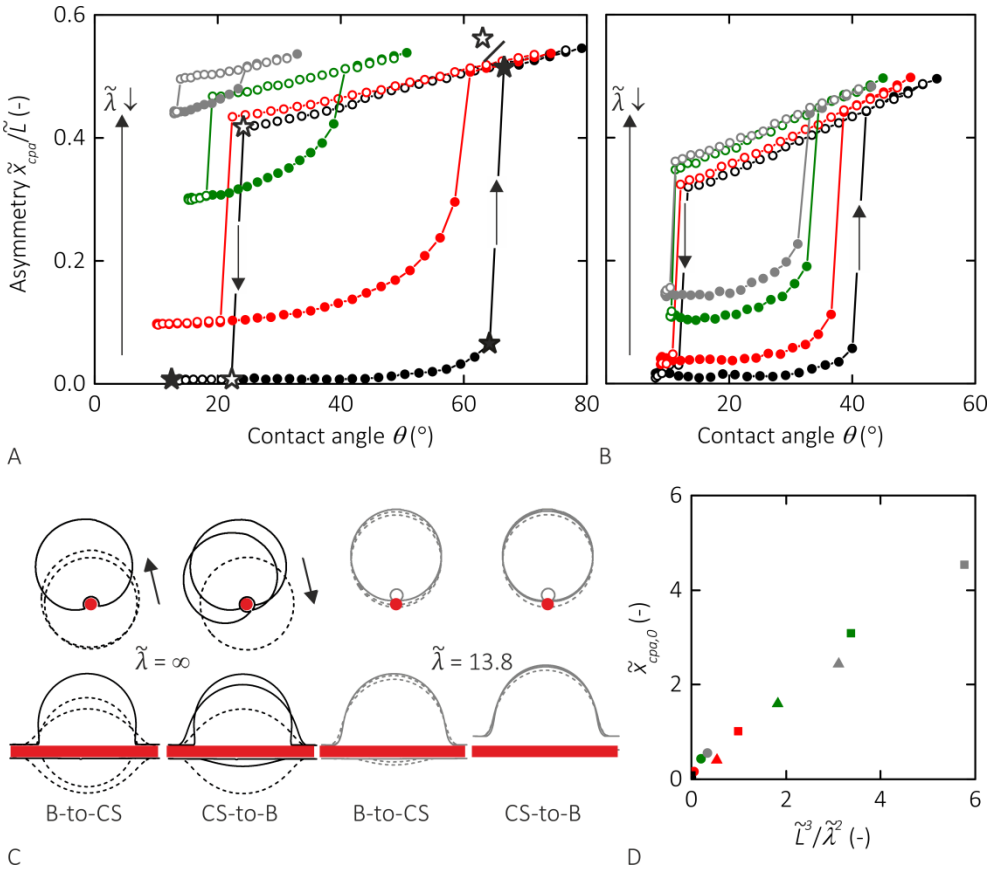

Figure 2 Center of projected area position $\tilde{x}_{cpa}/\tilde{L}$ versus contact angle θ for different values $\tilde{\lambda} = \infty$ (black), 33.1 (red), 18.0 (green), and 13.8 (gray) of the capillary length for (A) a relatively large droplet with $\tilde{L} = 10.3$ and for (B) a relatively small droplet with $\tilde{L} = 4.0$. The filled and open symbols indicate increasing and decreasing contact angles, respectively. (C) Profiles showing the asymmetry of a droplet with $\tilde{L} = 10.3$ in the absence ($\tilde{\lambda} = \infty$, left) and presence of buoyancy ($\tilde{\lambda} = 13.8$, right). The profiles are taken at the points indicated by the stars in (A) for the barrel-to-clamshell (solid stars) and the clamshell-to-barrel transitions (open stars). For $\tilde{\lambda} = 13.8$, the profiles are taken at similar positions in the hysteresis curve. Barrels and clamshells are represented by dashed and solid lines, respectively. (D) Scaling of the (initial) barrel asymmetry with buoyancy (same colors as in (A) and (B)) and droplet size (dots: $\tilde{L} = 4.0$; triangles: $\tilde{L} = 8.4$; squares: $\tilde{L} = 10.3$). The dotted line is the best fit with geometric prefactor 0.82.

of surface profiles shown in Figure 2C. In the absence of gravity (left), a dramatic change in the morphology is readily observed upon crossing both the barrel-to-clamshell and the inverse clamshell-to-barrel transition. In the presence of a substantial density mismatch of $\tilde{\lambda} = 13.8$ (right), however, the global change in morphology turns out to be rather subtle – notwithstanding the fundamental topological difference between a multiply and a simply connected droplet interface.

To understand the results of Figure 2A, B more quantitatively, we consider the effect of the pertinent physical quantities on the drop shape. Since the drop shape is governed by the balance of buoyancy and surface tension forces, we expect that x_{cpa} is governed by the balance of these two forces. Buoyancy scales as $|\Delta\rho| g L^3$ and the spring force due to the stiffness of the drop provided by surface tension as $x_{cpa}\gamma$. (The absolute value of the spring force will include a geometric prefactor that depends on the contact angle.) Balancing the two contributions, we find

$x_{cpa} \propto |\Delta\rho| g L^3/\gamma$ (**Equation 2**).

To verify this scaling behavior, we plot in Figure 2D the normalized value $\tilde{x}_{cpa,0}$ obtained at zero voltage for the barrels in various curves as in Figure 2A, B. Indeed, the data follow the expected behavior. This means that the stiffness of the barrel morphology can be described as a simple harmonic spring. This result is remarkable in view of the rather complex surface morphology and the substantial deformation of the drop between the largest and the smallest capillary length investigated. Since it describes the properties of the drop, this result should also hold for other forces distorting barrel drops, including in particular viscous drag from a flowing ambient phase. The previous statements are also valid for larger contact angles and for the clamshell state, yet limited by nonlinearities close to the transitions and at highly asymmetric shapes. Since the scaling of the governing forces (Equation 2) is the same, variations in the slope of the corresponding curves for the scaled deflection reflect the dependence of the geometric prefactor in the stiffness on the morphology and the contact angle. Overall, clamshells are found to be stiffer than barrels. Upon approaching the critical angle θ_{c1}, barrels soften progressively. This leads to a strong susceptibility to minor deviations of the density mismatch or other imperfections of the system: the slight deviation of $\tilde{x}_{cpa}$ in the (nominal) absence of buoyancy (solid black symbols in Figure 2A, B) could be caused by a density mismatch < 0.005 g/mL, which is consistent with our experimental uncertainty.

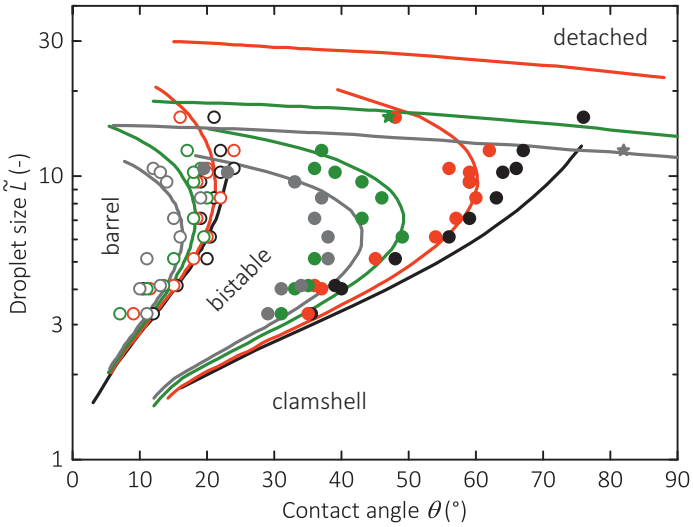

Figure 3 Morphology diagram of millimeter-sized droplets on fibers as a function of contact angle θ and reduced droplet size $\tilde{L}$, for different degrees of buoyancy. The four different colors indicate four different reduced capillary lengths: $\tilde{\lambda} = \infty$ (black), 33.1 (red), 18.0 (green), and 13.8 (gray). The filled circles, open circles, and stars indicate the experimentally observed barrel-to-clamshell, clamshell-to-barrel, and clamshell-to-detached transitions, respectively (with a typical error of 3° in the contact angle determination). The solid lines indicate the numerically determined stability limits of the barrel (right family of curves), and clamshell (left family of curves), and the condition for detachment (upper family of curves).

Plotting the critical angles θ_{c1} and θ_{c2} as a function of reduced droplet size $\tilde{L}$ yields stability limits for the barrel and clamshell morphologies, respectively. The symbols in Figure 3 show these data for a series of values of the reduced capillary length $\tilde{\lambda}$. This yields a universal morphology diagram in terms of all three control parameters θ, $\tilde{L}$, and $\tilde{\lambda}$. As in the neutrally buoyant case, for large θ and small $\tilde{L}$ only the clamshell is mechanically stable for all values of $\tilde{\lambda}$. For small θ and larger $\tilde{L}$ only the barrel is mechanically stable. Yet, both regimes are now bounded at finite $\tilde{L}$, as will be discussed below. The location of both morphological transitions is changing in such a way that the stability region of the barrel morphology including the bistable regime shrink with increasing buoyancy while the clamshell regime expands.

To gain more insight into the stability limits and the influence of buoyancy on the shift of morphology regimes, we consider the free energy of the system. Compared to our previous paper [21], we consider not only the interfacial energy but also a gravitational

energy contribution (see Section 6.2.5). For the symmetry-broken shapes observed under the influence of buoyancy, no analytical solution of the energy Equation 1 is known. The equilibrium morphologies and the corresponding droplet energy can be obtained by numerical minimization over all admissible interfacial configurations and for any combination of parameters (θ, $\tilde{L}$, $\tilde{\lambda}$). For a series of capillary lengths (identical to the experimental values $\tilde{\lambda} = \infty$, 33.1, 18.0, and 13.8), we start from either a barrel or clamshell morphology and change the contact angle θ in small steps for a fixed droplet size $\tilde{L}$. As such, we determine the numerical boundaries of local stability $\theta_{c1}(\tilde{\lambda}, \tilde{L})$ and $\theta_{c2}(\tilde{\lambda}, \tilde{L})$, respectively. The experimental data (circles) agree reasonably well with these numerical curves, although in the experiments the barrel-to-clamshell transition can be induced at slightly lower contact angle as shown in Figure 3.

6.4 Discussion

Figure 3 confirms that the critical contact angles θ_{c1} and θ_{c2} for the barrel-to-clamshell and clamshell-to-barrel transition shift to smaller values with decreasing capillary length and that the hysteresis interval $\Delta\theta = \theta_{c1} - \theta_{c2}$ decreases. With buoyancy both stability lines are nonmonotonous; *i.e.*, the maximum values of the transition angles θ_{c1} and θ_{c2} and the hysteresis interval are obtained at a critical droplet size that scales with capillary length (and is infinite for zero buoyancy). For small buoyancy, surface energy favors the clamshell morphology for large θ and small $\tilde{L}$. For larger buoyancy, gravitational energy now also favors the clamshell morphology due to an upward shift of the center of mass of the (low-density) droplet. The stability lines curve backward, making the regimes for stable barrels and bistability finite. Although the regimes of stable barrels and bistability shrink in favor of stable clamshells, we note that in our numerical results we do find for all conditions investigated a region at small contact angles and intermediate droplet volumes, for which barrels are the only mechanically stable morphology. Experimentally, highly buoyant large droplets can occasionally be stuck in the bistable regime if the contact angle needed to destabilize the clamshell is lower than experimentally accessible. Thus, clamshells are always found to become unstable provided that θ is small enough. This finding is in contrast to the report by Chou *et al*. [22].

The morphology diagram is extended with a third stability criterion $\theta_{c3}(\tilde{\lambda}, \tilde{L})$ that indicates the clamshell-to-detached transition. Large clamshells detach from the fiber when the buoyancy force $\sim|\Delta\rho|gL^3$ is dominating the capillary force, the latter scaling with either the fiber (γr_f) or droplet (γL) length in the limit of high and low fiber

curvature, respectively [29]. The typical length scale for detachment then scales with $\tilde{\lambda}^{\alpha}$ with α between 2/3 and 1 and is relatively insensitive to contact angle, as observed in the numerical results presented in Figure 3. The detachment is also experimentally observed as indicated by the star-shaped symbols. The inset of Figure 5 shows a sequence of the clamshell-to-detached transition. After necking, a small clamshell droplet is left behind on the fiber, with the same contact angle as just before the transition.

The energy landscape of the two competing morphologies (constructed by imposing a sequence of fixed $\tilde{x}_{cm}$ for each morphology separately [21]) shows that both the barrel-to-clamshell and the clamshell-to-barrel transitions occur when their respective energy barriers disappear at θ_{c1} and θ_{c2}, respectively. This is still valid if buoyancy plays a role, although some differences in the energy curves are observed. Equation 1 shows that the additional energy contribution due to gravitation can be added a posteriori and is linearly decreasing with $\tilde{x}_{cm}$ (with a slope determined by capillary length and droplet size). In the absence of buoyancy (see Figure 4A), the energy minimum corresponding to the barrel morphology is always found for an axisymmetric configuration, *i.e.*, for $\tilde{x}_{cm} = 0$. The decay of the barrel into the clamshell morphology is characterized by a vanishing second derivative $\mathrm{d}^2\tilde{E}_c/\mathrm{d}\tilde{x}_{cm}{}^2$ in the minimum of the potential: the minimum at $\tilde{x}_{cm} = 0$ transforms into a local maximum while θ is increased. The second derivative $\mathrm{d}^2\tilde{E}_c/\mathrm{d}\tilde{x}_{cm}{}^2$ on the barrel branch decreases as $\tilde{x}_{cm}$ is increased, and the energy curve displays an inflection point where the slope $\mathrm{d}\tilde{E}_c/\mathrm{d}\tilde{x}_{cm}$ has a maximum. This distance of the inflection point on the barrel branch in the absence of buoyancy and the value $\mathrm{d}\tilde{E}_c/\mathrm{d}\tilde{x}_{cm}$ itself become larger as the contact angle decreases (*cf.* Figure 4A).

Now, in the presence of buoyancy, the additional energy term in Equation 1 accounting for buoyancy is linear in $\tilde{x}_{cm}$ and proportional to $k = L^3/\lambda^2$. If the maximum slope in the absence of buoyancy satisfies $\left(\mathrm{d}\tilde{E}_c/\mathrm{d}\tilde{x}_{cm}\right)_{max} > k$, the barrel is still locally stable, but its symmetry is broken and the corresponding energy minimum is shifted toward finite $\tilde{x}_{cm} > 0$ (see Figure 4B, indicated by circles). With growing contact angles the minimum is shifted to larger distances $\tilde{x}_{cm}$, which is noted in Figure 2A, B by the increase of barrel asymmetry with growing contact angle. To describe and classify the instability of the barrel upon increasing buoyancy, we have to consider two possible soft modes: the first mode is related to the radial displacement of the center of mass and is characterized by a vanishing second derivative of the restricted energy. It occurs once the magnitude of buoyancy is so large that $\left(\mathrm{d}\tilde{E}_c/\mathrm{d}\tilde{x}_{cm}\right)_{max} = k$ is satisfied; *i.e.*, the minimum of the sum of restricted and gravitational energy has reached the inflection point and transformed into a

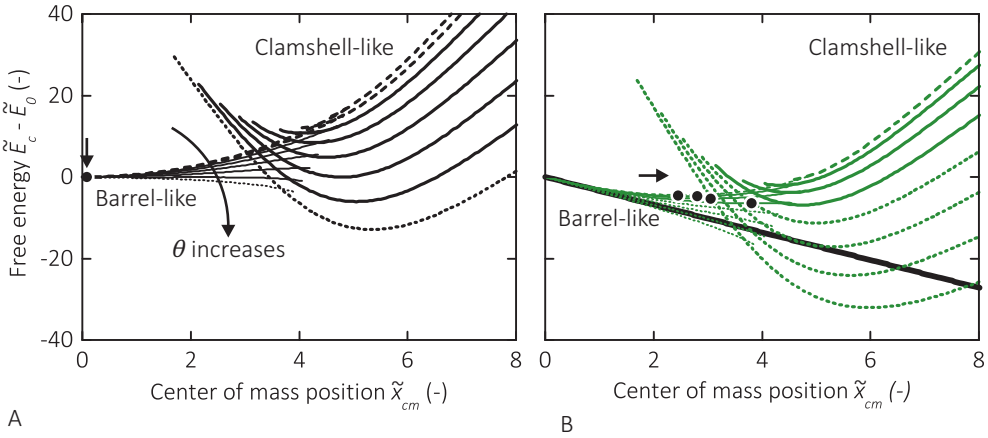

Figure 4 Restricted interfacial free energy $\tilde{E}_c - \tilde{E}_0$ (with $\tilde{E}_0$ the normalized energy of the axisymmetric barrel) of barrel-like (thin lines) and clamshell-like (thick lines) morphologies for (A) infinite capillary length and (B) $\tilde{\lambda} = 18.0$. The energy is plotted versus radial position of the center of mass $\tilde{x}_{cm}$ for various contact angles (10°, ..., 80°) at fixed $\tilde{L} = 10.3$. The upper dashed and lower dotted curves denote stable barrel and clamshell equilibrium morphologies, respectively, whereas for the middle solid curves both morphologies are mechanically stable. The circles (denoted with arrow) represent the minimum energy of the barrel morphology, which is located at $\tilde{x}_{cm} = 0$ in (A) and shifted outward in (B). The black solid line in (B) denotes the gravitational energy added to the curves of (A).

saddle point. The second mode is related to the rupture of the liquid neck which forms in the back of the barrel and causes it to decay into a clamshell. In any case, this necking instability marks the terminal point of the barrel branch. At this point we find the droplet to be already unstable with respect to the radial displacement mode, *i.e.*, a second derivative $\mathrm{d}^2\tilde{E}_c/\mathrm{d}\tilde{x}_{cm}{}^2 < 0$, which is in accordance with the prediction of Maddocks [30] on constrained isoperimetric problems. Our numerical results suggest that, while decreasing the contact angle θ, the inflection point approaches the end of the barrel branch, causing the region with negative second derivative to shrink. Eventually, in the limit $\theta \to 0$, the inflection point and the terminal point are identical; *i.e.*, the two instabilities occur simultaneously. Moreover, the region of bistability between barrel and clamshell has shrunken to a point, and the two branches have merged into a single smooth curve.

The transition from a clamshell morphology to a state where the droplet is split into two parts (of which one is completely detached due to the formation and rupture of a neck)

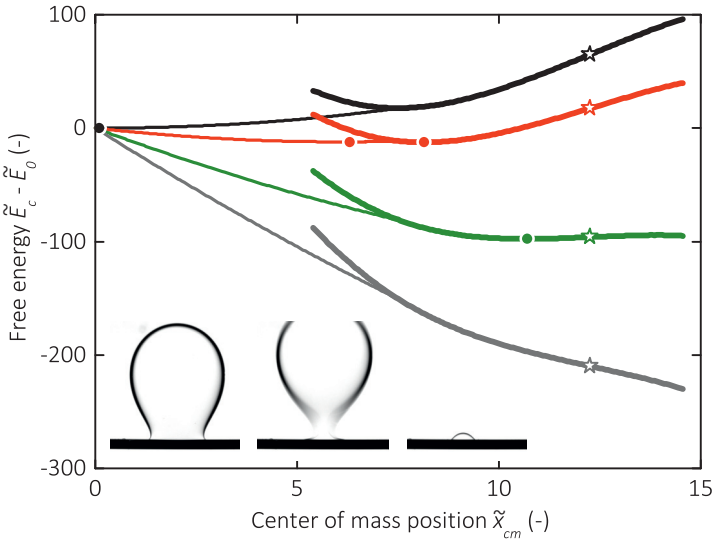

Figure 5 Transition to the detached state. Restricted interfacial free energy $\tilde{E}_c - \tilde{E}_0$ versus $\tilde{x}_{cm}$ of barrel-like (thin line) and clamshell-like (thick line) morphologies for $\tilde{L} = 16.2$ and θ = 47° (corresponding to the green star in Figure 3). The four different colors indicate four different reduced capillary lengths: $\tilde{\lambda} = \infty$ (black), 33.1 (red), 18.0 (green), and 13.8 (gray). The local minima in the barrel and clamshell curves are indicated by dots, while the inflection point in the clamshell curve is indicated by a star. The droplet is detached from the fiber when the local minimum in the clamshell energy vanishes – close to $\tilde{\lambda} = 18.0$ – and the lower energy of the detached state can be assumed. The inset shows a side view sequence of the clamshell-to-detached transition at constant contact angle.

can be explained by exactly the same mechanism as described above for the barrel-to-clamshell transition: also, the restricted interfacial energy of the clamshell branches exhibits a negative third derivative with respect to the distance $\tilde{x}_{cm}$ and an inflection point. The main difference is that the maximum slopes of the clamshell branches are much larger, which implies larger buoyancy required to induce droplet detachment. This can be observed in Figure 5 where the effect of increasing buoyancy on a system defined by a specific volume $\tilde{L} = 10.3$ and contact angle $\theta = 47°$ is shown. From upper to the lower curve are displayed: a single stable barrel ($\tilde{\lambda} = \infty$, black curve), bistable asymmetric barrel and clamshell ($\tilde{\lambda} = 33.1$, red curve), a single stable clamshell ($\tilde{\lambda} = 18.0$, green curve), and detachment ($\tilde{\lambda} = 13.8$, gray curve). While decreasing $\tilde{\lambda}$ the local minimum on the clamshell branch moves into the direction of the inflection point. Below a certain value $\tilde{\lambda}$ of the reduced capillary length, the minimum ceases to exist ($\tilde{\lambda} > 18.0$), and the

clamshell droplet decays into the detached state. In terms of absolute stability based on the global energy minimum, any liquid morphology is unstable with respect to a completely or partially detached droplet, as the gravitational energy can be lowered to an arbitrary small value.

In this work we analyzed the morphology and stability of droplets wetting a cylindrical fiber controlled by contact angle, droplet size, and the magnitude of buoyancy forces. Our experimental findings are in good agreement with results of numerical energy minimizations. A systematic analysis of the computed energy landscape for various droplet size and capillary lengths allows us to explain the high sensitivity of the stability limit of the barrel morphology with respect to buoyancy forces observed in experiments. It is demonstrated that, in the range of experimentally accessible contact angles $\theta > 10°$, droplet detachment from a cylindrical fiber occurs always from the clamshell morphology. Similar morphological transitions and the detachment of droplets occur under an incident flow of the ambient phase. It will be interesting to see if the destabilizing hydrodynamic drag force acting on the surface of the droplet can be effectively replaced by a volume force as considered in the present work.

References

[1] N.K. Adam, *Detergent action and its relation to wetting and emulsification*, J. Soc. Dryers Colourists 53 (1937), 121-129.

[2] T. Gilet, D. Terwagne and N. Vandewalle, *Digital microfluidics on a wire*, Appl. Phys. Lett. 95 (2009), 014106.

[3] T. Gilet, D. Terwagne and N. Vandewalle, *Droplets sliding on fibres*, Eur. Phys. J. E 31 (2010), 253-262.

[4] Y.M. Zheng, H. Bai, Z.B. Huang, X.L. Tian, F.Q. Nie, Y. Zhao, J. Zhai and L. Jiang, *Directional water collection on wetted spider silk*, Nature 463 (2010), 640-643.

[5] Z. Huang, Y. Chen, Y. Zheng and L. Jiang, *Capillary adhesion of wetted cribellate spider capture silks for larger pearly hanging-drops*, Soft Matter 7 (2011), 9468-9473.

[6] H. Bai, R. Sun, J. Ju, X. Yao, Y. Zheng and L. Jiang, *Large-scale fabrication of bioinspired fibers for directional water collection*, Small 7 (2011), 3429-3433.

[7] E. Lorenceau and D. Quere, *Drops on a conical wire*, J. Fluid Mech. 510 (2004), 29-45.

[8] M.E.R. Shanahan, *On the behavior of dew drops*, Langmuir 27 (2011), 14919-22.

[9] B.J. Mullins, I.E. Agranovski, R.D. Braddock and C.M. Ho, *Effect of fiber orientation on fiber wetting processes*, J. Colloid Interf. Sci. 269 (2004), 449-458.

[10] Z. Huang, X. Liao, Y. Kang, G. Yin and Y. Yao, *Equilibrium of drops on inclined fibers*, J. Colloid Interf. Sci. 330 (2009), 399-403.

[11] J. Plateau, *Statique experimentale et theorique des liquides soumis aux seules forces moleculaires*, Gauthier-Villars (1873).

[12] A. Klingner and F. Mugele, *Electrowetting-induced morphological transitions of fluid microstructures*, J. Appl. Phys. 95 (2004), 2918-2920.

[13] M. Brinkmann and R. Lipowsky, *Wetting morphologies on substrates with striped surface domains*, J. Appl. Phys. 92 (2002), 4296-4306.

[14] H. Gau, S. Herminghaus, P. Lenz and R. Lipowsky, *Liquid morphologies on structured surfaces: From microchannels to microchips*, Science 283 (1999), 46-49.

[15] M. Callies and D. Quere, *On water repellency*, Soft Matter 1 (2005), 55-61.

[16] G. Manukyan, J.M. Oh, D. Van Den Ende, R.G.H. Lammertink and F. Mugele, *Electrical switching of wetting states on superhydrophobic surfaces: A route towards reversible Cassie-to-Wenzel transitions*, Phys. Rev. Lett. 106 (2011), 014501.

[17] B.J. Carroll, *Accurate measurement of contact-angle, phase contact areas, drop volume, and Laplace excess pressure in drop-on-fiber systems*, J. Colloid Interf. Sci. 57 (1976), 488-495.

[18] B.J. Carroll, *Equilibrium conformations of liquid-drops on thin cylinders under forces of capillarity - a theory for the roll-up process*, Langmuir 2 (1986), 248-250.

[19] G. Mchale, M.I. Newton and B.J. Carroll, *The shape and stability of small liquid drops on fibers*, Oil Gas Sci. Technol. 56 (2001), 47-54.

[20] G. Mchale and M.I. Newton, *Global geometry and the equilibrium shapes of liquid drops on fibers*, Colloid Surf. A 206 (2002), 79-86.

[21] H.B. Eral, J. De Ruiter, R. De Ruiter, J.M. Oh, C. Semprebon, M. Brinkmann and F. Mugele, *Drops on functional fibers: From barrels to clamshells and back*, Soft Matter 7 (2011), 5138-5143.

[22] T.-H. Chou, S.-J. Hong, Y.-E. Liang, H.-K. Tsao and Y.-J. Sheng, *Equilibrium phase diagram of drop-on-fiber: Coexistent states and gravity effect*, Langmuir 27 (2011), 3685-3692.

[23] F. Mugele and J.C. Baret, *Electrowetting: From basics to applications*, J. Phys. Condens. Matter 17 (2005), R705-R774.

[24] H.B. Eral, G. Manukyan and J.M. Oh, *Wetting of a drop on a sphere*, Langmuir 27 (2011), 5340-5346.

[25] J. Buehrle, S. Herminghaus and F. Mugele, *Interface profiles near three-phase contact lines in electric fields*, Phys. Rev. Lett. 91 (2003), 086101.

[26] F. Mugele and J. Buehrle, *Equilibrium drop surface profiles in electric fields*, J. Phys. Condens. Matter 19 (2007), 375112.

[27] G. Mchale, N.A. Kab, M.I. Newton and S.M. Rowan, *Wetting of a high-energy fiber surface*, J. Colloid Interf. Sci. 186 (1997), 453-461.

[28] K.A. Brakke, *The surface evolver and the stability of liquid surfaces*, Phil. Trans. R. Soc. A 354 (1996), 2143-2157.

[29] E. Lorenceau, T. Senden and D. Quéré, *Wetting of Fibers*, in Molecular Gels, edited by R.G. Weiss and P. Terech, Springer Netherlands (2006).

[30] J.H. Maddocks, *Stability and folds*, Arch. Rational Mech. Anal. 99 (1987), 301-328.

Chapter 7

Electrostatic potential wells for on-demand drop manipulation in microchannels

Precise control and manipulation of individual drops are crucial in many lab-on-a-chip applications. We present a novel hybrid concept for channel-based discrete microfluidics with integrated electrowetting functionality by incorporating co-planar electrodes (separated by a narrow gap) in one of the microchannel walls. By combining the high throughput of channel-based microfluidics with the individual drop control achieved using electrical actuation, we acquire the strengths of both worlds. The tunable strength of the electrostatic forces enables a wide range of drop manipulations, such as on-demand trapping and release, guiding, and sorting of drops in the microchannel. In each of these scenarios, the retaining electrostatic force competes with the hydrodynamic drag force. The conditions for trapping can be predicted using a simple model that balances these forces.

This chapter has been published as R. de Ruiter, A.M. Pit, V. Martins de Oliveira, M.H.G. Duits, H.T.M. van den Ende and F. Mugele, *Electrostatic potential wells for on-demand drop manipulation in microchannels*, Lab on a Chip 15 (2014), 883-891.

7.1 Introduction

In various fields in (cell) biology and chemistry, microfluidic drops are currently used as microreactors of picoliter to nanoliter volume with an isolated and controlled content [1, 2]. By injecting the analyte fluid into T-junctions [3, 4] or flow focusing devices [5], or using microchannel step emulsification [6-8], monodispersed liquid drops can be generated up to kHz frequencies in channel-based discrete microfluidics. However, applications such as high-throughput screening of cells and analysis of chemical reactions require in addition high-speed manipulation and individual control over specific drops.

In flow or pressure driven microfluidics, drops are mostly manipulated passively *via* topological modification of the channels, *e.g.*, by using variations in the channel dimensions to modify the hydrodynamic resistance of different paths or capillary valves to modify the pressure required for drop transport. Several drop manipulations have been demonstrated, such as transport, trapping, sorting, merging, and splitting [1, 9-11]. An illustrative example is the trapping of drops in storage wells connected to the main channel, making use of a combination of capillary forces and differences in hydrodynamic resistance. An alternative flow path is present for the continuous phase in the form of bypass channels when the wells are occupied [12, 13]. On the other hand, drops can also be trapped at specific locations in the main channel itself. Small holes have been introduced in the top wall of a wide and thin microchannel to function as anchors. Confined drops that are passing by expand into the hole to decrease their surface area and interfacial energy, generating an anchoring force that can hold the drop against the drag force of the surrounding flow [14, 15]. The merging of subsequent drops has been achieved for example by widening the channel [16] or capturing drops in between rows of pillars [17], and splitting is accomplished in T-junctions or by introducing isolated obstacles in the flow [18-20]. Since these passive manipulations are in general non-selective and not (easily) tunable, precise control over individual drops is limited. For example, a drop trapped in a storage well or by a small geometric defect in the microchannel wall cannot be easily released by changing the trapping force. To remove the drop from the trap, a change in the direction or magnitude of the flow is required [12-15]. Another possible disadvantage is that if arrays of drops are trapped, they will all be released simultaneously. A combination of active methods, *e.g.*, laser forcing [21] or dielectrophoresis [22], is necessary to release single drops.

Precise control over individual drops can be achieved *via* electrowetting-based digital microfluidics (DMF), in which units of nanoliter to microliter volume are actuated using a

series of adjacent electrodes [23-27]. The same types of drop manipulation as described above are then performed *via* switching of individually addressable electrodes that change the local wettability. As the electrodes provide the actuation, no driving flow is used. Devices are either based on a parallel plate set-up, in which drops are sandwiched between a substrate with insulated actuation electrodes and a substrate with ground electrodes, or on co-planar designs, where both the actuation and ground electrodes are patterned on one substrate. Although high actuation speeds can be achieved in DMF, the throughput is always lower than in channel-based microfluidics. In addition, higher throughputs require extensive programming of a large number of electrodes.

Here, we combine the high throughput and low sample volumes used in channel-based microfluidics and the individual drop control achieved using electrical actuation by incorporating insulator-covered electrodes in the walls of microchannels. The isolation of the electrodes from the aqueous drops offers clear advantages over designs in which there is direct contact between electrodes and fluid [28, 29], as it prevents electrochemical reactions that could be detrimental to various (*e.g.*, biological) samples. Electrodes can be positioned at various locations along the channel in several configurations to perform different drop manipulations, thereby fully integrating the two techniques spatially. This approach differs from a previous hybrid design where a co-planar digital microfluidics unit was placed on the front end of a microchannel based continuous flow system [30]. Here, DMF was used to pre-process liquid drops, after which a small fraction was loaded into the channel for single phase chemical separations. The voltages required for the electrical actuation of drops depend on the thickness of the dielectric layer, but they are generally much lower than the kilovolts used in dielectrophoretic (DEP) actuation, where polarizable drops are manipulated with non-uniform electric fields [22, 31-33]. In addition, electrical actuation offers a more direct and local control, allowing for drop trapping above the electrodes inside the main microchannel.

In previous work by our group, the combination of microfluidics and electrowetting (EW) was used to control the size and frequency of drop formation [34, 35]. We now use a different approach; instead of contact angle reduction, we exploit electrostatic potential wells to manipulate drops in a microchannel flow. Several operations can be implemented, such as on-demand trapping and release, which is crucial for the storage of drops that need to be analyzed *in situ* for some time. To create a trapping site we use two co-planar electrodes [36] separated by a narrow gap. A co-planar design allows for easy

fabrication of the microfluidic device, as the (PDMS) channels only need to be connected to a single insulator-covered substrate with both the actuation and ground electrodes. In more complex lab-on-a-chip devices, such co-planar electrodes can be combined with another functional unit in the second substrate. For example, drops with cells can be trapped in specific positions where ligands are patterned in the opposing channel wall, allowing for the analysis of excreted proteins using Surface Plasmon Resonance (SPR) [37] or other techniques.

When a confined conductive drop is positioned above both insulator-covered electrodes, a series of two parallel-plate capacitors is formed, which generates an electrical potential well that tends to keep the drop above the two electrodes. The associated attractive force is proportional to the square of the applied voltage, allowing for a tunable trapping strength [38]. The equilibrium position of the drop (with respect to the trap) is governed by a force balance between the retaining and driving forces. The latter is the hydrodynamic drag force exerted by the continuous phase flow, which is adjustable *via* the flow rate. The trapping and driving forces are thus adjustable independently. In Section 7.3 we discuss the principle and modelling of the electrostatic trap and compare the trapping and driving forces under various experimental conditions. The versatility of our approach for several applications in lab-on-a-chip devices is illustrated in Section 7.4. We demonstrate the guiding and sorting of drops, offering a simple alternative to sorting *via* dielectrophoresis [31, 33] or surface acoustic waves [39].

7.2 Materials and methods

The microchannels were fabricated from polydimethylsiloxane (PDMS, Sylgard 184) using standard soft lithography [40]. Figure 1A gives an overview of the device, which consists of a (tapered) T-junction where aqueous drops are formed and a main channel containing the electrodes. The height of the device is 85 μm, and the width of the main channel is 2.5 mm. Due to the extreme aspect ratio the main channel can be considered as a Hele-Shaw cell [41]. The side inlets are used to control the oil flow rate in the main channel; this allows choosing the oil flow rates for drop formation and drop transport independently.

The bottom substrate is fabricated from indium tin oxide (ITO) coated glass substrates (PGO). Patterned electrodes are obtained *via* photolithography and etching in a solution of 18% HCl, creating gaps that are 10 or 15 μm wide. The substrate is spin coated with PDMS at 4000 rpm for 600 s to obtain an approximately 7 μm thick insulating layer that separates the aqueous drops from the electrode. While other insulating materials are

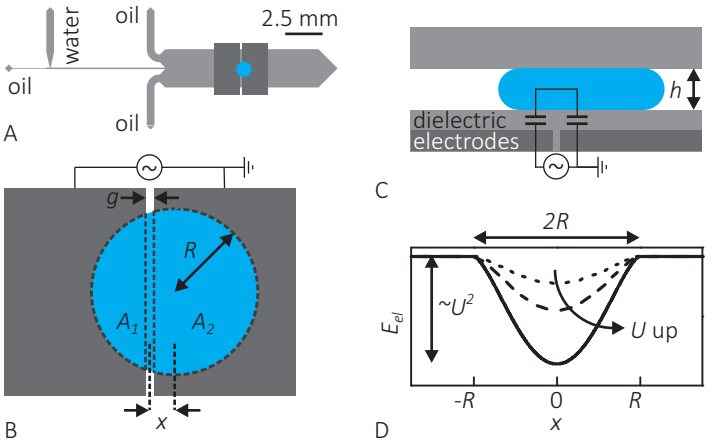

Figure 1 Device geometry and generated electrostatic potential well. (A) Overview of one of the devices showing a drop formation unit and a main channel with trapping electrodes. (B) Top view and (C) side view of the co-planar electrode design. (D) Electrostatic potential well generated by the electrodes.

generally preferable in EW, the use of PDMS was found to provide the most robust devices in terms of channel-to-substrate adhesion and leak-tightness. The PDMS is partly cured (at 75 °C for 20 min) and subsequently connected to the microchannels, while the electrodes are aligned in the main channel. Hereafter, the curing is completed. The properties of the dielectric layer are measured from the electrowetting response, *i.e.*, the voltage-dependent $\cos\theta = \cos\theta_Y + \eta$ on a simultaneously fabricated evenly covered flat substrate. Here, θ_Y is the Young angle, and $\eta = \varepsilon_0\varepsilon_d U^2/(2d\gamma)$ is the electrowetting number [23], where $\varepsilon_0\varepsilon_d$ is the dielectric permittivity of the substrate with thickness d, U is the applied root mean square (RMS) voltage, and γ is the interfacial tension of the oil-water interface. Using this method, the capacitance per area $c = \varepsilon_0\varepsilon_d/d$ of the dielectric layer is determined to be ~2.5 µF/m^2. The effective electrowetting number in the experiments is generally < 1.

Paraffin oil (viscosity $\mu \approx 100$ mPa·s) is used as the continuous phase, and the dispersed phase consists of de-ionized water (Millipore Synergy UV, 18.2 MΩ·cm) with KCl added up to a conductivity of 3 mS/cm (~25 mM). The interfacial tension of the water-oil interface is 50mN/m, and the advancing and receding water contact angles on PDMS are determined to be 148° and 138°, respectively. To study the influence of γ, a mixture of 50 wt% ethylene glycol and 50 wt% water is used. The interfacial tension is reduced to 33 mN/m, and the advancing and receding contact angles are now 148° and 132°.

Continuous oil flows are driven using syringe pumps. The dispersed phase is brought to the tapered T-junction by adjusting the water pressure. The required pressure depends on the applied oil flow rate and the hydraulic resistance of the channels. Drops are subsequently formed on demand by generating short air-pressure pulses using a pressure regulator (Parker Hannifin Corp.), a three-way solenoid valve (Takasago Electric Inc.), and a solid state relay (International Rectifier) which are controlled using home-made circuitry, a data acquisition card (National Instruments), and a custom-written MATLAB program. The air pressure can be regulated from about 1-100 kPa. Drops of different size (R = 50-250 μm) are generated by varying the duration Δt and magnitude ΔP of the pressure pulse. An alternating (AC) voltage (frequency: 1 kHz, RMS voltage: 0-350 V) is applied between the two separated electrodes in the main channel to generate electrostatic forces on the drops. The device is observed using an inverted microscope (TI-U, Nikon), and the behavior of the generated drops is recorded using a high speed camera (FASTCAM SA5, Photron). Drop sizes are extracted using edge detection in MATLAB.

7.3 Principles of on-demand trapping and release

7.3.1 Electrostatic potential wells

We first discuss the potential wells as generated by two co-planar electrodes separated by a gap. This case has already been described by 't Mannetje *et al.* [38] for spherical-cap shaped drops resting on an open surface. In our case, the drops are confined between the bottom and top walls of a microchannel, where the radii of the drops in the horizontal plane are larger than the height of the channel ($R > h$). Nevertheless, the underlying physical principles are the same for these two traps.

Briefly, when a confined drop of an electrically conductive liquid 'touches' (*i.e.*, capacitive couples to) both electrodes, an electrical circuit containing two parallel plate capacitors in series is formed (Figure 1C). For the salt concentrations and AC frequencies considered in our experiments, the liquid can be considered as a perfect conductor (*i.e.*, surface charges completely screen the electric field from the interior of the drop) [42]. The capacitance between the drop and the electrodes is completely dominated by the area of the drop–substrate interface with negligible contributions from the contact line. Restricting our analysis to confined water drops with $R > h$, the contribution of oil intervening between the drop and the solid wall is reduced to a thin film that is negligible compared to the much thicker dielectric layers [43]. We note, however, that our device is also capable of

trapping drops with $R > h$ – albeit with somewhat reduced trapping forces as compared to the analysis presented below.

The overall capacitance is $C(x) = C_1(x)C_2(x)/\big(C_1(x) + C_2(x)\big)$, where the individual capacitances are given by $C_{1,2}(x) = (\varepsilon_0\varepsilon_d/d)A_{1,2}(x)$. Here, $A_{1,2}(x)$ is the area of the squeezed drop above the respective electrode. The areas depend on the position x of the center of mass of the drop (see Figure 1B). Charging the capacitors by applying a voltage generates an electrostatic free-energy landscape $E_{el}(x) = -C(x)U^2/2 = -cAU^2 f(x)$, where $A = \pi R^2$ is the total contact area of the drop. The dimensionless function $f(x)$ can be derived from geometry and accounts for the variations in the areas (two examples are shown using the red curves in Figure 2). The corresponding trapping force $F_{el}(x) = -\mathrm{d}E_{el}(x)/\mathrm{d}x$ has a maximum value $F_{el,max} = -acRU^2$. We thus find that the maximum trapping force scales with the capacitance per area, the radius of the (squeezed) drop, and the square of the voltage, with a proportionality constant a of order unity that depends on the electrode configuration. In this simplified analysis the voltage-dependent contact angle change and the resulting changes in the drop shape are neglected. Estimates show an increase in $F_{el,max}$ of maximum 20% for most experiments.

We now consider specific cases. For a gap between two (effectively) infinite electrodes (Figure 2A), the electrostatic energy is minimal when the drop is centered above the gap. For a negligible gap width ($g \ll R$), the trapping force reaches a maximum $F_{el,max} = -0.58cRU^2$ at $x/R \approx 0.67$. In a microchannel with the gap oriented perpendicular to the flow direction, the hydrodynamic forces will tend to push the drop through the potential well, leading to a counteracting force in the downstream half of the potential and the possibility of drop trapping between $x/R = 0$ and $x/R \approx 0.67$. If the drag force exceeds the maximum value of the electrostatic force, the drop will pass the trap. In case the gap runs parallel to the flow direction in between two finite electrodes (Figure 2B), the hydrodynamic forces will push the drop towards the edge of the electrodes. The areas of the drop above each electrode (always equal due to energy minimization) decrease as the drop is passing the trap. The electrostatic energy is now minimum if the drop is still completely in contact with the electrodes, and increases continuously afterwards. The trapping force reaches its maximum $F_{el,max} = -(1/4)\,cRU^2$ at $x/R = 0$, *i.e.*, when the drop is halfway down the edge of the electrodes (note that this maximum force is 57% lower as compared to the perpendicular gap).

Figure 2C shows drops that are trapped using these two configurations (perpendicular (left) and parallel gaps (middle)) and a V-shaped gap (right). The choice of electrode

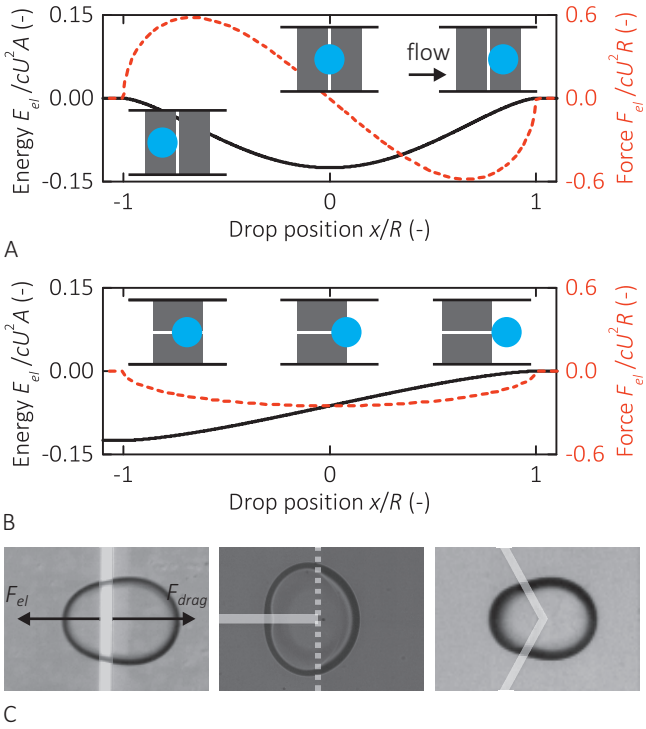

Figure 2 Drop trapping in electrostatic potential wells. (A, B) The electrostatic contribution to the free energy of the system (black solid line) and the resulting electrostatic force (red dashed line) for two co-planar electrodes separated by a narrow gap ($g \rightarrow 0$) (A) perpendicular and (B) parallel to the direction of the flow. (C) Examples of drop trapping in various co-planar electrode designs: perpendicular gap, parallel gap, and V-shaped gap. The gaps between the electrodes are indicated in white.

configuration should be made in relation to the desired application. While the perpendicular gap yields the largest trapping force, the drops are free to move along the gap after trapping. In contrast, the parallel gap has a smaller trapping strength but has the benefits of keeping the drops on a predefined track in the microchannel and confining the trapped drop to a specific position. In addition, the inherent voltage-dependent elongation of the drop perpendicular to the gap (to be discussed in Section 7.4.3) is smaller in the parallel gap. The V-shaped gap directs the drop to the middle of the trap upon trapping. To facilitate the experiments and quantitative modelling of the forces acting on trapped drops, we chose the parallel gap for the present study.

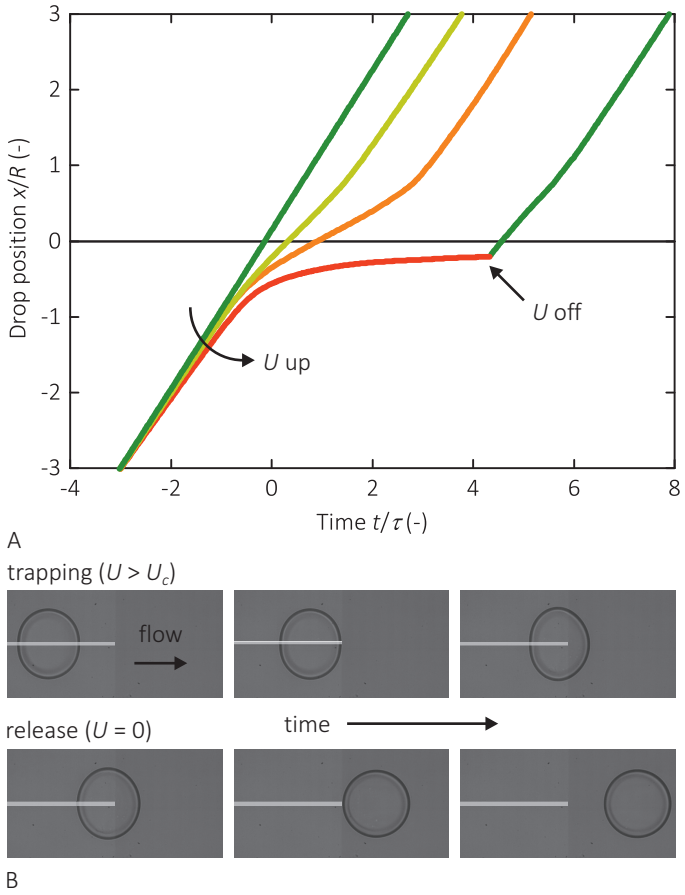

Figure 3 Drop trajectories during trapping and release. (A) Drop trajectories upon passing the co-planar electrode configuration. The time is rescaled with τ, the characteristic time in which the undisturbed drop traverses its radius. For $U = 0$, (green) the drop has a constant velocity, for $0 < U < U_c$ (100 V (yellow) and 140 V (orange)), the drop is slowed down at the trap, and for $U \geq U_c$ (180 V (red)), the drop is ultimately trapped. Trapped drops can be released on demand by switching off the voltage. (B) Image sequences showing on demand drop trapping and release. The gaps between the electrodes are indicated in white.

7.3.2 Trapping experiments

To examine the trapping capability of our split-electrode configuration, we formed drops of a specific size ($R = 150$ µm) and recorded videos at several voltages. The extracted drop trajectories are shown in Figure 3A. All drops have the same initial velocity of 0.3 mm/s, which is slightly lower than the average velocity of 0.8 mm/s of the continuous

phase. As expected, when no voltage is applied, the drop traverses the microchannel without changing its velocity. At low voltages, the drop decelerates as soon as it starts crossing the edge of the electrodes, *i.e.*, at $x/R = -1$. However, as long as the drag force exceeds the maximum electrostatic force, the drop passes the trap and accelerates back to its initial velocity. Trapping of the drop only occurs when the RMS voltage exceeds a critical value U_c. The drop is slowed down until a zero velocity is attained at a voltage-dependent trapping position $x/R < 0$ and can subsequently be released on demand by switching off the voltage. A further increase in the voltage shifts the trapping position upstream (results not shown).

To investigate how this critical voltage U_c depends on the size of the drops, we performed systematic experiments that involved varying the drop size ($R =$ 50-250 μm) and the applied voltage ($U =$ 100-350 V) independently and recording the fate (*i.e.*, passing or trapping) of each drop. The flow rate of the continuous phase in the test section with the trap was held constant. The results shown in Figure 4A clearly indicate that U_c increases with R. Since the electrostatic force is proportional to the drop radius, it is implied that the hydrodynamic 'release force' increases more strongly with R. This also means that the trap is size-selective; for each given voltage we find a critical drop radius R_c above which the drop cannot be trapped anymore. Extending the systematic measurements to a second flow rate, we found that the critical voltage increases with the continuous phase velocity u. Next, drops of a fixed size were formed at several flow rates to explore this dependence in more detail. As shown in Figure 4B, a linear relationship is found between the square of the critical voltage (and thus the maximum electrostatic force) and the continuous phase velocity. Repeating these experiments at a different oil-water interfacial tension (by using an ethylene glycol-water mixture instead of water), we found that the critical voltage does not depend on γ at small applied voltages. At larger voltages, small deviations from this behavior are observed. Low interfacial tension drops are more deformed (see inset) and have a larger voltage-dependent contact angle reduction during guiding and trapping, resulting in a larger maximum trapping force.

7.3.3 Quantitative analysis

To explain the dependence of the critical voltage on drop size and flow rate (but not on interfacial tension), we consider the balance between the maximum electrostatic trapping force and the hydrodynamic driving force on the drop in a quantitative way. More accurate values for the trapping force are obtained by taking into account the finite gap

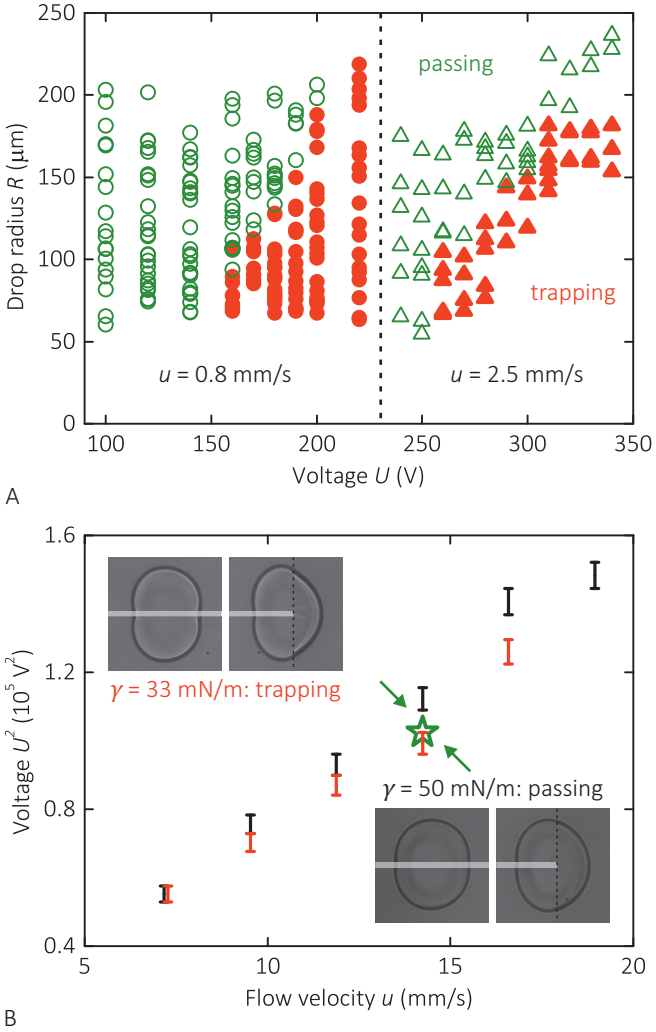

Figure 4 Experimental trapping diagrams. (A) Depending on the applied voltage and drop radius, drops are either being trapped by (red closed symbols) or passing (green open symbols) the electrodes. Results are shown for two different velocities of the continuous phase, $u = 0.8$ mm/s (circles) and $u = 2.5$ mm/s (squares). (B) Square of the critical voltage versus the flow velocity of the continuous phase for a fixed drop size ($R = 125$ µm), for two different interfacial tensions, $\gamma = 50$ mN/m (black) and $\gamma = 33$ mN/m (red). The ends of the error bars indicate the minimum and maximum voltages for which we observed trapping and passing, respectively. The pictures show drops with $\gamma = 50$ mN/m (lower right, passing the electrodes) and $\gamma = 33$ mN/m (upper left, being trapped by the electrodes) at $u = 14.2$ mm/s and $U = 320$ V (as indicated by the star), just before and above the electrode edge. The gaps between the electrodes are indicated in white.

width between the electrodes. A gap width g introduces a correction factor of $(1 - g/2R)$ to the trapping force, which is > 0.85 for gaps that are 10-15 µm wide and drop radii that are larger than 50 µm. Edge detection yields the maximum drop radius, which is converted into the contact radius by taking into account the voltage-dependent contact angle (yielding $<$ 20% corrections). Drop deformations during trapping are neglected. The hydrodynamic drag force exerted by the outer flow is obtained from the Stokes equation. When $h \ll R$ the microchannel can be modelled as a Hele-Shaw cell, where the problem is reduced to a 2D flow by averaging the velocity field over the height of the channel. The total drag force on the drop contains two contributions: the pressure difference along the drop and the viscous shear stresses in the surrounding fluid. Scaling arguments yield expressions for the pressure drag and viscous drag as $F_p \propto \mu u R^2/h$ and $F_\mu \propto \mu u R$, respectively [15]. This indicates that the pressure drag is larger than the viscous drag by an order of $R/h > 1$. An analytical calculation of the drag force on a cylinder with no-slip boundary condition in an infinitely wide channel yields $F_{drag} = (24\pi\mu u R^2/h)\left(1 + 2K_1(q)/\left(qK_0(q)\right)\right)$, where K_0 and K_1 are modified Bessel functions of the second kind and $q = 2\sqrt{3}R/h$ (see Appendix 7A.1). These results agree well with the ones obtained by Lee and Fung [44]. For $R \gg h$, this expression is reduced to $F_{drag} = 24\pi\mu u R^2/h$, which confirms the dominance of the pressure drag in the limit of large drops, while for $R \approx h$ the viscous drag needs to be considered as well (see Figure A1). It should be noted that the drag force is underestimated when the drop size becomes of the order of the finite channel width. The flow velocity is increased as the drop blocks a significant fraction of the channel width. In addition, the no-slip boundary condition at the confining side walls has to be taken into account. Thus, the width of the microchannel is the third length scale in the equation aside from the drop radius and the channel height. The numerically calculated curves in Figure A1B clearly demonstrate that the pressure difference along the drop shows a drastic increase as the drop radius approaches the width of the channel (*i.e.*, $2R/h \approx W/h$), resulting in a diverging drag force. More details about these calculations can be found in Appendix 7A.2 and in the study of Vanapalli *et al.* [45]. Since $R/h < 3$ in the current experiments, the analytical expression is used to determine the drag force.

Plotting the drag force against the maximum trapping force in Figure 5, we find a sharp transition from passing to trapping as soon as the maximum trapping force exceeds the hydrodynamic drag. The experimental data for several flow rates and interfacial tensions follow the same curve, confirming the proposed model. Quantitative deviations should actually be expected for small drops ($R \approx h$), where our assumption of a disc-like drop

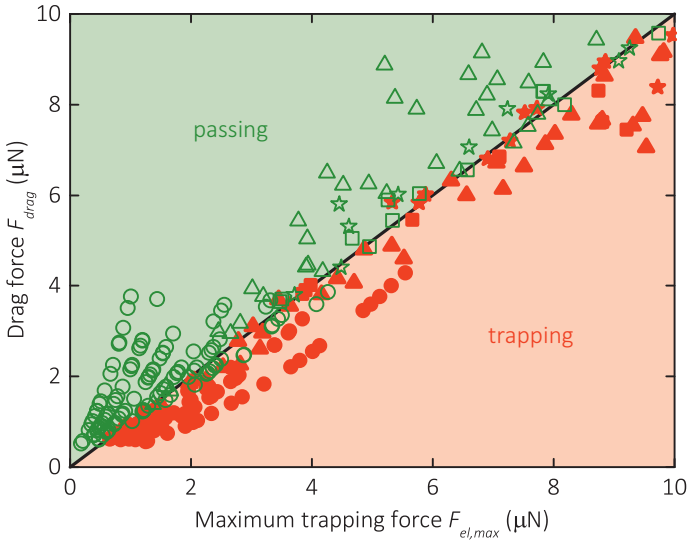

Figure 5 Drag force versus maximum trapping force for the experimental results in Figure 4A ($u = 0.8$ mm/s (circles), $u = 2.5$ mm/s (triangles); $\gamma = 50$ mN/m) and Figure 4B ($\gamma = 50$ mN/m (squares), $\gamma = 33$ mN/m (stars); $R = 125$ μm). The transition from passing (green open symbols) to trapping (red closed symbols) occurs when both forces are equal.

shape breaks down, affecting both the electrostatic trapping force as well as the drag force. Similarly, deviations from a circular shape for large drops ($R \gg h$) or small interfacial tensions (see Figure 4B) are not taken into account in our model. Yet, as Figure 5 shows, the consequences for the prediction of the trapping threshold are minor for the range of parameters studied here, *i.e.*, in particular for electrostatic trapping forces up to 10 μN. Note that these forces are one to two orders of magnitude larger than the forces of 0.1 to 1 μN reported for geometric traps [15]. Moreover, electrostatic traps offer the additional advantage of being switchable, enabling on-demand trapping and release of drops by changing the applied voltage.

7.4 Applications

7.4.1 Guiding of drops

The principle that the electrostatic force will pull a drop towards the middle of a gap can also be used to direct drops. An example hereof is presented in Figure 6. By placing the electrode gap at an angle α with respect to the flow direction, the electrostatic trapping force competes with the projection of the hydrodynamic driving force in the direction

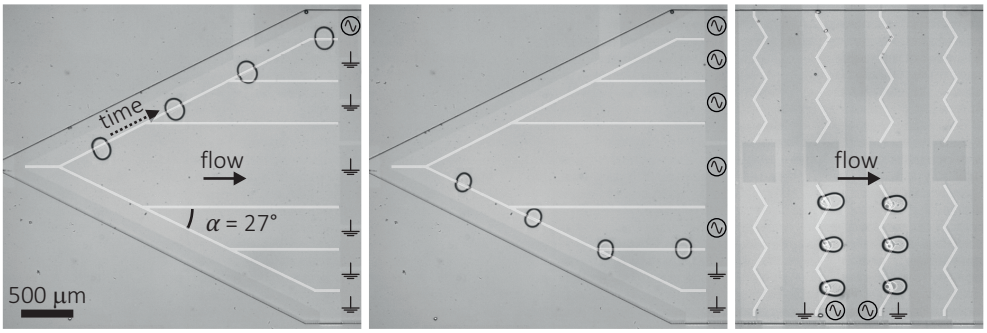

Figure 6 Guiding and trapping of drops. (A, B) Guiding of drops along various tracks in a microchannel using a series of individually addressable electrodes. These pictures are made by combining four time frames. (C) Downstream trapping of multiple drops. The gaps between the electrodes are indicated in white.

perpendicular to the gap. In terms of a simple force balance between the trapping and the driving force, this means that we can use the equations for a perpendicular gap, in which, however, the ratio between the hydrodynamic force and the maximum electrostatic force is now decreased by a factor of $\sin\alpha$. This allows for the guiding of drops even in strong flows, by designing a small value for α. By combining several electrodes in a branching geometry, drops can be guided laterally along various predefined tracks, depending on which electrodes are activated. Only $n+1$ electrodes are needed to obtain n possible directions. The path of subsequent drops can be easily altered by switching between the electrodes, which offers increased flexibility as compared to guiding along topological rails [14]. After the drops are guided along different parallel tracks, they can be stopped using an independently operated array of electrostatic trapping wells located at the terminus of the guiding gaps. This combination of guiding and trapping is very suitable in scenarios where several drops have to be chemically treated or analyzed in parallel for a certain amount of time; an example is the analysis of biomolecules in drops using local sensor surfaces (as *e.g.*, in SPR [14]).

7.4.2 High-speed drop sorting

The guiding of drops as shown in the previous section has an intrinsic speed limitation. At higher flow speeds, drops are unable to follow the guide due to the drag force. To reduce the relevant component of the drag force, a smaller inclination angle is required, which results in longer tracks for reaching a certain lateral displacement. In lab-on-a-chip

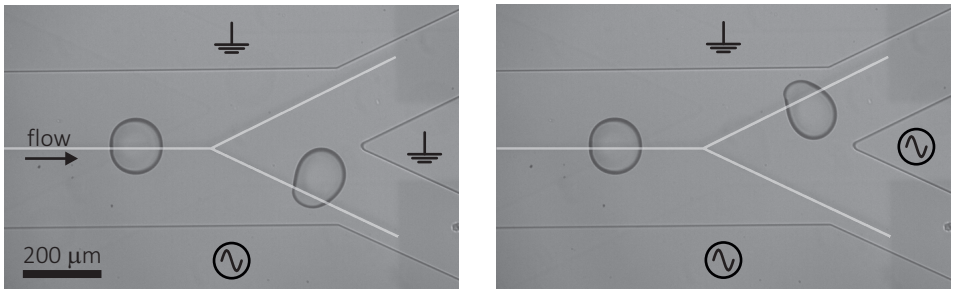

Figure 7 Top view of a three-electrode high speed sorting geometry below a Y-shaped channel. Drops are continuously generated using a flow focusing device. By switching the middle electrode (A) on and (B) off, a drop can be forced towards either outlet. The angle of the gaps and Y-junction with respect to the inlet channel is 25°. The gaps between the electrodes are indicated in white.

applications that involve sorting rather than slow analysis, for instance, selecting between empty and cell-containing drops or between fluorescently labelled and non-labelled drops, higher handling speeds are desirable, which can be achieved by optimizing the electrode and channel design. To this end, we designed a three-electrode branching geometry underneath a Y-shaped channel (height 55 µm, width 400 µm) as shown in Figure 7. An AC potential difference is applied continuously across the upper and lower electrodes, while the middle electrode is switched between the applied potential and ground electrode, effectively switching the path of the drop from one outlet to the other. Drops approach the Y-junction exactly in the middle of the channel and only require a small deflection to be directed to either outlet.

In this experiment, we generated water drops in mineral oil ($\mu \approx 30$ mPa·s) using a flow focusing device. Depending on the flow rates of the water and oil phase, confined drops can be generated at 10 to 1000 Hz. To avoid hydrodynamic interactions, the distance between subsequent drops can be increased by increasing the oil flow rate. The maximum electrostatic force is exerted when the center of the drop is at a distance of $\sim 0.67R$ from the gap (see Section 7.3.1). The optimum design for deflecting drops that flow at a high speed (and hence experience large hydrodynamic forces) requires that the gaps are not centered below the outlet channels, but rather are offset towards the outer walls. With the gaps incorporated in this way, we observe that the drops end up approximately in the centers of the outlet channels. The applied potential is a 10 kHz sine wave at 225 V. For the middle electrode, the sine is modulated by a square waveform. When the middle

electrode is at 0 V, drops are directed to the lower channel, and when it is at 255 V, drops are directed to the upper channel. Modulating the middle electrode at half the frequency of drop generation allows alternate sorting of drops. It is also possible to select a single drop from a train of drops by applying a short pulse lasting one period of drop generation. In combination with a detection technique, *e.g.*, optical or electrical [46], our device could be used as an active sorter.

With the current device and materials used, we were able to sort 100 drops per second. At higher drop generation rates, the drag force becomes too large for the electrostatic force to pull the drop towards the desired outlet. However, the geometry of the channel and the electrodes could be optimized to achieve higher sorting rates. Since the drag scales linearly with the viscosity of the continuous phase, the drag could be reduced (and hence the sorting frequency is increased) by using oils with a lower viscosity. Another option is to decrease the inclination angle of the branching electrodes.

Electrostatic potential wells and dielectrophoresis (DEP) [31, 33] both make use of electric fields for drop sorting. DEP comprises the motion of liquid drops, particles, or biological cells in a non-uniform electric field and relies on differences in the (frequency-dependent) dielectric constant with the continuous phase. Obtaining the force for the actual device geometry thus requires calculation of the electric field gradients. In addition, sorting cell-containing drops from empty drops in ambient oil involves the use of physiological strength buffers with a relatively large conductivity, *i.e.*, typically 15 mS/cm. Manipulation using DEP requires a frequency of hundreds of MHz in this case [47, 48]. In contrast, manipulation using electrostatic potential wells relies on the sharp contrast between conductive drops in an insulating medium. Our method is thus especially suitable for this application, while using lower frequencies and voltages as compared to DEP.

7.4.3 Drop deformations and splitting

The aforementioned drop deformations can be explained *via* minimization of the sum of the electrostatic and interfacial energies. As the drop deforms perpendicular to the gap, the total area above the electrodes increases at the cost of the area above the gap. Thus, the presence of a gap is critical to these deformations. The resulting decrease in electrostatic energy is balanced by the increase in interfacial energy associated with the increase in surface area. Minimizing the total energy then yields an equilibrium shape that is dependent on the applied voltage. This reasoning predicts larger drop deformations for wider gaps, larger drops, higher voltages, and lower interfacial tension. These trends are

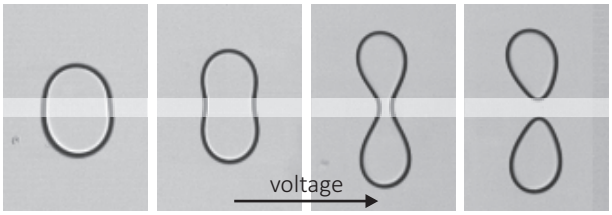

Figure 8 Splitting of drops at high voltage and large gap width. The gap between the electrodes is indicated in white.

confirmed in the experiments. We chose narrow gap widths (*i.e.*, 10 or 15 μm) and a high interfacial tension (*i.e.*, no surfactants) for the purpose of limiting deformations.

Extreme drop deformations result in the splitting of drops as shown for high voltages in Figure 8 and in the trapping diagram in Figure A2A. So while our simple force-based model would imply no limitations on the applied voltage and the absence of a role for the interfacial tension, it is the splitting of drops that limits the voltage that can be applied and thus the maximum electrostatic trapping force that can be exerted. In situations in which larger trapping forces are required or drops are sensitive to break-up (*e.g.*, when surfactants are used that lower the interfacial tension), the use of electrodes in a parallel plate set-up could be considered. Here, the actuation electrodes are patterned on one substrate, while the ground electrode is on the other, which eliminates the presence of a gap. This approach can be used for both trapping and guiding of drops in channels. Although a restriction in the possibilities for drop trapping, the drop splitting itself offers another interesting drop manipulation in microchannels due to its symmetry. The original drop centers above the electrode gap due to energy minimization, and thus always splits into two equally-sized drops.

7.5 Conclusions

We presented a hybrid concept for channel-based microfluidics with integrated electrowetting functionality to achieve individual control over nanoliter aqueous drops at high throughput. The trapping of drops using a co-planar electrode configuration is successfully predicted using a simple model that balances the maximum electrostatic force exerted by the trap with the hydrodynamic drag force exerted by the surrounding flow. Compared to small geometric defects, the maximum forces are an order of magnitude larger and tunable. In addition, we showed guiding and high-speed sorting of

drops. We anticipate that this hybrid technology platform will enable further flexible devices combining high throughput and individual drop control.

References

[1] H. Song, D.L. Chen and R.F. Ismagilov, *Reactions in droplets in microflulidic channels*, Angew. Chem. Int. Edit. 45 (2006), 7336-7356.

[2] M.T. Guo, A. Rotem, J.A. Heyman and D.A. Weitz, *Droplet microfluidics for high-throughput biological assays*, Lab Chip 12 (2012), 2146-2155.

[3] P. Garstecki, M.J. Fuerstman, H.A. Stone and G.M. Whitesides, *Formation of droplets and bubbles in a microfluidic T-junction - scaling and mechanism of break-up*, Lab Chip 6 (2006), 437-446.

[4] T. Thorsen, R.W. Roberts, F.H. Arnold and S.R. Quake, *Dynamic pattern formation in a vesicle-generating microfluidic device*, Phys. Rev. Lett. 86 (2001), 4163-4166.

[5] S.L. Anna, N. Bontoux and H.A. Stone, *Formation of dispersions using "flow focusing" in microchannels*, Appl. Phys. Lett. 82 (2003), 364-366.

[6] S. Sugiura, M. Nakajima, S. Iwamoto and M. Seki, *Interfacial tension driven monodispersed droplet formation from microfabricated channel array*, Langmuir 17 (2001), 5562-5566.

[7] K. Van Dijke, G. Veldhuis, K. Schroen and R. Boom, *Parallelized edge-based droplet generation (EDGE) devices*, Lab Chip 9 (2009), 2824-2830.

[8] K. Van Dijke, R. De Ruiter, K. Schroen and R. Boom, *The mechanism of droplet formation in microfluidic EDGE systems*, Soft Matter 6 (2010), 321-330.

[9] C.N. Baroud, F. Gallaire and R. Dangla, *Dynamics of microfluidic droplets*, Lab Chip 10 (2010), 2032-2045.

[10] R. Seemann, M. Brinkmann, T. Pfohl and S. Herminghaus, *Droplet based microfluidics*, Rep. Progr. Phys. 75 (2012), 016601.

[11] H. Gu, M.H.G. Duits and F. Mugele, *Droplets formation and merging in two-phase flow microfluidics*, Int. J. Mol. Sci. 12 (2011), 2572-2597.

[12] H. Boukellal, S. Selimovic, Y.W. Jia, G. Cristobal and S. Fraden, *Simple, robust storage of drops and fluids in a microfluidic device*, Lab Chip 9 (2009), 331-338.

[13] M. Sun, S.S. Bithi and S.A. Vanapalli, *Microfluidic static droplet arrays with tuneable gradients in material composition*, Lab Chip 11 (2011), 3949-3952.

[14] P. Abbyad, R. Dangla, A. Alexandrou and C.N. Baroud, *Rails and anchors: guiding and trapping droplet microreactors in two dimensions*, Lab Chip 11 (2011), 813-821.

[15] R. Dangla, S. Lee and C.N. Baroud, *Trapping microfluidic drops in wells of surface energy*, Phys. Rev. Lett. 107 (2011).

[16] Y.-C. Tan, Y.L. Ho and A.P. Lee, *Droplet coalescence by geometrically mediated flow in microfluidic channels*, Microfluid. Nanofluid. 3 (2007), 495-499.

[17] X. Niu, S. Gulati, J.B. Edel and A.J. Demello, *Pillar-induced droplet merging in microfluidic circuits*, Lab Chip 8 (2008), 1837-1841.

[18] D.R. Link, S.L. Anna, D.A. Weitz and H.A. Stone, *Geometrically mediated breakup of drops in microfluidic devices*, Phys. Rev. Lett. 92 (2004), 054503.

[19] L. Salkin, A. Schmit, L. Courbin and P. Panizza, *Passive breakups of isolated drops and one-dimensional assemblies of drops in microfluidic geometries: experiments and models*, Lab Chip 13 (2013), 3022-3032.

[20] S. Protiere, M.Z. Bazant, D.A. Weitz and H.A. Stone, *Droplet breakup in flow past an obstacle: A capillary instability due to permeability variations*, Europhys. Lett. 92 (2010).

[21] E. Fradet, C. Mcdougall, P. Abbyad, R. Dangla, D. Mcgloin and C.N. Baroud, *Combining rails and anchors with laser forcing for selective manipulation within 2D droplet arrays*, Lab Chip 11 (2011), 4228-4234.

[22] W. Wang, C. Yang, Y.S. Liu and C.M. Li, *On-demand droplet release for droplet-based microfluidic system*, Lab Chip 10 (2010), 559-562.

[23] F. Mugele and J.C. Baret, *Electrowetting: From basics to applications*, J. Phys. Condens. Matter 17 (2005), R705-R774.

[24] R.B. Fair, *Digital microfluidics: is a true lab-on-a-chip possible?*, Microfluid. Nanofluid. 3 (2007), 245-281.

[25] M.G. Pollack, R.B. Fair and A.D. Shenderov, *Electrowetting-based actuation of liquid droplets for microfluidic applications*, Appl. Phys. Lett. 77 (2000), 1725-1726.

[26] S.K. Cho, H.J. Moon and C.J. Kim, *Creating, transporting, cutting, and merging liquid droplets by electrowetting-based actuation for digital microfluidic circuits*, J. Microelectromech. Syst. 12 (2003), 70-80.

[27] M.J. Jebrail, M.S. Bartsch and K.D. Patel, *Digital microfluidics: a versatile tool for applications in chemistry, biology and medicine*, Lab Chip 12 (2012), 2452-2463.

[28] M. Zagnoni and J.M. Cooper, *On-chip electrocoalescence of microdroplets as a function of voltage, frequency and droplet size*, Lab Chip 9 (2009), 2652-2658.

[29] C. Priest, S. Herminghaus and R. Seemann, *Controlled electrocoalescence in microfluidics: Targeting a single lamella*, Appl. Phys. Lett. 89 (2006).

[30] M. Abdelgawad, M.W.L. Watson and A.R. Wheeler, *Hybrid microfluidics: A digital-to-channel interface for in-line sample processing and chemical separations*, Lab Chip 9 (2009), 1046-1051.

[31] K. Ahn, C. Kerbage, T.P. Hunt, R.M. Westervelt, D.R. Link and D.A. Weitz, *Dielectrophoretic manipulation of drops for high-speed microfluidic sorting devices*, Appl. Phys. Lett. 88 (2006).

[32] W. Wang, C. Yang and C.M. Li, *On-demand microfluidic droplet trapping and fusion for on-chip static droplet assays*, Lab Chip 9 (2009), 1504-1506.

[33] J.C. Baret, O.J. Miller, V. Taly, M. Ryckelynck, A. El-Harrak, L. Frenz, C. Rick, M.L. Samuels, J.B. Hutchison, J.J. Agresti, D.R. Link, D.A. Weitz and A.D. Griffiths, *Fluorescence-activated droplet sorting (FADS): Efficient microfluidic cell sorting based on enzymatic activity*, Lab Chip 9 (2009), 1850-1858.

[34] F. Malloggi, S.A. Vanapalli, H. Gu, D. Van Den Ende and F. Mugele, *Electrowetting-controlled droplet generation in a microfluidic flow-focusing device*, J. Phys. Condens. Matter 19 (2007).

[35] H. Gu, F. Malloggi, S.A. Vanapalli and F. Mugele, *Electrowetting-enhanced microfluidic device for drop generation*, Appl. Phys. Lett. 93 (2008).

[36] U.C. Yi and C.J. Kim, *Characterization of electrowetting actuation on addressable single-side coplanar electrodes*, J. Micromech. Microeng. 16 (2006), 2053-2059.

[37] L. Malic, T. Veres and M. Tabrizian, *Nanostructured digital microfluidics for enhanced surface plasmon resonance imaging*, Biosens. Bioelectron. 26 (2011), 2053-2059.

[38] D.J.C.M. 'T Mannetje, A.G. Banpurkar, H. Koppelman, M.H.G. Duits, D. Van Den Ende and F. Mugele, *Electrically tunable wetting defects characterized by a simple capillary force sensor*, Langmuir 29 (2013), 9944–9949.

[39] T. Franke, A.R. Abate, D.A. Weitz and A. Wixforth, *Surface acoustic wave (SAW) directed droplet flow in microfluidics for PDMS devices*, Lab Chip 9 (2009), 2625-2627.

[40] D.C. Duffy, J.C. Mcdonald, O.J.A. Schueller and G.M. Whitesides, *Rapid prototyping of microfluidic systems in poly(dimethylsiloxane)*, Anal. Chem. 70 (1998), 4974-4984.

[41] H.S. Hele-Shaw, *On the motion of a viscous fluid between two parallel plates*, Trans. R. Inst. Nav. Archit. 40 (1898).

[42] T.B. Jones, K.L. Wang and D.J. Yao, *Frequency-dependent electromechanics of aqueous liquids: Electrowetting and dielectrophoresis*, Langmuir 20 (2004), 2813-2818.

[43] A. Staicu and F. Mugele, *Electrowetting-induced oil film entrapment and instability*, Phys. Rev. Lett. 97 (2006), 167801.

[44] J.S. Lee and Y.C. Fung, *Stokes flow around a circular cylindrical post confined between 2 parallel plates*, J. Fluid Mech. 37 (1969), 657-670.

[45] S.A. Vanapalli, A.G. Banpurkar, D. Van Den Ende, M.H.G. Duits and F. Mugele, *Hydrodynamic resistance of single confined moving drops in rectangular microchannels*, Lab Chip 9 (2009), 982-990.

[46] E.W.M. Kemna, L.I. Segerink, F. Wolbers, I. Vermes and A. Van Den Berg, *Label-free, high-throughput, electrical detection of cells in droplets*, Analyst 138 (2013), 4585-92.

[47] T.B. Jones, J.D. Fowler, Y.S. Chang and C.J. Kim, *Frequency-based relationship of electrowetting and dielectrophoretic liquid microactuation*, Langmuir 19 (2003), 7646-7651.

[48] R. Pethig, *Review article - Dielectrophoresis: Status of the theory, technology, and applications*, Biomicrofluidics 4 (2010), 022811.

Appendix 7A The flow resistance of a circular drop sandwiched between two plates

7A.1 Analytical expression

In the Hele-Shaw approximation, the drag force on a circular drop with radius R sandwiched between two parallel plates with gap h ($h/R \ll 1$) can be calculated analytically. We have to solve the set of equations

$$\nabla p = \mu\left(\nabla^2 \underline{u} - \frac{12}{h^2}\underline{u}\right)$$

$$\nabla \cdot \underline{u} = 0$$

These can be rewritten in terms of the stream function Ψ and the vorticity function Ω as

$$\nabla^2 \Psi = \Omega$$

$$\nabla^2 \Omega = \kappa^2 \Omega$$

where Ψ is defined by $\underline{u} = \nabla \times \left(\Psi \underline{e_z}\right)$ and $\kappa^2 = 12/h^2$.

The problem is analyzed in cylindrical coordinates with the drop positioned at the origin. At the drop boundary $r = R$ we assume a no-slip boundary condition, and away from the drop the velocity field u_∞ is homogeneous. The complete solution of the flow field around the drop is then given by

$$\Psi(r,\phi) = u_\infty R \sin(\varphi)\left\{\frac{r}{R} - \frac{R}{r} + \frac{2K_1(q)}{qK_0(q)}\left(\frac{K_1(qr/R)}{K_1(q)} - \frac{R}{r}\right)\right\}$$

where K_0 and K_1 are modified Bessel functions of the second kind and $q = 2\sqrt{3}R/h$. From this equation the pressure field can be determined to be

$$p(r,\phi) = p_0 - \mu\kappa^2 u_\infty R\cos(\phi)\left\{\frac{r}{R} + \frac{R}{r} + \frac{2K_1(q)}{qK_0(q)}\frac{R}{r}\right\}$$

The net force in the direction of the flow on a fluid disc with radius r can subsequently be calculated from

$$F_x = rH\int_0^{2\pi} \underline{e_r} \cdot \left(-p\underline{\underline{1}} + 2\mu\underline{\underline{D}}\right) \cdot \underline{e_x} d\varphi$$

which for $r = R$ reduces to

$$F_x = \frac{24\pi\mu u_\infty R^2}{h}\left(1 + \frac{2K_1(q)}{qK_0(q)}\right)$$

The results we obtained with this 2D calculation agree well with the two-term approximation as derived by Lee and Fung, which can be used for ($h/R \leq 2.5$) [44].

7A.2 Numerical calculations taking into account the microchannel walls

When the drop size becomes of the order of the finite channel width, the drop blocks a significant fraction of the channel width for flow of the continuous phase. In addition, the no-slip boundary condition at the confining side walls has to be taken into account. Thus, the width of the microchannel becomes the third length scale in the problem, in addition to the drop radius and the channel height. We numerically calculated the flow and pressure fields with an extension of the Hele-Shaw approximation to include the no-slip boundary conditions on the side walls. The problem is reduced to a 2D calculation by averaging the velocity field over the height of the channel. The dimensionless Stokes equations can then be written as

$$\partial_\xi \pi = \left\{e^2\left(\partial_\xi{}^2 + \partial_\eta{}^2\right) - 12\right\}\partial_\eta \psi$$

$$-\partial_\eta \pi = \left\{e^2\left(\partial_\xi{}^2 + \partial_\eta{}^2\right) - 12\right\}\partial_\xi \psi$$

$$\partial_\zeta \pi = 0$$

where π is the dimensionless pressure, ψ the dimensionless stream function, $e = 2h/W$ the aspect ratio of the microchannel, and ξ, η, and ζ the three dimensionless coordinates. Details of the calculation were previously described in Vanapalli *et al*. [45]. Due to the symmetry of the configuration the calculations are restricted to a single quadrant with $0 < x < W$ and $0 < y < W/2$. After determination of the stream function (Figure A1A) and the pressure in the channel, the drag force on the drop is calculated by

$$F_{drag} = F_p - F_s - F_b$$

with

$$F_p = -2hW\int_0^W \partial_x p(x, W)\mathrm{d}x$$

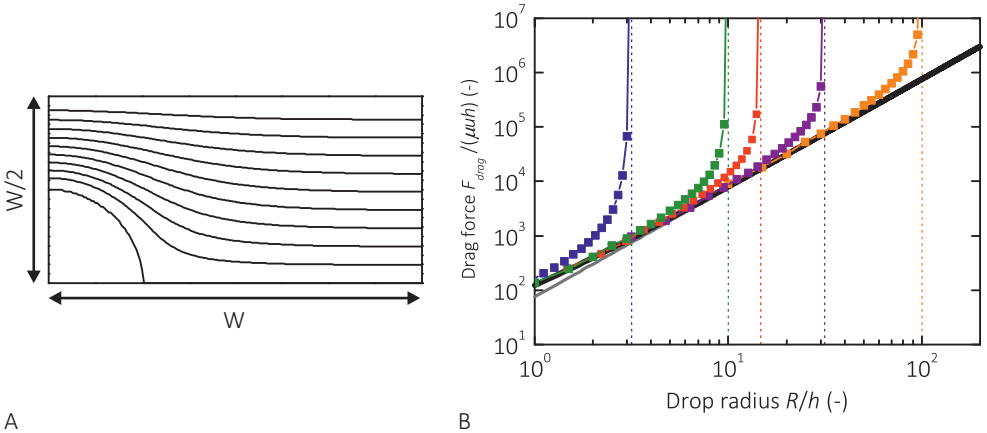

A B

Figure A1 The drag force on a circular drop. (A) Example of a flow line pattern for a drop with $2R/W = 1/2$. (B) Drag force versus drop radius, as calculated analytically for an infinitely wide channel, *i.e.*, the aspect ratio $e = 2h/W \to 0$ (thick black line), with scaling arguments for large drops $R \gg h$ (thin gray line), and numerically in a channel with $e = 0.316$ (blue), $e = 0.100$ (green), $e = 0.068$ (red), $e = 0.032$ (purple), and $e = 0.010$ (orange) with a no-slip boundary condition on the drop surface.

$$F_s = -4\mu H \int_0^W \partial_y{}^2 \Psi(x, W)\mathrm{d}x$$

$$F_b = 48(\mu W/h)\Psi_W$$

the driving force due to the pressure gradient, and the opposing shear force along the sidewalls and the top and bottom walls, respectively.

The results for channels with various aspect ratios are compared to the expression for an infinitely wide channel (Figure A1B). Here, we model the drop as a solid disk with a no-slip boundary condition at the drop surface. For small drops, the numerical results nicely coincide with the analytical expression. When the drop size approaches the channel width (as indicated by the vertical lines), the hydrodynamic drag force on the drop diverges due to the pressure build-up.

Figure A2A shows an experimental trapping diagram for a channel with $W = 500$ µm and drop radii R up to 200 µm. Thus, in these experiments the drop sizes are of the order of the channel width. Using the analytical expression for F_{drag} and plotting it against $F_{el,max}$

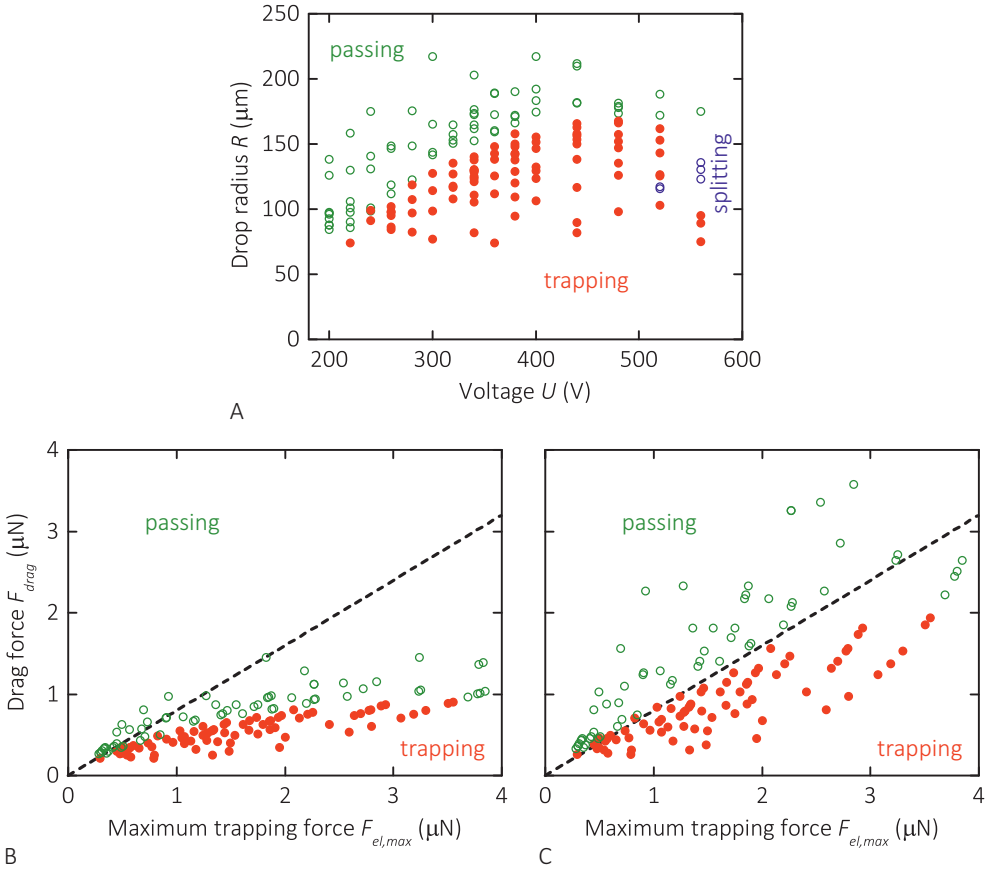

Figure A2 Experimental results for more narrow channels ($W = 500$ μm). (A) Experimental trapping diagram; depending on applied voltage and drop radius, drops are either being trapped by (red closed symbols), passing (green open symbols), or split by (blue open symbols) the electrodes. (B-C) Drag force versus maximum trapping force for the experimental results in (A). In (B) the drag force is calculated analytically, assuming $2R/W \ll 1$, while in (C) the drag force is calculated numerically, taking into account the finite channel width. The black dotted line is a linear fit to the data in (C) at small trapping force.

in Figure A2B indicates that the drag force is underpredicted, especially for the larger drops. Using the numerical results for the drag force in Figure A2C, we now find a much better linear relationship between F_{drag} and $F_{el,max}$. The lack of quantitative correspondence is most probably due to uncertainty in the flow rate (a pressure difference was applied). In addition, for larger trapping forces ($F_{el,max} > 3$ μN) drop deformations start to influence the results significantly.

Chapter 8

Concluding remarks

Oil drops in the pore space of a reservoir rock can interact with a wide range of structured surfaces, due to the complex and variable shapes of rock grains and the chemical variety in adsorbed clays. Drops can attain various morphologies depending on their volume and the surface wettability. As a result, modification of these properties (*e.g.*, through coalescence, or ad- or desorption) generally leads to changes in drop shape and position. We investigated the removal of these drops in some generic geometries, *i.e.*, drops between a sphere and a plane, drops on fibers, and drops in microfluidic channels with a 'wetting defect'. The formation of visco-elastic layers at the oil-water interface contributes to the complexity of the problem.

8.1 Morphological transitions

We first consider drops interacting with ideal, *i.e.*, microscopically smooth and chemically homogeneous, surfaces that are structured on the scale of the drop size. Drops in a sphere/ plane geometry can either attain an axisymmetric non-spherical shape or a non-axisymmetric spherical shape (Chapter 5). Every contact angle yields a single energy minimum, resulting in a continuous and fully reversible transition. Non-axisymmetric shapes should move gradually radially outward upon increasing the contact angle above its critical value. The morphological transitions of drops on fibers between multiply connected barrel shapes and simply connected clamshell shapes (Chapter 6) are however discontinuous. Energy barriers that are large compared to thermal energies, separate the local minima and render the two morphologies mechanically stable for a broad range of intermediate $\left(\theta, \tilde{V}\right)$ values, thereby introducing a history dependence in the drop morphology [1].

8.1.1 Force required for drop removal

The external forces that might facilitate drop release and subsequent removal are generally buoyancy forces or pressure or viscous drag. We initially studied the effect of buoyancy on the morphology of drops on fibers (Chapter 6). The capillary length now appears as a third parameter controlling the drop morphology next to contact angle and drop size. The introduction of buoyancy breaks the cylindrical symmetry of the barrel and shifts the stability limits, shrinking the bistable and barrel regimes in favor of the clamshell regime. More importantly, we found a new stability limit for the clamshell morphology related to partial detachment from the fiber. The typical length for detachment scales with the capillary length (with a power 2/3 – 1). Drop removal can thus be achieved for large drops, large density differences, or low interfacial tensions, although part of the liquid will remain attached to the fiber.

In the rock pore space, the capillary length is typically a few millimeters due to the small density differences ($<$ 0.2 g/mL) and oil-water interfacial tensions of 10-30 mN/m. The buoyancy forces on individual micron scale drops are thus negligible, requiring an other driving force. Analyzing the energy diagram for a given contact angle for the maximum slope, yields the external force that is required to (partially) remove the drop from the contacting solid(s). Figure 1 shows typical results for both drops in a sphere/ plane geometry (Figure 1A) and drops on a fiber (Figure 1B). The force decreases with increasing contact angle and obviously vanishes for $\theta \rightarrow 180°$. However, in both cases we do not

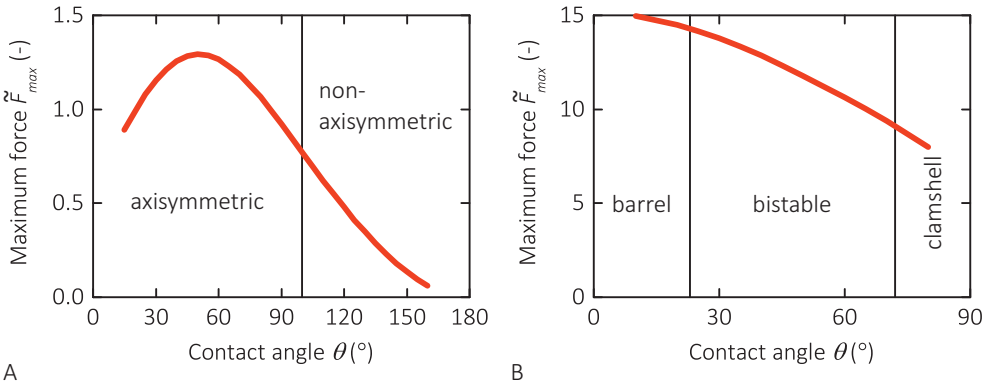

Figure 1 Force required for drop removal versus contact angle for (A) drops in a sphere/ plane geometry ($\tilde{V} = 1$ and $\tilde{s} = 0.5$) and (B) drops on a fiber ($\tilde{V} = 1100$). The typical length scale for non-dimensionalisation is either the radius of the sphere or the radius of the fiber.

observe a bifurcation of the force upon reaching the transition points. In the bistable regime for drops on fibers, the required force is equal for barrels and clamshells. We find no influence of the attained morphology, as barrels can only detach *via* the clamshell shape, and the maximum slope is always found for the latter (see Figure 4A in Chapter 6). Similarly, axisymmetric liquid bridges in a sphere/ plane geometry can only detach *via* a non-axisymmetric shape. A drastic decrease in required external force is thus only obtained for a large wettability alteration.

8.1.2 The effect of surface heterogeneity on morphological transitions

For drops on fibers, the transitions are relatively insensitive to small differences between the advancing and receding contact angles due to large slopes in the energy diagram and the dominating effect of small mismatches in the mass densities. However, for drops in a sphere/ plane geometry we find significant discrepancies between the experiments and the predictions. Experimentally, substantial history dependence in the global drop morphology is observed. Drops are frequently trapped in the confined space between the sphere and the plane, and their outward movement is significantly delayed compared to the expectations. We have shown that minor contact angle hysteresis (below 1 degree) due to microscopic heterogeneity can be the cause of the deviations from the 'ideal' behavior, as the driving forces are very small. As a result, the drop never reaches the symmetry axis. When the contact angle is increased starting from a low value (*i.e.*, good wettability), the outward movement shows a discontinuity.

These observations have important implications for natural systems, such as the rock pore space, where contact angle hysteresis can be up to several tens of degrees. Removal of drops from a confined geometry is thus seriously hampered by the presence of this contact angle hysteresis. If the magnitude of the wettability alteration is large, drops may show a discontinuous behavior in their morphology and position. However, we can conclude that in most cases the removal of single drops relies on large external forces facilitating the release.

8.2 Micropatterned surfaces

In the previous paragraph we summarized our findings for drops interacting with a surface structured on the scale of the drop size. Drops that interact with microscopically heterogeneous surfaces can be conveniently studied in microfluidic channels with confining walls. We used electrowetting to create a 'wetting defect' and determined the drag forces required for detaching a drop from it (Chapter 7). We found that the trapping and removal can be predicted with a fairly simple force balance. To approach the situation in EOR more closely, these experiments could be extended to measurements of pinning forces on drops interacting with topographically and chemically heterogeneous (rock) surfaces. Channels could then be flushed with high and low salinity brine to influence the stability of previously deposited monolayers of polar oil compounds [2]. The opposing force for drop removal could be provided by the flowing ambient phase, or by electrodes in the second microchannel wall, pulling the drop from the defect.

For weakly confined oil drops, *i.e.*, drops that do not block a significant fraction of the pore space, both the viscous drag and the pressure drag are generally small due to the low viscosity and flow velocity (of the order of μm/s) of the continuous phase. The magnitude of these forces is not sufficient to overcome the pinning forces. However, as noted before, when the drop size becomes of the order of the pore size, the flow velocity and thus the drag forces increase significantly (Chapter 7). In general, oil can only be effectively removed when it is present as a large connected volume that can not be bypassed by the water phase *via* different pathways.

8.3 Role of the oil-water interface

Adsorption of amphiphilic species onto the oil-water interface will also affect the possibilities for removing drops from (rock) surfaces. As long as the oil-water interface

remains fluid-like, its role can be captured *via* the interfacial tension. The Young angle (dictating the drop morphology) and the Laplace pressure for a given drop curvature (or vice versa the curvature for a given pressure) will change. More than one interface may be involved at the same time: the amphiphilic species adsorbing onto the oil-water interface may also adsorb onto, or have desorbed, from a rock or clay surface. Studying these processes requires an 'integrated approach', in which the different interfaces are addressed simultaneously. In this thesis, a method was developed for studying two interfacial tension changes simultaneously (Chapter 4). While this can offer a useful diagnostic tool, it does not reveal mechanistic information. For the latter, additional microscopic techniques aimed at chemical structure and the presence of wetting films are needed.

We also found in this thesis that under certain chemical conditions, more complex interfacial layers can be formed (Chapter 3). Solid-like layers were in our case found for a model system of calcium-stearate, but would also be conceivable in EOR applications where (metal complexes of) naphthenates and asphaltenes can be involved in adsorption. Such solid-like layers increase the complexity of the system both in the physical and the chemical sense. Further study of these systems might be justified by more concrete evidence that these layers play an important role under reservoir conditions (elevated temperatures and multiple chemical species).

References

[1] H.B. Eral, J. De Ruiter, R. De Ruiter, J.M. Oh, C. Semprebon, M. Brinkmann and F. Mugele, *Drops on functional fibers: from barrels to clamshells and back*, Soft Matter 7 (2011), 5138-5143.

[2] N. Kumar, L. Wang, I. Siretanu, M. Duits and F. Mugele, *Salt dependent stability of stearic acid Langmuir-Blodgett films exposed to aqueous electrolytes*, Langmuir 29 (2013), 5150-5159.

Acknowledgements

First of all I would like to thank my promotor Frieder Mugele and my daily supervisor Michèl Duits. Frieder, thank you for accepting me as PhD student in the Physics of Complex Fluids group, and the support and inspiration throughout these years. Michèl, thank you for your valuable input in my papers. Your suggestions and corrections were always highly appreciated.

My work has been part of the Enhanced Oil Recovery Exploratory Research Program, which is funded by BP. Within this project we have been collaborating with BP's Pushing Reservoir Limits Team, the Dynamics of Complex Fluids group of prof. Stephan Herminghaus at the Max Planck Institute for Dynamics and Self-Organization in Göttingen, and the NanoGeoScience group of prof. Susan Stipp and the University of Copenhagen. I would like to thank all people involved for the stimulating discussions during the numerous ExploRe meetings. Special thanks go to BP's Ian Collins, Isabella Stocker, and Pete Salino, for their contributions and interesting insights in the world of oil recovery.

I really enjoyed the collaboration with Ciro Semprebon and Martin Brinkmann (Göttingen) on the morphological transitions of drops on fibers and drops in a sphere/ plane geometry. Ciro and Martin, your Surface Evolver calculations always inspired us to perform more experiments, and our discussions always gave me new insights in the topic of morphological transitions.

I would like to thank all members of my thesis committee for taking the effort to critically read my thesis. Also, I highly appreciate your contributions to the mini-symposium organized the day after.

I would like to thank all my (former) colleagues for their contributions, both scientifically and socially, to the nice atmosphere in the Physics of Complex Fluids group. I really enjoyed the many group outings, sports days, thesis defenses, Frisbee breaks, shared dinners, game nights, and other fun activities. The administrative support by Annelies, Lisette, and Edith, and the technical support by Mariska, Daniel W., Daniel E., and Klaas is greatly appreciated. I was happy to supervise Peter, Pim, Astrid, Boris, Vitor and Mathijs during their thesis projects and internships. Thank you all for your valuable contributions.

Special thanks go to all colleagues with whom I collaborated on a publication: Willem on the analysis of metal-stearate layers, Arun on the measurement of interfacial tension with

electrowetting, and Arjen and Dirk on the electrostatic potential wells in microfluidics. Burak, Jolet, and Jung, it was a great pleasure to work with you on the drop-on-a-fiber team!

Some distraction of PhD stress was luckily offered by Lindy Hop. I would like to thank all members of Swing Out Loud for the enjoyable lessons, workshops, performances, tea dances, and parties. The weekly survivalrun practices with Tartaros were the perfect opportunity to let off some steam! I really enjoyed all practices and the runs we joined together.

I am very happy that Dieter and Bijoy accepted to be my paranymphs. Thank you for all the nice times we shared together, both during and outside working hours. Dieter, I enjoyed the Lindy Hop events, gaming nights, conferences, and all other activities. Bijoy, joining the summer school in Les Houches together was a great experience. I am glad that Huub and Erik L. are completing our paranymph team. Huub, thank you for all shared moments, relaxing holidays, and for listening to all our concerns and complaints. Erik L., I enjoyed our Lindy Hop activities very much.

Jolet and I started our PhD projects simultaneously and are also lucky to be able to defend at the very same day. Jolet, thank you for sharing this from beginning to end, with all ups and downs. You have been a great support and contributed to my own work, and I like to believe you also taught me something about air film lubrication in drop impact.

Ten slotte wil ik graag onze ouders bedanken voor hun ondersteuning en de nodige afleiding tijdens de gezamenlijke weekenden. Papa en mama, bedankt voor jullie continue aanmoediging, interesse en vertrouwen in een succesvolle afronding!

Riëlle de Ruiter
Enschede, March 2014

List of publications

Publications from this thesis research: (* equal contributions)

R. de Ruiter, A.M. Pit, V. Martins de Oliveira, M.H.G. Duits, H.T.M van den Ende and F. Mugele. Electrostatic potential wells for on-demand drop manipulation in microchannels. *Lab on a Chip* **14** (2014), 883-891.

R. de Ruiter*, J. de Ruiter*, H.B. Eral, C. Semprebon, M. Brinkmann and F. Mugele. Buoyant droplets on functional fibers. *Langmuir* **28** (2012), 13300-13306.

R. de Ruiter, P.A. Wennink, A.G. Banpurkar, M.H.G. Duits and F. Mugele. Use of electrowetting to measure dynamic interfacial tensions of a microdrop. *Lab on a Chip* **12** (2012), 2832-2836.

R. de Ruiter, R.W. Tjerkstra, M.H.G. Duits and F. Mugele. Influence of cationic composition and pH on the formation of metal stearates at oil-water interfaces. *Langmuir* **27** (2011), 8738-8747.

In preparation:

R. de Ruiter, M. van Gorcum, C. Semprebon, M.H.G. Duits, M. Brinkmann and F. Mugele, Influence of contact angle hysteresis on the morphology and position of drops confined between a sphere and a plane.

Other publications:

H.B. Eral*, J. de Ruiter*, R. de Ruiter*, J.M. Oh, C. Semprebon, M. Brinkmann and F. Mugele. Drops on functional fibers: from barrels to clamshells and back. *Soft Matter* **7** (2011), 5138-5143.

K. van Dijke, R. de Ruiter, K. Schroën and R. Boom. The mechanism of droplet formation in microfluidic EDGE systems. *Soft Matter* **6** (2010), 321-330.

J.C. Bird, R. de Ruiter, L. Courbin and H.A. Stone. Daughter bubble cascades produced by folding of ruptured thin fims. *Nature* **465** (2010), 759-762.

L.M.C. Sagis, R. de Ruiter, F.J. Rossier Miranda, J. de Ruiter, K. Schroën, A.C. van Aelst, R. Boom and E. van der Linden. Polymer microcapsules with a fiber-reinforced nanocomposite shell. *Langmuir* **24** (2008), 1608-1612.

Conference presentations:

Physics@FOM, Veldhoven (21-22 January 2014). Electrostatic potential wells for drop manipulations in microchannels. Co-authors: A.M. Pit, V. Martins de Oliveira, M.H.G. Duits, H.T.M van den Ende and F. Mugele. Oral presentation.

MicroTAS, Freiburg (27-31 October 2013). Electrostatic potential wells for manipulations of drops in microchannels. Co-authors: A.M. Pit, V. Martins de Oliveira, D. Wijnperlé, M.H.G. Duits, H.T.M van den Ende and F. Mugele. Poster presentation and conference proceedings.

MESA+ Meeting, Enschede (16 September 2013). Drop manipulation in microchannels using electrodes. Co-authors: A.M. Pit, V. Martins de Oliveira, M.H.G. Duits, H.T.M van den Ende and F. Mugele. Poster presentation.

Advances in Microfluidics & Nanofluidics, South Bend (24-26 May 2013). Electro-wetting controlled drop manipulation in microchannels. Co-authors: A.M. Pit, M.H.G. Duits, H.T.M van den Ende and F. Mugele. Oral presentation.

Physics@FOM, Veldhoven (22-23 January 2013). Electrowetting driven morphology transitions. Co-authors: J. de Ruiter, H.B. Eral, J.M. Oh, M. van Gorcum, M.H.G. Duits, C. Semprebon, M. Brinkmann and F. Mugele. Poster presentation.

Burgersdag, Enschede (10 January 2013). Electro-wetting controlled drop manipulation in microchannels. Co-authors: M.H.G. Duits, H.T.M. van den Ende and F. Mugele. Oral presentation.

APS Division of Fluid Dynamics Meeting, San Diego (18-20 November 2012). Electro-wetting controlled drop manipulation in microchannels. Co-authors: M.H.G. Duits, H.T.M. van den Ende and F. Mugele. Oral presentation.

Liquid Matter Conference, Vienna (6-10 September 2011). Formation of solid metal stearate layers at the decane/water interface. Co-authors: R.W. Tjerkstra, M.H.G. Duits and F. Mugele. Poster presentation.

NWO Scientific Meeting on Chemistry, Veldhoven (14-15 March 2011). Formation of solid metal stearate layers at the decane/water interface. Co-authors: R.W. Tjerkstra, M.H.G. Duits and F. Mugele. Poster presentation.

Physics@FOM, Veldhoven (18-19 January 2011). Drops on functional fibers: from barrels to clamshells and back. Co-authors: J. de Ruiter, H.B. Eral, J.M. Oh, C. Semprebon, M. Brinkmann and F. Mugele. Poster presentation.

FERMAT-IMPACT-GIMFus Meeting, Sevilla (20-22 October 2010). Solidified surfactant layers at oil-water interfaces. Co-authors: R.W. Tjerkstra, M.H.G. Duits and F. Mugele. Oral presentation.

International Meeting on Electrowetting, Pohang (24-26 June 2010). Electrowetting-induced morphological transitions of droplets on a fiber. Co-authors: J. de Ruiter, H.B. Eral, J.M. Oh, C. Semprebon, M. Brinkmann and F. Mugele. Poster presentation and oral presentation.

International Meeting on Electrowetting, Pohang (24-26 June 2010). Determination of dynamic interfacial tension by electrowetting. Co-authors: P.A. Wennink, A.G. Banpurkar, M.H.G. Duits and F. Mugele. Poster presentation.

Inside front covers:

Eral *et al*. (2011)

de Ruiter *et al*. (2014)

About the author

Riëlle de Ruiter was born on the 5th of April 1985 in Tiel (The Netherlands), and grew up in Geldermalsen. After completing secondary education at the RSG Lingecollege in Tiel in 2003, she obtained her propaedeutic diplomas in Applied Physics and Applied Mathematics at the Eindhoven University for Technology. In 2007 she obtained her Bachelor's degree (*cum laude*) in Food Technology from Wageningen University, with a thesis on the production of polymer microcapsules by electrostatic layer-by-layer deposition of pectin and whey protein isolate fibrils. In 2009 she obtained her Master's degree (*cum laude*) in Food Technology with a specialization in Process and Product Design. As part of the study program she spend five months in the Complex Fluids group of Howard Stone at Harvard University in Cambridge (USA), working on a project about the formation of daughter bubbles during soap bubble rupture. Her thesis about spontaneous droplet generation in edge-based droplet generation devices was performed under supervision of dr. Karin Schroën in the Food Process Engineering group of prof. Remko Boom.

In 2009, she started her PhD research in the Physics of Complex Fluids group within the MESA+ Institute for Nanotechnology and the Department of Science and Technology of the University of Twente, under supervision of prof. Frieder Mugele and dr. Michel Duits. The results of this research are presented in this thesis.

International Meeting on Electrowetting, Pohang (South-Korea, 2010)

ISBN: 978-90-365-3638-4